

**APPLICATION OF PHOTO-ENHANCED BATTERY AS
AUXILIARY ELECTRODES IN ELECTROCHEMICAL
WATER SPLITTING**



**A Thesis Submitted in Partial Fulfillment of the Requirements for the
Degree of Doctor of Philosophy in Physics
Suranaree University of Technology
Academic Year 2020**

การประยุกต์ใช้ข้าวเบตเตอร์ที่เพิ่มประสิทธิภาพด้วยแสงเป็นข้าวเสริมในการแยก
น้ำด้วยไฟฟ้าเคมี



นางสาวสุพรรณษา มุสิกะเจริญ

วิทยานิพนธ์นี้เป็นส่วนหนึ่งของการศึกษาตามหลักสูตรปริญญาวิทยาศาสตรดุษฎีบัณฑิต

สาขาวิชาฟิสิกส์

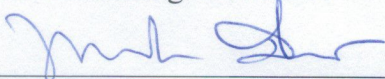
มหาวิทยาลัยเทคโนโลยีสุรนารี

ปีการศึกษา 2563

**APPLICATION OF PHOTO-ENHANCED BATTERY AS
AUXILIARY ELECTRODES IN ELECTROCHEMICAL WATER
SPLITTING**

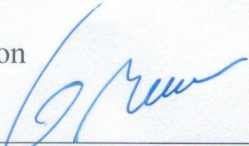
Suranaree University of Technology has approved this thesis submitted in partial fulfillment of the requirements for the Degree of Doctor of Philosophy.

Thesis Examining Committee



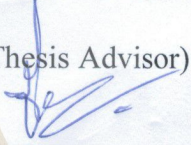
(Assoc. Prof. Dr. Panomsak Meemon)

Chairperson



(Assoc. Prof. Dr. Worawat Meevasana)

Member (Thesis Advisor)



(Dr. Teera Butburee)

Member



(Assoc. Prof. Dr. Prayoon Songsiriritthigul)

Member



(Assoc. Prof. Dr. Rapee Utke)

Member



(Assoc. Prof. Dr. Chatchai Jothityangkoon)

Vice Rector for Academic Affairs
and Quality Assurance



(Prof. Dr. Santi Maensiri)

Dean of Institute of Science

สุพรรณษา มุสิกะเจริญ : การประยุกต์ใช้ขั้วแบตเตอรี่ที่เพิ่มประสิทธิภาพด้วยแสงเป็นขั้วเสริมในการแยกน้ำด้วยไฟฟ้าเคมี (APPLICATION OF PHOTO-ENHANCED BATTERY AS AUXILIARY ELECTRODES IN ELECTROCHEMICAL WATER SPLITTING) อาจารย์ที่ปรึกษา : รองศาสตราจารย์ ดร.วรวัดน์ มีวาสนา, 131 หน้า.

CuO-Cu(OH)₂/Cu₂O/ ขั้วตัวกลางรีดอกซ์/ ตัวเก็บประจุยิ่งยวดที่ตอบสนองต่อแสง/ ระบบแยกน้ำด้วยวิธีทางไฟฟ้า/ ไฮโดรเจน/ ช่องว่างออกซิเจน

การแยกน้ำด้วยวิธีทางไฟฟ้าซึ่งเป็นวิธีการผลิตไฮโดรเจนแบบยั่งยืนที่ได้รับความสนใจอย่างมากในช่วงไม่กี่ปีที่ผ่านมา อย่างไรก็ตามการผลิตไฮโดรเจนที่มีความบริสุทธิ์สูงและราคาต้นทุนต่ำยังเป็นความท้าทายสำหรับการผลิตไฮโดรเจนขนาดใหญ่ ดังนั้นการศึกษานี้จึงได้เสนอกลยุทธ์ในการรวมระบบการแยกน้ำแบบสองเซลล์เข้ากับการกักเก็บพลังงานแสงอาทิตย์ โดยระบบแยกน้ำนี้ใช้ CuO-Cu(OH)₂/Cu₂O เป็นขั้วตัวกลางรีดอกซ์ระหว่างเซลล์ไฮโดรเจนและออกซิเจน ระบบแยกน้ำแบบสองเซลล์นี้ไม่เพียงแต่ป้องกันการรวมกันของแก๊สแต่ยังสามารถเพิ่มอัตราการเกิดแก๊สได้อีกด้วยซึ่งปฏิกิริยารีดอกซ์ (การชาร์จ/การดิสชาร์จ) ของ CuO-Cu(OH)₂/Cu₂O โดยอาศัยแสงทำให้อัตราการผลิตแก๊สไฮโดรเจนเพิ่มขึ้นอย่างมีนัยสำคัญ (52%) จาก 111.7 $\mu\text{mol h}^{-1}\text{cm}^{-2}$ ในเงื่อนไขไม่ฉายแสงเป็น 168.9 $\mu\text{mol h}^{-1}\text{cm}^{-2}$ ภายใต้แสงอาทิตย์ เพื่อศึกษากลไกของแสงต่อปฏิกิริยารีดอกซ์ของขั้ว CuO-Cu(OH)₂/Cu₂O สามารถศึกษาได้จากสมบัติทางไฟฟ้าเคมี ซึ่งจากกราฟโวลแทมเมตรี (CV) และการประจุที่กระแสคงที่ (GCD) พบว่าภายใต้การฉายแสงอาทิตย์ทำให้ความจุของขั้ว CuO-Cu(OH)₂/Cu₂O เพิ่มขึ้น 36% และผลของแสงต่อขั้วไฟฟ้าตัวกลางในระหว่างการแยกน้ำนั้นตรวจสอบจาก *in-situ* X-ray absorption และ photoemission spectroscopy (XAS และ PES) พบว่าขณะฉายแสงอาทิตย์เกิดช่องว่างของออกซิเจนบริเวณผิวของขั้วตัวกลางซึ่งเป็นบทบาทสำคัญในการเพิ่มปฏิกิริยารีดอกซ์และความจุของขั้วตัวกลางและการเพิ่มขึ้นของอัตราการเกิดแก๊ส การค้นพบนี้ถือเป็นทางเลือกใหม่ในการกักเก็บพลังงานแสงอาทิตย์ได้โดยตรงและเป็นการผลิตไฮโดรเจนแบบยั่งยืนที่มีราคาต้นทุนต่ำ

สาขาวิชาฟิสิกส์

ปีการศึกษา 2563

ลายมือชื่อนักศึกษา

ลายมือชื่ออาจารย์ที่ปรึกษา

สุพรรณษา มุสิกะเจริญ
[ลายมือ]

SUPANSA MUSIKAJAROEN : APPLICATION OF BATTERY
ELECTRODES IN PHOTO- ENHANCED WATER SPLITTING. THESIS
ADVISOR : ASSOC. PROF. WORAWAT MEEVASANA, PH.D. 131 PP.

CuO-Cu(OH)₂/ Cu₂O/ REDOX MEDIATOR ELECTRODE/ ELECTROLYSIS/
PHOTO-SUPERCAPACITOR/ HYDROGEN/ OXYGEN VACANCY

Water electrolysis has received much attention in recent years as a means of sustainable H₂ production. However, many challenges remain in obtaining high-purity H₂ and making large-scale production cost-effective. This study provides a strategy for integrating a two-cell water electrolysis system with solar energy storage. In our proposed system, CuO-Cu(OH)₂/Cu₂O was used as a redox mediator between oxygen and hydrogen evolution components. The system not only overcame the gas-mixing issue, but also showed high gas generation performance. The redox reaction (charge/discharge) of CuO-Cu(OH)₂/Cu₂O led to a significant increase (51%) in the rate of H₂ production from 111.7 μmol h⁻¹cm⁻² in the dark to 168.9 μmol h⁻¹cm⁻² under solar irradiation. In order to explain the effect of solar irradiation of three-electrode system, the electrochemical properties of the CuO-Cu(OH)₂/Cu₂O were investigated. The cyclic voltammetry (CV) and galvanostatic charge-discharge (GCD) curves under light irradiation show enhancement of capacitance by 36% compared dark condition. The effects of light on the redox reaction of CuO-Cu(OH)₂/Cu₂O during water electrolysis were investigated by *in-situ* X-ray absorption and photoemission spectroscopy. These results suggest that surface oxygen vacancies are created under irradiation and play an important role in increased capacitance and gas generation.

These findings provide a new path to direct storage of abundant solar energy and low-cost sustainable hydrogen production.

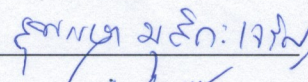
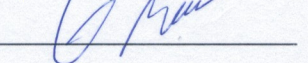


School of Physics

Academic Year 2020

Student's Signature

Advisor's Signature

สุรนารี ๒๕๖๓: ๑๖/๗



ACKNOWLEDGEMENTS

My research and thesis could not be done without the help and support of several people. First and foremost, I would like to sincerely thank my thesis advisor, Assoc. Prof. Dr. Worawat Meewasana, for the continuous support of my Ph.D. study during 5 years. I received many scientific ideas, excellent knowledge, patience, motivation, enthusiasm, and an opportunity to learn about data analysis and many types of equipment in France and China. These are provided me a research experience. Furthermore, he gave me a good direction, and his advice helped me throughout my research and writing of this thesis. I could not have imagined having a better advisor and mentor for my Ph.D. study.

Besides my advisor, I would like to thank the rest of my thesis committee: Assoc. Prof. Dr. Panomsak Meemon, Dr. Teera Butburee, Assoc. Prof. Dr. Prayoon Songsiriritthikul, and Assoc. Prof. Dr. Rapee Utke, for their encouragement, insightful comments, and hard questions.

I would like to thank Mr. Siwat Polin, Dr. Suchinda Sattayaporn, Dr. Pinit Kidkhunthod, Dr. Hideki Nakajima, Narong Chanlek, Dr. Rutchadaporn Supruangnet, Mr. Surachet Rattanasuporn, Mr. Watcharapon Jenpiyapong and Miss Arunothai Rattanachata for help in UPS/XPS, and XAS measurement, Dr. Teera Butburee, Asst. Prof. Dr. Wittawat Seanrang, Mr. Warakorn Jindata, Mr. Chutchawan Jaisuk, Dr. Tanachat Eknapakul, Miss Areeya Mooltang, Mr. Worasarit Saengsui and Meevana group for helpful discussion.

I am deeply grateful to financial support by Center of Excellence in Advanced Functional Materials (CoE-AFM), External Grants and Scholarships for Graduate Students (OROG) Suranaree University of Technology, the Research Network NANOTEC (RNN) program of the National Nanotechnology Center (NANOTEC), NSTDA, and the Office of Naval Research Global under Grant No. N62909-18-1-2018.

I would like to thank all of staff at the School of Physics, Institute of Science, Suranaree University of Technology for giving me knowledge and inspiring me to do the research. Special thank go to Mrs. Phenkhae Petchmai who helps me doing the documents and always correct some mistakes that I had made.

It is impossible to list all of my fellow graduate students, who were a great support during my Ph.D. study, for all the great times we had together.

Finally, I would like to give my gratitude my family to support and understanding who gave me inspiration to encouraged me to pursue this degree. They are always there for me and giving me faith and care to achieve the best I can do.

Supansa Musikajaroen

มหาวิทยาลัยเทคโนโลยีสุรนารี

CONTENTS

	Page
ABSTRACT IN THAI	I
ABSTRACT IN ENGLISH	II
ACKNOWLEDGMENTS	IV
CONTENTS	VI
LIST OF TABLES	X
LIST OF FIGURES	XI
LIST OF ABBREVIATIONS	XXIII
CHAPTER	
I INTRODUCTION	1
1.1 Background and Motivation	1
1.2 Research objective/ Purposes of the study	7
1.3 Scope and limitations	7
1.4 Anticipated outcomes	8
1.5 Outline of thesis	8
II LITERATURE REVIEWS	9
2.1 Brief overview of electrochemical energy storage	10
2.1.1 Rechargeable batteries (Li-ion battery)	11
2.1.2 Supercapacitors	13
2.2 Photo-assist charging energy storage devices	17
2.3 Decoupled electrochemical water splitting	21

CONTENTS (Continued)

	Page
2.3.1 Conventional and decouple electrolysis	21
2.3.2 Soluble redox mediator	24
2.3.3 Solid state redox mediator	27
2.4 Oxygen vacancies and in transition-metal oxides and photoelectron chemical/ photocatalyst	30
2.4.1 Photo-induced oxygen vacancy in transition-metal oxides	30
2.4.2 Role of surface oxygen vacancy in photoelectrochemical	32
2.5 Application of CuO and Cu ₂ O on photoelectrochemical water splitting	33
III RESEARCH METHODOLOGY	36
3.1 Synthesis and characterization of CuO-Cu(OH) ₂ electrode	36
3.1.1 Preparation of CuO-Cu(OH) ₂ on copper foil	36
3.1.2 Electrode characterization	37
3.1.2.1 Field emission scanning electron microscopy (FE-SEM)	38
3.1.2.2 X-ray diffractometer	39
3.2 Electrochemical characterization and electrode activation	41
3.2.1 Electrochemical characterization under dark and solar irradiation	41
3.2.2 Electrode activation	42
3.3 Two-cell water electrolysis system	43
3.3.1 Considerations for selecting the redox mediator electrodes	43
3.3.2 Fabrication of two-cell water electrolysis system	44
3.4 Performance of two-cell water electrolysis system and photoenhanced pure gas production	45

CONTENTS (Continued)

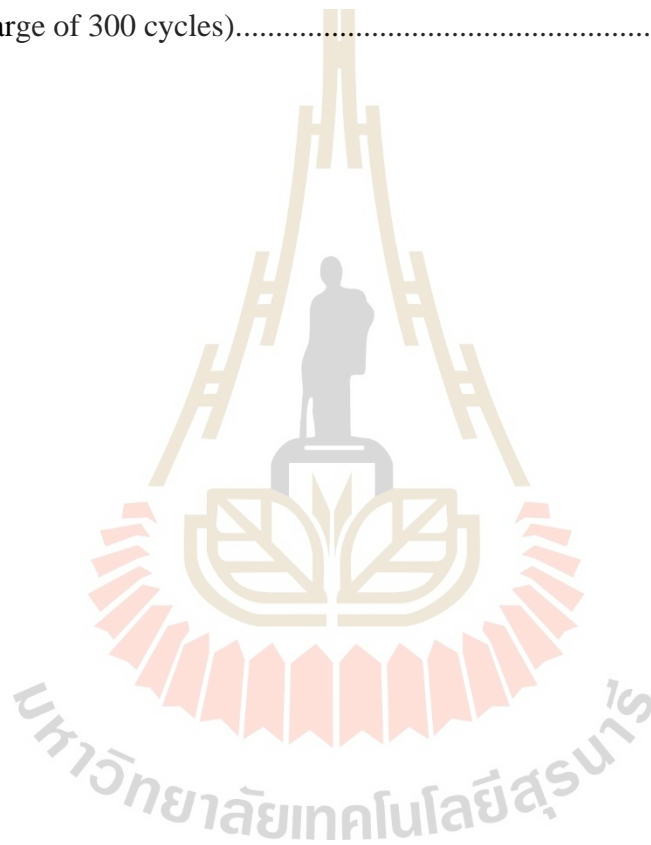
	Page
3.4.1 Gas measurement and Faradaic efficiency	46
3.4.2 <i>In-situ</i> gas chromatography	47
3.5 <i>In-situ</i> X-ray absorption spectroscopy (XAS)	48
3.6 Photoemission spectroscopy (PES)	54
IV RESULTS AND DISCUSSION	57
4.1 Characterization of the CuO-Cu(OH) ₂ electrodes	58
4.1.1 Scanning electron microscopy	58
4.1.2 EDS analysis	60
4.1.3 XRD analysis	61
4.2 Electrochemical properties of the electrodes	64
4.2.1 Cycle voltammogram (CV) and galvanostatic and charge– discharge (GCD) measurements	64
4.2.2 Mediator electrode activation	66
4.2.3 Electrochemical properties of the electrodes under dark and sunlight illumination	68
4.2.4 Electrochemical impedance spectroscopy study of the electrodes	73
4.2.5 UV-visible spectra	74
4.3 The operation of two-cell water electrolysis system	75
4.3.1 Redox mediator electrode optimization	79
4.4 Gas measurement and Faradaic efficiency	83
4.5 <i>In-situ</i> gas chromatography	84

CONTENTS (Continued)

	Page
4.6 Gases production of two-cell water electrolysis under dark and light illumination	85
4.6.1 Chronoamperometry measurement (V constant)	85
4.6.2 Chronopotentiometry measurements (I constant)	89
4.7 <i>In-situ</i> X-ray absorption spectroscopy (XAS)	90
4.8 Photoemission spectroscopy analysis	93
4.9 Discussion	95
V CONCLUSIONS	100
REFERENCES	102
APPENDIX	118
CURRICULUM VITAE	131

LIST OF TABLES

Table		Page
1	EDS data recorded on the as-prepared sample	61
2	EDS data recorded on the sample after activation process (charge- discharge of 300 cycles).....	61



LIST OF FIGURES

Figure	Page
1.1 Schematic of water electrolysis system.	2
1.2 The schematic of PEM electrolyzer system using a soluble redox mediator separated H ₂ and O ₂ production steps.	3
1.3 Schematic of the ECPB-based water splitting.	3
1.4 Mechanism of separated H ₂ and O ₂ production in alkaline water electrolysis system.	4
1.5 (a) Schematic demonstrated the photoelectrochemical water. (b) The concept of a standalone solar hydrogen station with a photoelectron chemical system to Producing O ₂ and a Centralized H ₂	5
2.1 The Ragone plot shows a performance of the energy density versus power density for different energy storage technologies.	9
2.2 The schematics of energy storage devices. (a) An electrical double layer capacitor (EDLCs), (b) a pseudocapacitor (MnO ₂ depicted center) and (c) a Li-ion battery (LiCoO ₂).	11
2.3 Schematic illustration of the mechanism of conventional Li-ion battery using a graphite anode and LiCoO ₂ cathode material.	12

LIST OF FIGURES (Continued)

Figure	Page
2.4	Illustration of the potential drop that occurs between the charging and discharging processes. Internal resistances are a primary cause of the IR decrease, which causes side effects that are potential safety concerns.13
2.5	Supercapacitors and batteries have different electrochemical behavior, such as the Voltammogram (a) and (b) and the Galvanostatic Charge-Discharge (c) and (d) curves. ESR is equivalent series resistance.14
2.6	The schematic of the photo-charging Li-S battery. (a) The battery is composed of a Li anode immersed in an organic electrolyte. (b) Discharging is identical to that of a standard aqueous Li-S battery. 18
2.7	The schematic of photo-assisted rechargeable Li-O ₂ battery comprises a Li anode in non-aqueous electrolyte and charge/discharge curves for a Li-O ₂ battery with/without an I-ion redox mediator. 19
2.8	The charging process for the electrode reactions in a supercapacitor is shown schematically with/without light illumination 20
2.9	(a) Cyclic voltammetry (CV) curves of the NPC@Cu ₂ O electrode at 10 mV/s under dark and light illumination. (b) Galvanostatic charge-discharge profiles (GCD) at 1 A/g under dark and light illumination. 21
2.10	Under acidic conditions, a comparison of (a) conventional (coupled) water electrolysis vs (b) Decoupled water electrolysis: OER and (c) decoupled water electrolysis: HER. 24

LIST OF FIGURES (Continued)

Figure	Page
2.11	A photoelectrochemical cell that created by (Bloor et al., 2016) for the reduction of phosphomolybdic acid at a carbon cathode that is powered by visible light irradiation of a WO ₃ photoanode. 26
2.12	Goodwin and Walsh utilized a closed bipolar electrode cell method to spatially isolate O ₂ and H ₂ generation from water electrolysis. 27
2.13	The mechanism of NiOOH/Ni(OH) ₂ as a solid decoupling agent electrode is shown schematically. The OER is linked to the reduction of NiOOH (red arrows), whereas the HER is coupled to the oxidation of Ni(OH) ₂ (green arrows). 29
2.14	Variation in the charge density of 2DEG in response to different UV irradiation doses. The APES results in (a)–(d) correspond to the given irradiation doses in SrTiO ₃ 30
2.15	(a) Schematic of capacitance measurement allowing for light irradiation of the top electrode. (b) Capacitance of the BLFO as a function of UV laser irradiation at $f = 2$ kHz with a time scale of 480 s. 31
2.16	Evolution of the valance band (VB) spectra of SrTiO ₃ and Bi _{0.95} La _{0.05} FeO ₃ , respectively, from the pristine cleaved surface to the exposed surface. 31

LIST OF FIGURES (Continued)

Figure	Page
2.17	(a) Photocurrents curves for (1) Ag-BiVO ₄ -OV, (2) BiVO ₄ -OV, (3) Ag-BiVO ₄ , and (4) BiVO ₄ electrodes under visible light ($\lambda > 420$ nm). (b) The schematic diagram shows the mechanism of charge separation and the photocatalytic reaction of Ag-BiVO ₄ -OV, under simulated solar light irradiation (Shi et al., 2018). 32
2.18	Band edge positions of semiconductors in contact with an aqueous electrolyte at pH = 0 compared to NHE and vacuum. Additionally, the redox potentials of HER and OER are given for comparison. 33
2.19	The schematic show energy band structure of the Cu ₂ O/CuO bilayered composite in contact with solution during PEC HER. 34
2.20	The activity and stability of the Cu ₂ O/CuO bilayered composites at different pH levels in 0.5M Na ₂ SO ₄ solution. 35
3.1	Cu(OH) ₂ -CuO electrode preparation (a) surface oxidation of Cu in alkaline solution (b) As-prepared Cu(OH) ₂ -CuO electrode. 37
3.2	The interaction of electron beam on the sample (a) the signal produced by the electron interaction in the thin sample; (b) the absorption of secondary electrons, backscattered electrons, and X-rays in the thick sample, by inelastic scattering within the interaction volume will limit the depth of specimens (Inkson, 2016). 39
3.3	X-ray emission caused by electrons (a) Characteristics of X-ray. (b) A schematic of an energy-diffusing X-ray (EDX). 40

LIST OF FIGURES (Continued)

Figure	Page
3.4	(a) Bragg's diffraction law for two identical wavelengths and phased beams. (b) Schematic setup of the XRD measurement system. 41
3.5	Three-electrode electrochemical cell setup. (a) Schematic of three-electrode system. Electrochemical measurement under (b) dark, (c) laser light (450 nm) and (c) solar irradiation. 43
3.6	The membrane-free configuration for alkaline water electrolysis in separate oxygen and hydrogen cell. (a) Schematic illustration and (b) experimental setup of a two-cell water electrolysis system after operated 20 minutes, respectively. 45
3.7	(a) and (b) Measurement setup and schematic illustration of a typical custom-built devices for measured volume of gases, respectively. 47
3.8	Photograph of <i>in-situ</i> GC measurement system. 47
3.9	Schematic illustration and Experimental setup of a two-cell water electrolysis system, respectively. 48
3.10	The X-ray absorption near edge structure (XANES) and extended X-ray absorption fine structure (EXAFS) spectroscopies. 50
3.11	(a) XAS diagram, showing the pre-edge, X-ray absorption near edge structure (XANES), and X-ray absorption fine structure (EXAFS) areas. (b) The spectrum of XAS. (c) Three distinct ways of XAS detection: transmission, fluorescence, and electron yield. 52

LIST OF FIGURES (Continued)

Figure	Page
3.12	(a) <i>In situ</i> Cu K-edge fluorescence measurement setup, (b) schematic, and (c) process of electrolysis operation of mediator electrode during charging and discharging under dark and blue light illuminations in two-cell water electrolysis at 3 V.53
3.13	XAS setup at beamline 5.2.53
3.14	A typical XPS setup is shown schematically. It includes a photon source (X-rays, UV-light, laser, or synchrotron radiation), sample manipulation with several degrees of freedom in linear and rotational directions, electron optics, and dispersive energy analyzer, and a detector. XPS spectra (intensity vs. binding energy) of four different metals are illustrated with their element-specific distribution of core-level photoemission.55
3.15	The type of core-level spectroscopies: ultraviolet photoelectron spectroscopy (UPS), X-ray photoelectron spectroscopy (XPS), X-ray absorption spectroscopy (XAS) and X-ray emission spectroscopy (XES).56
4.1	SEM micrographs of As-prepared electrode. (a) photograph of electrode before and after surface oxidation thick films. (b) pre-cleaned Cu foil. (c)-(f) As-prepared electrode.59
4.2	SEM micrographs of activated electrode.60

LIST OF FIGURES (Continued)

Figure	Page
4.3	EDS analysis. Quantitative chemical composition analysis of as-prepared and after activation process electrodes taken 4 selected sites as shown in the SEM image ((a) and (b)). (a) The SEM image of as-prepared electrode. (b) The SEM image of activated electrode. Table 1 EDS data recorded on the as-prepared sample. Table 2 EDS data recorded on the sample after activation process (charge-discharge of 300 cycles). 61
4.4	XRD patterns of as-prepared, charged (CuO-Cu(OH)_2) and discharged (Cu_2O) electrodes. 63
4.5	Electrochemical properties of electrode in potential window of -2 V to 0.9 V. (a) Cyclic voltammetry of electrode at different scan rate. (b) Variation of specific capacitance as a function of scan rate. 65
4.6	Electrochemical properties of electrode in potential window of 0 V to 0.9 V. (a) Cyclic voltammetry of electrode at different scan rate. (b) Variation of specific capacitance as a function of scan rate. 65
4.7	Electrochemical properties of electrode. (a) Charge-discharge curves of electrode at different current densities. (b) Variation of specific capacitance as a function of current density. 67
4.8	Electrochemical properties of electrode. (a) Charge-discharge curves of electrode at different current densities. (b) Variation of specific capacitance as a function of current density. 67

LIST OF FIGURES (Continued)

Figure	Page
4.9	(a) CV curves of CuO-Cu(OH) ₂ electrode before and after activation process at 10 mV/s with potential range from -2 V to 1 V vs Ag/AgCl. (b) The cycling stability and galvanostatic discharge curves (inset) of CuO-Cu(OH) ₂ /Cu-foil electrode by charge/discharge measurement at 10 mA/cm ² and -1.3-0.6 V vs Ag/AgCl in 1 M NaOH. 68
4.10	Effect of sunlight on CuO-Cu(OH) ₂ /Cu ₂ O redox mediator electrode. (a), (b), and (c) CV curve of CuO-Cu(OH) ₂ electrode taken at the scan rate of 3, 10, 30 mV/s, respectively, under dark and sunlight illuminations. (d) Variation of specific capacitance as a function of scan rate under dark and sunlight illumination. 70
4.11	Effect of laser light (450 nm) on CuO-Cu(OH) ₂ /Cu ₂ O redox mediator electrode. (a) and (b) CV curve of CuO-Cu(OH) ₂ electrode at 5 and 30 mV/s, respectively, in three electrode electrochemical under dark and laser light illumination. 71
4.12	(a)-(c) CV curves of the half-cell electrode under dark and sunlight illumination at 10, 20, and 30 mV/s, respectively. (d) Specific capacitance of CuO-Cu(OH) ₂ electrode under dark and solar irradiation. 72
4.13	(a) and (b) Galvanostatic charge-discharge profiles under dark and sunlight condition at constant currents in a potential range of 0 to 0.6 V and -1.5 to 0.5 V vs Ag/AgCl, respectively. (c) Specific capacitance as a function of current density under a dark condition and a light illumination. 73

LIST OF FIGURES (Continued)

Figure	Page
4.14	Electrochemical impedance spectroscopy study of electrodes in a three-electrode system. (a) EIS plot of the as-prepared and activated electrodes after charge-discharge of 5, 30 and 400 cycles. (b) EIS plot of electrode under dark and light irradiation. 74
4.15	UV-vis spectra of as-prepared (black dash line), CuO-Cu(OH) ₂ (blue line) and Cu ₂ O (red line) electrodes dispersed in DI water. 75
4.16	Our two-cell water electrolysis system setup. (a) Schematic of two-cell water electrolysis system with CuO-Cu(OH) ₂ /Cu ₂ O redox mediator electrodes. (b) The photograph of the Cu ₂ O and CuO-Cu(OH) ₂ redox mediator electrodes after electrolysis at 1.5 hours. 77
4.17	The potentials of the electrodes in hydrogen and oxygen cells of two-cell water electrolysis system. The potential of mediator electrodes during electrolysis are shown by blue and pink line curves, respectively. 78
4.18	Two-cell water electrolysis test with different charge of mediator electrodes. The chronopotentiometry curve (voltage as a function of time) of the electrolysis system at a constant applied current of 40 mA (current density of 4 mA/cm ²). (a) The mediator electrodes were charged to 22.4 mAh, the electrolysis cycle was short (34 mins). (b) The longer electrolysis cycle of >1 h achieved by charging the mediator electrodes to 63.6 mAh. 79

LIST OF FIGURES (Continued)

Figure	Page
4.19 (a) Charge and discharge of redox mediator electrode under dark and solar irradiation. A sample was charged at a current of 40 mA for 4 hours to reach the full charge depth, and then discharged at 40 mA to a cutoff potential of -1.3 V (vs. Ag/AgCl). The total electrode capacity was estimated at 112.8 mAh. This experiment was repeated four times at each charge/discharge process. (b) A schematic of the charge depth test setup of the two-cell water electrolysis.	82
4.20 (a) Electrochemical profile of CuO-Cu(OH) ₂ electrode at different charge depths tested in two-cell water electrolysis at a charge/discharge current of 40 mA. (b) Charging efficiency as a function of the electric charge transferred during charging step.	82
4.21 The volume of effluent gas produced at the headspace of the oxygen and hydrogen cells (blue squares and brown triangle) as a function of time during a two-cell water electrolysis test at a constant current of 40 mA (current density of 4 mA/cm ²). The blue and brown lines show the theoretical volume of the respective gases, calculated based on the current×time product assuming Faradaic efficiency of 100%. (b) Schematic illustration of a typical custom-built devices for gas volume measurement	84
4.22 <i>In situ</i> purity measurement of H ₂ and O ₂ . (a) Chromatogram of outlet gas taken from the headspace of the hydrogen cell and (b) the oxygen cell.	85

LIST OF FIGURES (Continued)

Figure	Page
4.23	(a) H ₂ and O ₂ production that evolved during operation at a potential bias of 2 V in two-cell water electrolysis which was setup according to the schematic diagram in (b). 86
4.24	Effect of sunlight on CuO-Cu(OH) ₂ /Cu ₂ O redox mediator electrode. (a) and (b) show H ₂ and O ₂ production in two-cell water electrolysis system operated at a potential application of 2 V under dark and sunlight illumination. (c) Current density of two-cell water electrolysis system under sunlight conditions. The inset shows the additional current density depending on light on/off. (d) The schematic of two-cell water electrolysis operation under solar irradiation. 88
4.25	The amount of gases from the sealed cells of two-cell water electrolysis system with light irradiated on different mediator electrode. (a) and (b) The amount of H ₂ and O ₂ , respectively, during electrolysis at V=3 V. (c) and (d) The amount of H ₂ and O ₂ , respectively, during electrolysis at V=2.5 V. 89
4.26	The applied potential as a function of time during operated two-cell water electrolysis system at a constant current of 40 mA (2 mA cm ⁻²) under dark and solar irradiation. 90

LIST OF FIGURES (Continued)

Figure	Page
4.27 Electronic structure of CuO-Cu(OH) ₂ /Cu ₂ O redox mediator electrode. (a) In situ Cu K-edge fluorescence XANES spectra of mediator electrode during charging and discharging under dark and light illuminations in two-cell water electrolysis at 3 V. The changing of oxidation state for each condition is shown in the inset. (b) Changing absorption edge positions and of redox mediator electrodes during charging and discharging under dark and light illumination.	92
4.28 FT EXAFS structures of redox mediator electrodes during charging (a) and discharging (b) under dark and light illumination.	93
4.29 Electronic structure of the redox mediator electrode. (a) and (b) Evolution of the valence band (VB) spectra of Cu ₂ O and CuO-Cu(OH) ₂ redox mediator electrode from the pristine fractured surface to the light irradiated surface, respectively. The inset in (a) shows the evolution of the in-gap state with increasing exposure time.	94
4.30 XPS spectra of mediator electrodes measured under dark and light condition. (a), (b) and (c) Cu3s3p, O1s and C1s, respectively, of Cu ₂ O electrode. (d), (e) and (f) Cu3s3p, O1s and C1s, respectively, of CuO-Cu(OH) ₂ electrode.	95
4.31 Schematic diagram illustrating the proposed mechanism of charge separation and photooxidation of Cu ₂ O to CuO.	99

LIST OF ABBREVIATIONS

2DEG	Two-dimensional electron gas
BE	Binding energy
CV	Cyclic voltammetry
CB	Conduction band
ECPB	Electron-coupled proton buffer
EDLC	Electrical double layer capacitors
EIS	Electrochemical impedance spectroscopy
eV	Electron volt
EXAFS	Extended X-ray absorption fine edge structure
EDS	Energy dispersive spectroscopy
FE-SEM	Field-emission scanning electron microscopy
GCD	Galvanostatic charge-discharge
HER	Hydrogen evolution reaction
OER	Oxygen evolution reaction
PEM	Proton exchange membrane
PES	Photoemission spectroscopy
SHE	Standard hydrogen electrode
SOC	State of charge
TMO	Transition metal oxide
UHV	Ultra-high vacuum

LIST OF ABBREVIATIONS (Continued)

UV	Ultraviolet light
UV-vis	UV-visible spectroscopy
VBM	Valence band maximum
VB	Valence band
XANES	X-ray absorption near edge structure
XAS	X-ray absorption spectroscopy
XRD	X-ray diffraction
XPS	X-ray photoelectron spectroscopy

CHAPTER I

INTRODUCTION

1.1 Background and Motivation

Hydrogen is considerable alternatives to unsustainable fossil fuels (Armaroli and Balzani, 2011; Le Goff et al., 2009). Currently, around 90% of the H₂ supply is produced via the fossil fuels reformation (Reece et al., 2011; Tachibana et al., 2012), which is both unsustainable and results in a net increase in CO₂. The only technique of hydrogen synthesis that is not dependent on fossil fuels is the electrolysis of water ($2\text{H}_2\text{O} \rightarrow 2\text{H}_2 + \text{O}_2$). The water electrolysis could be performed at room temperature, which the only required are water and energy in the form of electricity (Holladay et al., 2009). Therefore, electrochemical water electrolytic is attracting wide attention. However, both improving the yield of high-purity H₂ and reducing the production cost remain challenges to the application of water electrolysis system for large-scale hydrogen production. Therefore, water electrolysis system in separate cells combined with a renewable power source (solar energy) provides an alternative way to efficient device design and reduction of cost of the H₂ production.

The hydrogen and oxygen gases are simultaneously produced within same cell in the conventional water electrolysis. Mixing of these gases is occurs during electrolysis. They were resulting in degradation of electrolyzers and raising safety concerns (Figure 1.1a).

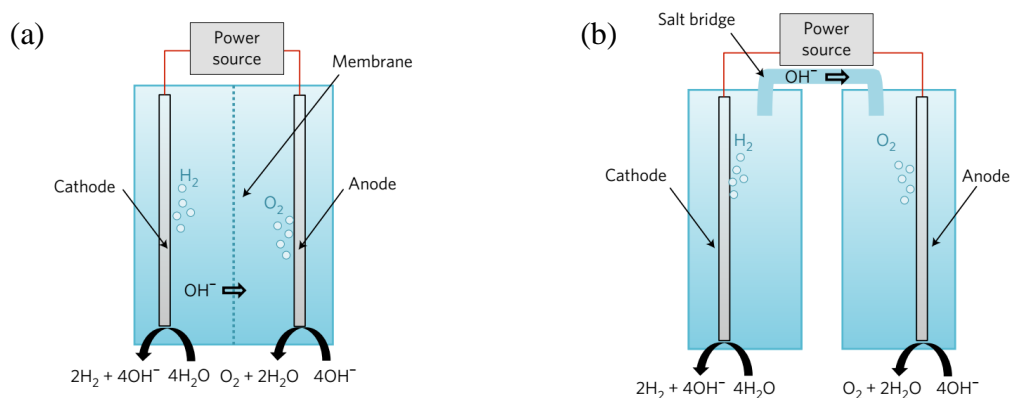


Figure 1.1 Schematic of water electrolysis system. (a) Conventional alkaline water electrolysis cell. (b) Alkaline water electrolysis cell with a salt bridge (Landman et al., 2017).

Therefore, several methods to prevent the mixing of gaseous H_2 and O_2 products are proposed (Chen et al., 2016; Dotan et al., 2019; Goodwin and Walsh, 2017; Hou et al., 2018; Landman et al., 2017; Rausch et al., 2014; Symes and Cronin, 2013; You and Sun, 2018). Cronin's group introduced a method to separate gases produced in the conventional proton exchange membrane (PEM) water electrolysis process (Rausch et al., 2014). They used a silicotungstic acid (soluble molecular redox mediator) as mediates the electron-coupled proton exchange between the oxygen and hydrogen evolution reactions (OER and HER respectively) (Figure 1.2 and 1.3). Water is oxidized at the anode to produce O_2 , protons, and e^- . Simultaneously, the silicotungstic acid redox medium is reversibly reduced and protons at the cathode are employed to direct production of H_2 without additional energy input. While PEM water electrolysis devices provide a number of benefits, as stated in Rausch et al., 2014, their application remains limited by the rather low efficiency and high cost of the both Pt catalysts and membranes (You and Sun, 2018).

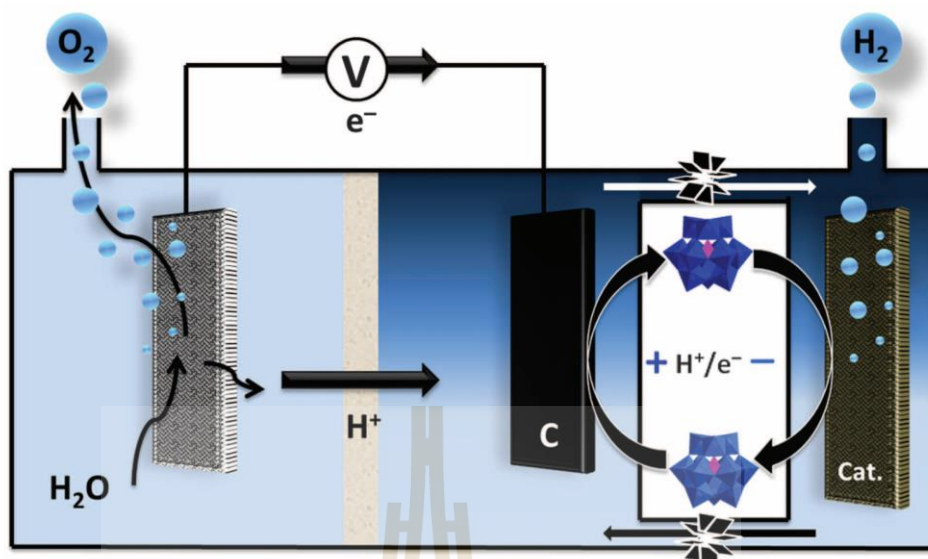


Figure 1.2 The schematic of PEM electrolyzer system using a soluble redox mediator separated H_2 and O_2 production steps (Rausch et al., 2014).

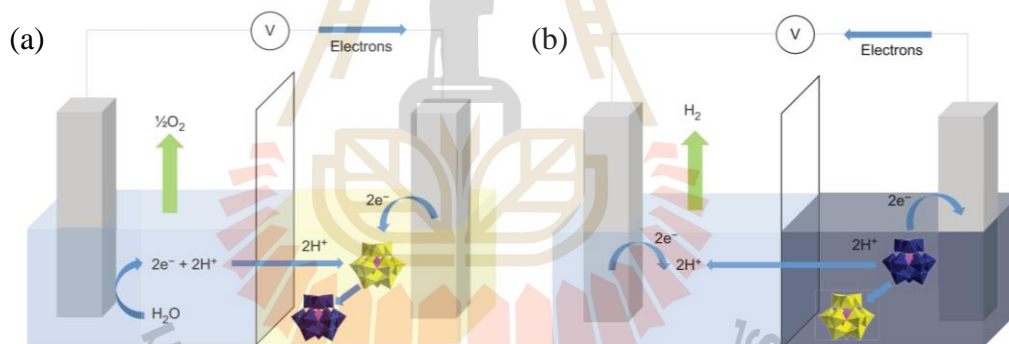


Figure 1.3 Schematic of the ECPB-based water splitting. (a) The oxidation reaction of H_2O at the anode obtains O_2 , H^+ , and e^- . The e^- move through the external circuit, while the H^+ diffuse through the membrane that separates the sections. The electrons reduced ECPB in the other section and simultaneously receive protons to charge-balancing. The color of ECPB changes from yellow to dark blue. (b) The H^+ released from reoxidation of the ECPB were migrating through the membrane to the other electrode. These protons combine with the e^- removed from the ECPB to generate H_2 . The color of ECPB reverses to original yellow color (Symes and Cronin, 2013).

To overcome this problem, the separation of hydrogen and oxygen production using Ni(OH)₂/NiOOH redox mediator electrodes in alkaline aqueous solution was proposed (Chen et al., 2016; Dotan et al., 2019; Landman et al., 2017) (Figure 1.4). In comparison with PEM water electrolysis, the overall efficiency of water electrolysis in alkaline media is better than that in acidic media. In contrast, alkaline water electrolysis is a low-cost characteristic because it only used a non-precious catalyst and a low-cost porous separator (You and Sun, 2018).

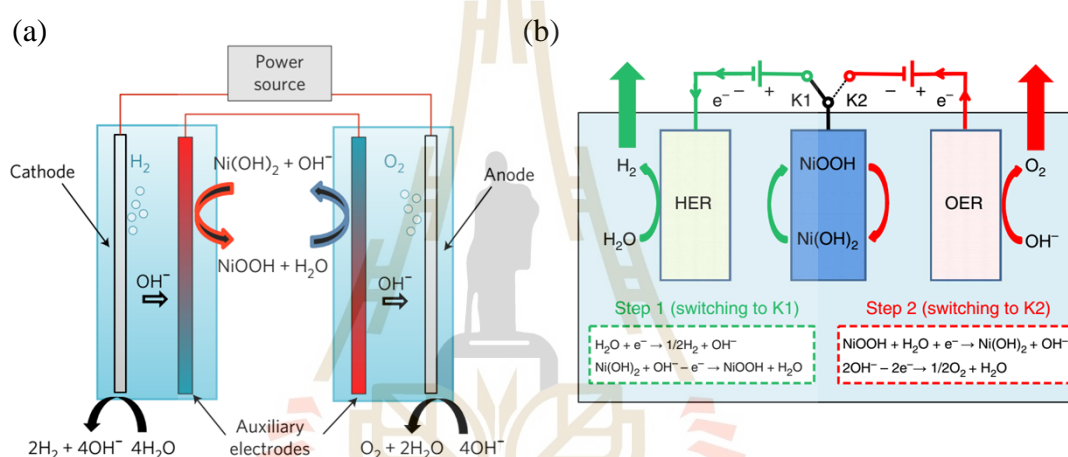


Figure 1.4 Mechanism of separated H₂ and O₂ production in alkaline water electrolysis system. (a) The two-cell water electrolysis using Ni(OH)₂/NiOOH as auxiliary electrodes. The H₂ and O₂ can occur simultaneously in separate hydrogen and oxygen cells (Landman et al., 2017). (b) The operation mechanism of the water electrolysis cell which split into a two-step. Step 1 is H₂ production (switching to K1), H₂O is reduced on the HER electrode (H₂O + e⁻ → 1/2H₂ + OH⁻) while Ni(OH)₂ electrode is oxidized to NiOOH (Ni(OH)₂ + OH⁻ - e⁻ → NiOOH + H₂O). Step 2 is O₂ production (switching to K2), the NiOOH electrode is reduced to Ni(OH)₂ (NiOOH + H₂O + e⁻ → Ni(OH)₂ + OH⁻) and anodic OH⁻ are oxidized to generate O₂ on the OER electrode (2OH⁻ - 2e⁻ → 1/2O₂ + H₂O) (Chen et al., 2016).

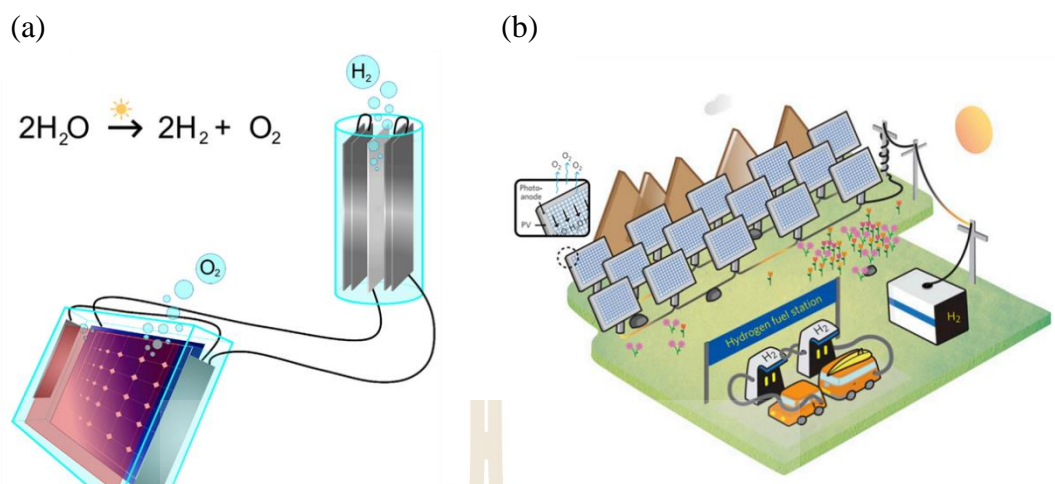


Figure 1.5 (a) Schematic demonstrated the photoelectrochemical water splitting with separate O_2 and H_2 cells. Si PV cells with Fe_2O_3 (hematite) photoanodes oxidize H_2O to generate O_2 using OH^- ions that are released from $\text{NiOOH} + \text{H}_2\text{O} + \text{e}^- \rightarrow \text{Ni}(\text{OH})_2 + \text{OH}^-$ reaction on an auxiliary electrode in the same cell. Simultaneously in another cell, H_2 is generated by reducing H_2O at the cathode. The $\text{Ni}(\text{OH})_2$ electrode absorbed OH^- ions generated at the cathode to oxidize $\text{Ni}(\text{OH})_2 \rightarrow \text{NiOOH}$. (b) The concept of a standalone solar hydrogen station with a photoelectrochemical system to producing O_2 and a centralized H_2 (Landman et al., 2020).

The CuO , $\text{Cu}(\text{OH})_2$, and Cu_2O electrodes have been widely used in rechargeable batteries and pseudo-capacitors. They store charge by reacting with OH^- ion in alkaline media and show high redox reaction and capacitance (Senthilkumar et al., 2015; Xu et al., 2019; Xu et al., 2016; Xu et al., 2015). Although CuO and $\text{Cu}(\text{OH})_2$ are slightly inferior to $\text{Ni}(\text{OH})_2$ in terms of capacity, it is outstanding in cycling durability. Therefore, the redox-reversible $\text{CuO-Cu}(\text{OH})_2/\text{Cu}_2\text{O}$ electrodes are suitable to be used as an ion-exchange mediator in our two-cell water electrolysis system. The electrons transfer from one mediator electrode to another by the charge and discharge processes

of mediator electrodes. Therefore, the capacitance of mediator electrodes has an important influence on the electrolysis rate in the two-cell water splitting system. Many studies report that charging and discharging of supercapacitive hydroxides and oxides under illumination can provide a higher current density and capacitance due to photogenerated electron-hole pairs in the electrode materials (An et al., 2019; Kalasina et al., 2017; Kalasina et al., 2018; Safshekan et al., 2017; Xia et al., 2012). Compared with NiOOH/Ni(OH)₂, using CuO-Cu(OH)₂/Cu₂O as mediator electrodes could easily enhance the performance of a two-cell water electrolysis system by illumination due to its narrow bandgap. It is therefore strongly absorbing of solar irradiation (Dias et al., 2015; Luo et al., 2016; Shu et al., 2017; Zhang and Wang, 2012), which enables the generation of electron-hole pairs for enhanced redox and charge transfer in the water splitting system.

In this work, we study in fundamental of a battery electrode and present a concept providing a significant enhancement in the production of pure gases in a two-cell water electrolysis system by using charge-discharge Cu₂O/CuO-Cu(OH)₂ redox mediator electrodes under solar irradiation. In our proposed system, the hydrogen, and oxygen cells are separated by using CuO-Cu(OH)₂/Cu₂O mediator electrodes substitute membrane separator for ion exchange between anode and cathode. The CuO-Cu(OH)₂ convert to Cu₂O during O₂ production at the anode ($4\text{OH}^- \rightarrow \text{O}_2 + 2\text{H}_2\text{O} + 4\text{e}^-$), while Cu₂O simultaneously converts to CuO-Cu(OH)₂ during H₂ production at the cathode ($4\text{H}_2\text{O} + 4\text{e}^- \rightarrow 2\text{H}_2 + 4\text{OH}^-$). This system, the CuO-Cu(OH)₂ with Cu₂O, has both photo-sensitive and pseudo-capacitive properties. The capacitance of mediator electrodes is improved greatly under light illumination by the creation of surface oxygen vacancies in the Cu₂O electrode. Therefore, the solar power, without the need for photovoltaics,

can be captured and directly stored. This concept provides a new way of sustainable hydrogen production while reducing costs for large-scale utilization.

1.2 Research objective/ Purposes of the study

In this work, we aim to study the battery reaction and sunlight sensitivity of the redox mediator to enhance the generation of pure gas in electrolysis cells. The objectives are listed as follows,

- 1.2.1. To study structure, morphology, and electrochemical properties of redox electrodes, and use them in hydrogen and oxygen cells for water splitting.
- 1.2.2. To enhance the production of pure hydrogen and oxygen gases by sunlight.
- 1.2.3. To study the electronic structure of materials for battery electrodes.

1.3 Scope and limitations

- 1.3.1. Redox electrodes will be prepared, and their structures and morphology will be characterized by X-ray diffraction (XRD), Field-emission scanning electron microscopy (FE-SEM), Energy Dispersive Spectroscopy (EDS). Their electrochemical properties will be also studied when they are used as a redox mediator electrode.
- 1.3.2. Two-cell water electrolysis system will be constructed by using the redox electrodes as mediator to separate hydrogen and oxygen cells. The effects of sunlight on sensitivity and reactivity of these electrodes will be investigated.

1.3.3. The electronic structure of the electrode materials in battery will be studied by photoemission spectroscopy.

1.4 Anticipated outcomes

1.4.1. To separate hydrogen and oxygen cells by using redox mediator electrodes.

1.4.2. To enhance pure hydrogen and oxygen gas in electrolysis cells and reducing the production cost by using sunlight sensitivity of redox couple mediator electrode.

1.4.3. Fundamental understanding of the working mechanism, characterized by photoemission spectroscopy technique.

1.4.4. Publication in ISI journals.

1.5 Outlines of thesis

This thesis is separated into five chapters. The first chapter is the introduction of the thesis. Chapter II describes a brief literature review of electrochemical energy storage, battery electrodes, and water electrolysis systems. Furthermore, the theory approaches concerning the physical and electrochemical properties are also described in this section. Chapter III presents the preparation and characterization methods of the electrodes. Moreover, the fabrication of a two-cell water electrolysis system and all measurement techniques used in this work are also described in this chapter. The obtained results and discussions of the results are presented in Chapter IV. Finally, the conclusions, suggestions, and future works are proposed in Chapter V.

CHAPTER II

LITERATURE REVIEWS

2.1 Brief overview of electrochemical energy storage

Among energy storage technologies, batteries and supercapacitors have been widely applications. The Ragone plot shows the difference in performance between batteries and supercapacitor, which compares the energy densities of various energy storage devices. In that chart, the value of the energy density (in Wh/kg) is plotted vs the power density (in W/kg), as shown in Figure 2.1.

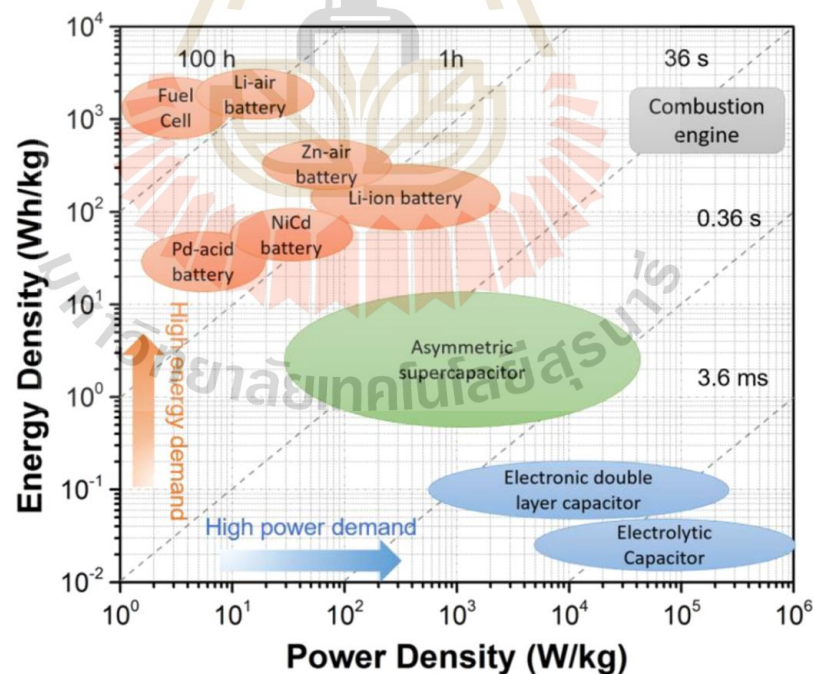


Figure 2.1 The Ragone plot shows a performance of the energy density versus power density for different energy storage technologies (Shao et al., 2018).

Lithium-ion batteries are used in various electronic devices due to their high energy density, which is approaching 180 Wh/kg (Aricò et al., 2005; Dunn et al., 2011). However, operating at high power remains a safety concern due to the resistive losses from electron and ion transport leading to heat generation and dendrite formation (Choi et al., 2012; Hu and Xu, 2014).

To consider high power to high energy, there are three electrochemical energy storing technologies (Simon and Gogotsi, 2008): electrical double layer capacitors (EDLCs) (Pandolfo and Hollenkamp, 2006), pseudocapacitors, and batteries. Both EDLCs and pseudocapacitors are called supercapacitors. EDLC store charge by electrostatic and are composed of porous active material (carbon) electrodes that acts as a store of charge, and an electrolyte as a medium carries an electrically charged electrode. While an electric current passed into an EDLC, the positive electrode pulls the negative electrons from the electrolyte to accumulate on the surface. Simultaneously, a negative electrode draws a positive charge to balance the electric charge at the surface of both electrodes (Figure 2.2a). Batteries store a charge through the conversion of electrical energy into chemical energy (Figure 2.2c). The electrical energy that was charging into the battery leading to arise a chemical reaction. The lithium ions flow out of the structure of the cathode material, then flows through the electrolyte and Intercalate to the structure of the anode material (Etacheri et al., 2011). Pseudocapacitors have behavior both a double-layer capacitance and surface intercalation. The energy density increases while keeping fast charge and discharge times comparable to an EDLC (Figure 2.2b).

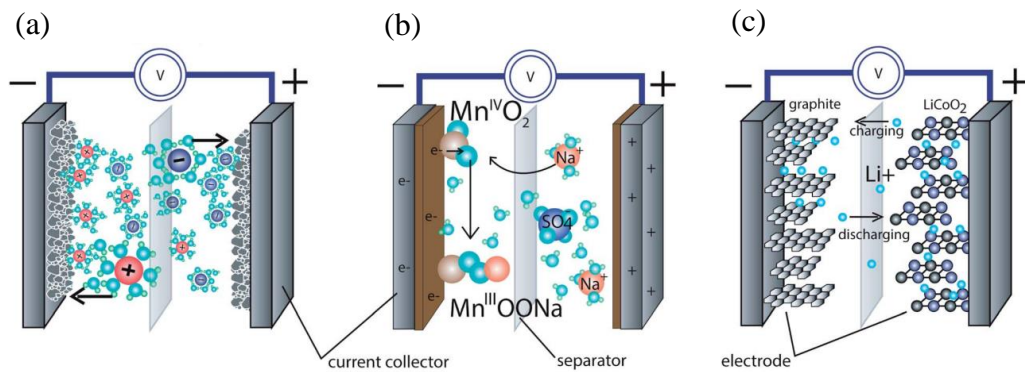


Figure 2.2 The schematics of energy storage devices. (a) An electrical double layer capacitor (EDLCs), (b) a pseudocapacitor (MnO_2 depicted center) and (c) a Li-ion battery (LiCoO_2) (Jost et al., 2014).

2.1.1 Rechargeable batteries (Li-ion battery)

Batteries with high performance such as energy density, long life cycle, and low cost have been the most attention in automotive applications and smart energy storage systems. A Li-ion battery is consisting of an anode, a separator, and a cathode (Figure 2.3). Graphite-based materials are widely used for anodes in the battery industry. All components are soaked in a liquid electrolyte, which is typically 1M LiPF_6 in a carbonate solvent mixture. The extracted Li^+ ions at the cathode flow through the electrolyte-soaked separator and intercalated into the anode material during the charging process. The process is reversed in discharging the battery (Goodenough, 2018; Ji et al., 2017).

In a conventional Li-ion battery, phase transitions occurring during the charge/discharge processes are associated with the extraction/insertion of Li-ions from the host material. The electrons are dragged from d -orbitals of transition metal ions in

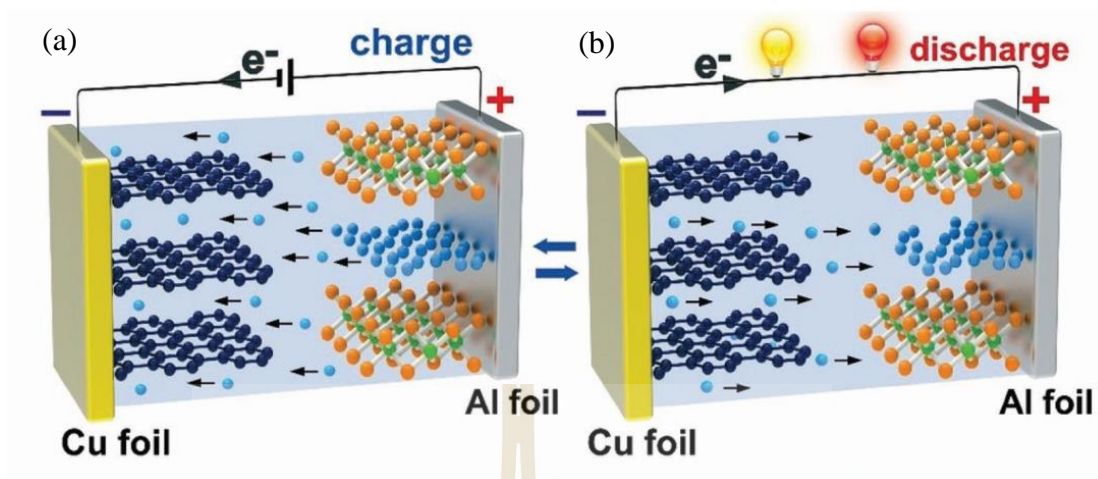


Figure 2.3 Schematic illustration of the mechanism of conventional Li-ion battery using a graphite anode and LiCoO_2 cathode material. (a) and (b) the charge/discharge process of the battery, respectively.

the charging process. Similarly, during discharge, Li-ions and electrons are transferred back into the relative lattice locations and original electronic orbitals. It is worth noting that the changes of energy associated with this reversible phase shift are distinct. Li-ions access the interstitial region of the host lattice during the discharge process, while electrons are absorbed into the transition metal d orbital, followed by decreasing energy and phase stabilization. In contrast, more energy is consumed as ions and electrons must be upheld from lower energy levels. In particular, during charging, more energy is used than during the discharge process-this different energy leading the potential gap between the charge and discharge curves. As a consequence of the higher overpotential, a phase transition occurs at the electrode during the charging process. The IR drop (shown in Figure 2.4) is caused by a change in internal resistance, which includes the resistance of the electrolyte, electrode materials, and various connections or auxiliaries. The disadvantages of the IR drop have increased energy consumption, which results in

a reduction in the efficiency of the battery, as well as safety concerns due to the emission of heat. These resistances may be reduced or eliminated to overcome side effects efficiently.

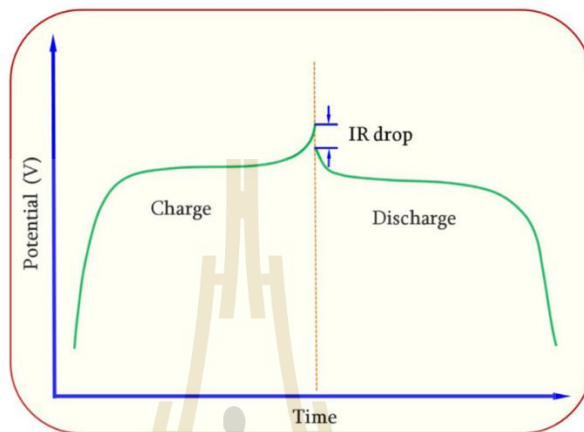


Figure 2.4 Illustration of the potential drop that occurs between the charging and discharging processes. Internal resistances are a primary cause of the IR decrease, which causes side effects that are potential safety concerns.

2.1.2 Supercapacitors

Supercapacitors are energy storage device that is charged through electrostatic or faradic electrochemical processes. The charges are stored in active materials such as porous carbons with a large surface area, metal oxides, and conducting polymers at the electrode-electrolyte interface. A positive and a negative electrodes are dipped to electrolyte and separated by an ion-permeable, electrically insulating separator (Shao et al., 2018). In comparison to batteries, supercapacitors provide rapid charge and discharge rates but have lower specific energy. Supercapacitors are advantageous in terms of efficiency, long life, high-performance stability, and operational safety. Supercapacitors differ from batteries in that they maintain a constant voltage increase

with continuous current charge, and their charges are stored and released from the electrodes, as shown in Figure 2.5.

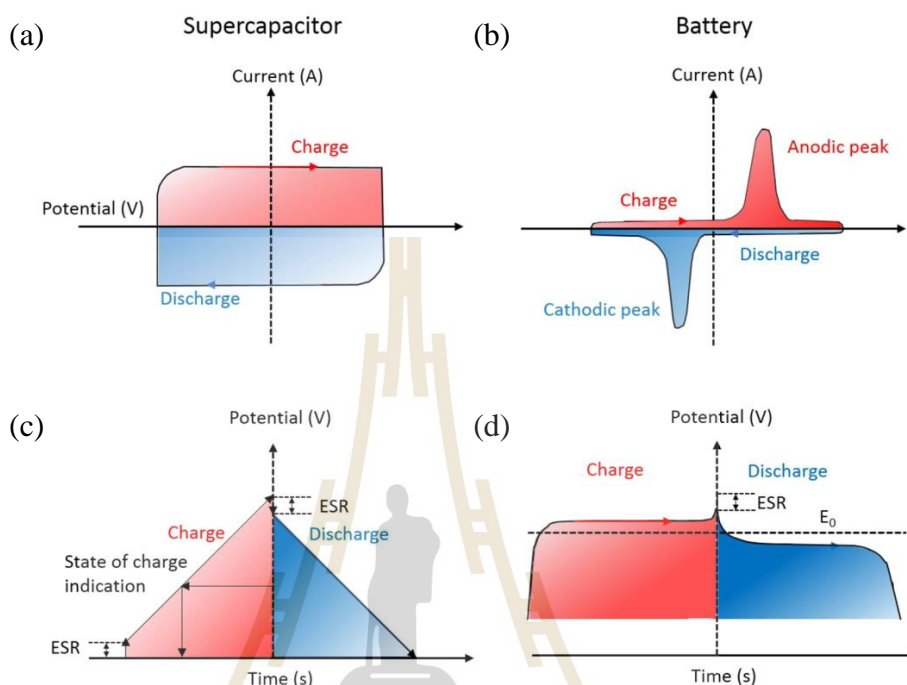


Figure 2.5 Supercapacitors and batteries have different electrochemical behavior, such as the Voltammogram (a) and (b) and the Galvanostatic Charge-Discharge (c) and (d) curves. ESR is equivalent series resistance (Shao et al., 2018).

Supercapacitors generally display a capacitance that is independent of the voltage being scanned. The cyclic voltammetry curve of a supercapacitor should thus keep a rectangular shape. At the same time, the current should remain nearly constant during the charge/discharge cycles. In contrast, batteries exhibit strong and distinct peaks indicative of considerable Faradaic reactions. A galvanostatic charge/discharge (GCD) curve of supercapacitor has a sloping curve with a constant slope value. A battery, on the other hand, usually shows a reasonably flat charge/discharge plateau when operated at a constant voltage stage. Because of the difference in the charge-

storage process, the amount of energy stored in these two types of electrodes is defined differently (capacitance versus capacity).

Calculating capacitance involves determining the ability of charge storage in an electrode. Capacitance is a charge value over a particular voltage range and could be calculate by using Equation 2.1.

$$C = \frac{\Delta Q}{\Delta U} \quad (2.1)$$

where ΔQ is the charge that stored in electrode and ΔU is the voltage supplied to the electrode. The capacitance (C) value is determined by assessing the charge-storage capacity within a specific voltage window, denoted by the Farad unit (F). For battery electrodes based on Faradaic reactions, the capacity is the amount of charge that store, measured in Coulombs (C) or milliampere-hours (mAh).

An electroconductive electrodes are dipped in an electrolyte solution. A double layer is produces due to the arrangement of charges at the electrode-electrolyte interfaces (Figure 2.2a) (Kötz and Carlen, 2000; Zhai et al., 2011; Zhang and Zhao, 2009). The surface area of the electrode materials used in the construction is highly effect on the effective specific capacitance of an EDLC, which could be approximated using Equation 2.2.

$$C = \frac{\epsilon_r \epsilon_0}{d} A \quad (2.2)$$

where ϵ_r is the relative permittivity related to the liquid electrolyte used, ϵ_0 is the permittivity of vacuum, A is the effective surface area of the electrode materials which are immersed to the electrolyte ions, and d is the effective charge separation distance between the electrical double layers.

Unlike EDLCs, pseudocapacitive electrode materials store charge through Faradaic processes involving redox reactions at the surface of active material (Figure 2.2b). This reaction is related to the electrode material's valence state due to electron transport. Officially, the term "pseudocapacitance" refers to electrode materials that exhibit capacitive electrochemical properties but store charge through charge-transfer Faradaic processes across the double layer.

The capacitance of a supercapacitor electrode is an important parameter represented in the amount of electrical charge stored at a given voltage. The specific capacitance of a supercapacitor is determined using Equation 2.1, $\frac{\Delta Q}{\Delta U}$, which reveals charge-storage capability within a specific voltage. In general, the findings of all three types of electrochemical tests may be used to determine this value. For most applications, external loads are usually supplied to supercapacitor, thus GCD functional behavior is closely related to electrochemical behavior. As a result, the GCD mode is the most widely used and accurate technique for determining capacitance. It can be used in Equation 2.3 to calculate it.

$$C = I \left(\frac{dV}{dt} \right)^{-1} \quad (2.3)$$

where I and $\frac{dV}{dt}$ are calculated from the slope of GCD curve. However, the same equation cannot be used to compute the "capacitance" of Faradaic materials based on their nonlinear GCD curves. On the other hand, Equation 2.3 cannot be used to a nonlinear GCD curve. The capacitance may also be estimated by integrating the CV curves using GCD discharge Equation 2.4.

$$C = \frac{1}{v\Delta V} \int IdV \quad (2.4)$$

where I denote discharge current, that is, the current below the x-axis, v denotes scan rate, and ΔV is the operational discharge potential range.

The energy stored in supercapacitors, referred to as the energy density, could provide by integrating the linear charge/discharge curves, triangular areas, as shown in Figure 2.5c. Thus, the energy density can be determined using

$$E = \int QdV = \int_0^{V_0} CVdV = \frac{1}{2}CV^2 \quad (2.5)$$

However, because of the nonlinear change in V , the energy density of a hybrid capacitor and battery (Figure 2.6d) with a nonlinear GCD curve cannot be evaluated using Equation 2.5. Therefore, the equation should be modified in this case.

$$E = \int QdV = \int_{t_1}^{t_2} IV(t)dt \quad (2.6)$$

After the initial IR drop, all times of discharge ($t_{discharge}$) and discharge voltages ($V(t)$) are used in the calculation. In Equation 2.6, t_1 is the time after the initial IR drop, t_2 denotes the end of the discharge, and I represent the constant current supplied to the supercapacitor.

2.2 Photo-assist charging energy storage devices

Photo-charging or photo-assisted charging energy storage systems are providing an employment of unlimited solar energy (Li et al., 2015; Liu et al., 2015; Xia et al., 2012). Recent advancements combined energy production and storage into a single device, simplifying the system significantly. The operating concepts are photo-generated e-hole pairs on the surface of light-sensitive battery electrodes, reducing charging potentials and increasing energy efficiency. The photo-charging Li-S, Li-O₂ batteries, Li-ion batteries, aqueous Li/Na-I₂ batteries, and supercapacitors have been

created to lower the charge potential and improve energy efficiency (Figure. 2.6 and 2.7) (Li et al., 2015). These advancements provide a rosy picture for high-efficiency batteries. However, high-efficiency photo transport and adsorption inside an integrated electrode remain significant obstacles to further increasing the energy density and efficiency of the devices.

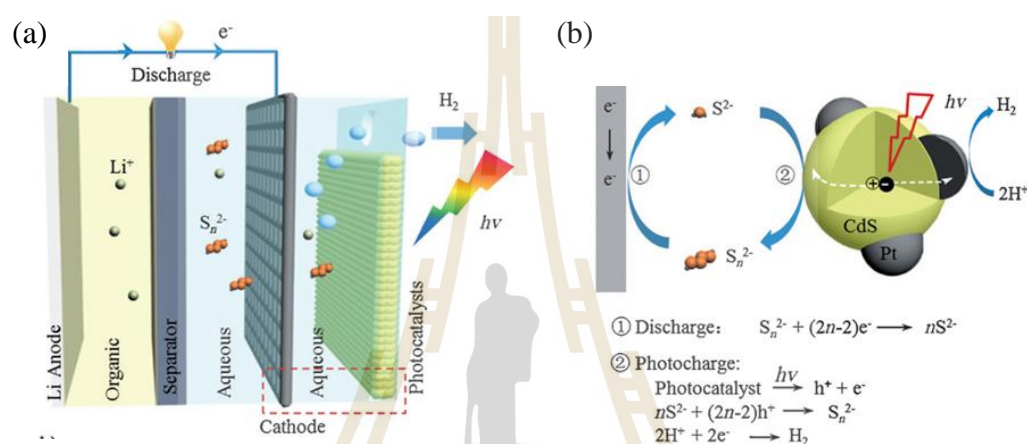


Figure 2.6 The schematic of the photo-charging Li-S battery. (a) The battery is composed of a Li anode immersed in an organic electrolyte. (b) Discharging is identical to that of a standard aqueous Li-S battery (Li et al., 2015).

Due to their photosensitive and pseudocapacitive characteristics, semiconducting materials have become the preferred composite electrodes for photo-assisted charging devices. To fulfill these criteria, the materials should have the following features: 1) a sufficient band gap (1.8-3.0 eV) to absorb more visible light, 2) a cheap cost and high transparency, 3) a high separation efficiency of photogenerated holes-electrons and a long life of the exciting holes (Yang et al., 2019). To the extent feasible, numerous researchers have dedicated their efforts to designing and fabricating composite electrodes with heterogeneous core-shell nanostructures (Mir et al., 2018).

The unique nanoporous and innovative double or multilayer structure, consisting of continuous ligaments and open pores, may offer continuous channels for electron and ion transport, respectively (Qin et al., 2016). Additionally, the nanometer-scale and interfacial effects between the various materials in the composite electrode aided in increasing light absorption and promoting hole-electrons separation.

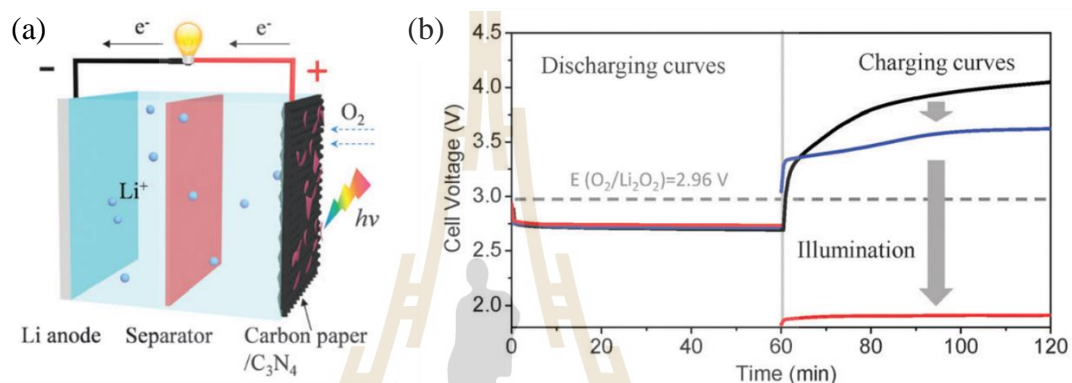


Figure 2.7 (a) The photo-assisted rechargeable Li–O₂ battery comprises a Li anode, a non-aqueous electrolyte containing an I-ion redox mediator, and C₃N₄ grown on carbon paper to serve as an oxygen electrode and a photoelectrode. (b) Charge/discharge curves for a Li–O₂ battery without an I-ion redox mediator (black line), a Li–O₂ battery with an I-ion redox mediator (blue line), and a photo-assisted rechargeable Li–O₂ battery (red line) (Liu et al., 2015).

The photo-assisted charged supercapacitor is shown in Figure 2.8. The charging method of the NPC@Cu₂O hybrid under light illumination consists of two stages (Figure 2.8). Under the influence of light, the semiconductor Cu₂O generates pairs of electrons and holes (Equation [1]), and the holes produced above oxidize the Cu₂O in the NPC@Cu₂O hybrid to CuO. (Equation [2]). Simultaneously, the matching photogenerated electrons are separated from the hole-electron pairs and travel via the

external circuit to the counter Pt electrode, where they react with H_2O to form H_2O . (Equation [3]). The discharge process is the inverse.

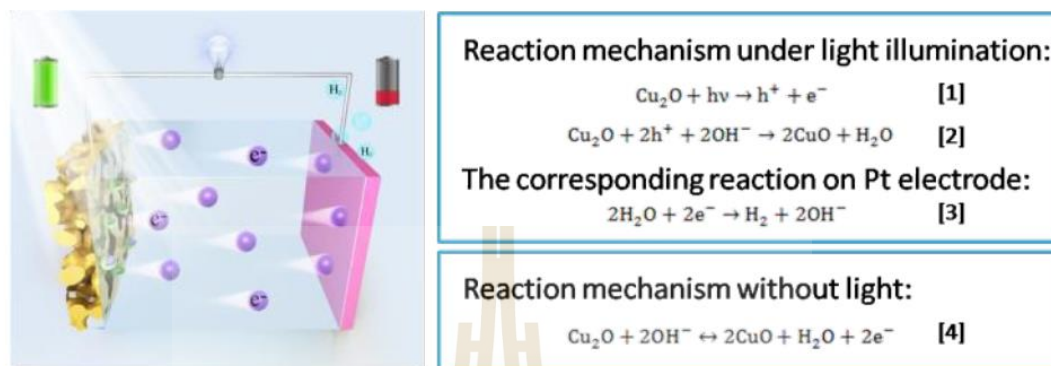


Figure 2.8 The charging process for the electrode reactions in a supercapacitor is shown schematically with/without light illumination.

Additionally, Equation [4], illustrates the reaction process of the NPC@Cu₂O hybrid in the absence of light. Specifically, the active material Cu₂O in the NPC@Cu₂O hybrid interacts with OH⁻ ions in aqueous electrolytes to form CuO during charging, while the opposite reaction occurs when discharging. Above important, following illumination, the photo-generated holes undergo oxidation and react with Cu₂O in the NPC@Cu₂O hybrid, promoting the usage of the electrode materials and increasing the specific capacitance further.

To test the electrochemical performance of the NPC@Cu₂O electrodes with and without light illumination, a specialized three-electrode electrochemical cell was used (100 mW/cm², Xenon lamp). Figure 2.9a shows the CV curves of the NPC@Cu₂O electrodes at a scan rate of 10 mV/s. They each exhibit a pair of redox peaks with a similar form. Under illumination, the peak current rises while the voltage gaps (ΔV) diminish, indicating that the NPC@Cu₂O electrode has an increased specific

capacitance and energy storage capacity. The GCD profiles, as shown in Figure 2.9b, also verified the capacitance increase. As with the CV curves, the charge voltage is lower when the light is on than the light is off. The reverse is true while discharging, indicating reduced over-potentials for both discharging and charging. Following illumination, the specific capacitances increased due to the extended charge/discharge periods at the same current density.

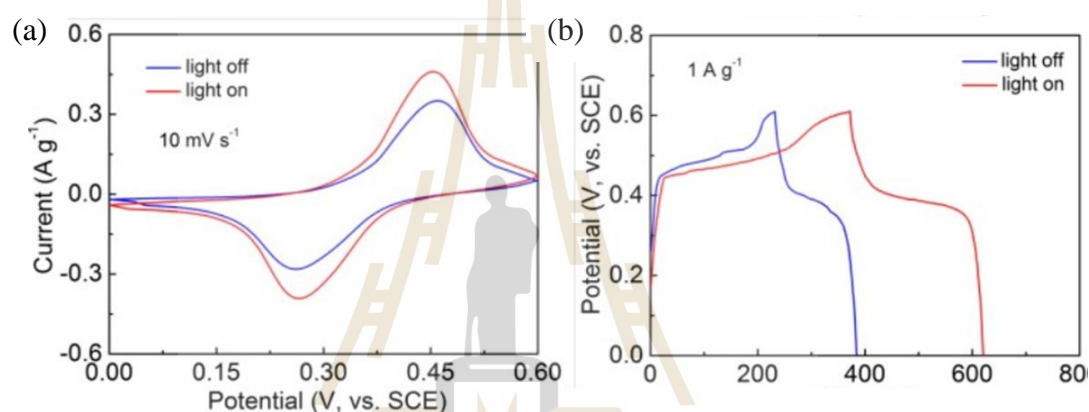


Figure 2.9 (a) Cyclic voltammetry (CV) curves of the NPC@Cu₂O electrode at 10 mV/s under dark and light illumination. (b) Galvanostatic charge-discharge profiles (GCD) at 1 A/g under dark and light illumination (An et al., 2019).

2.3 Decoupled electrochemical water splitting

2.3.1 Conventional and decouple electrolysis

Electrolysis of water to produce H₂ and O₂ is one of the most promising methods for harnessing intermittent renewable energy sources and storing the energy they offer as a clean-burning, sustainable fuel. The electrolysis of water may be thought of as having two half-reactions: the hydrogen evolution reaction (HER) and the oxygen evolution reaction (OER). These half-equations vary somewhat depending on the pH

of the electrolysis solution. The HER and OER proceed in the following manner at low pH: (all potentials are vs the standard hydrogen electrode, SHE)



Whereas, under alkaline conditions, the half-reactions occur as below



As a result, considerable electrical energy is required to operate water electrolysis. A potential difference of 1.23 V is the thermodynamic minimum needed to electrolyze water under normal circumstances. However, more voltage is needed to overcome different kinetic and resistance barriers (and generate significant currents via the OER and HER). This additional voltage is referred to as the overpotential, and it is calculated as the total of the numerous additional potentials associated with concentration, ohmic resistances in the electrolyzer, and the kinetic overpotentials for the individual HER and OER half-reactions (Xiang et al., 2016). The overpotential requirement for the OER often takes precedence over the others since the production of O_2 is a kinetically demanding four-electron, four-proton reaction (Suen et al., 2017). As a result, the OER is often regarded as the primary kinetic bottleneck in the electrolytic production of hydrogen from water.

Water electrolysis occurs simplest when a direct current is passed between two electrodes in a single compartment (Figure 2.10a). This form has many disadvantages, the most serious of which is the inability to separate the resultant gases. As can be shown from Equations 2.7–2.10, two moles of hydrogen are produced for every mole of oxygen generated. These gas-evolving processes occur concurrently, which may

result in the formation of a highly explosive combination. Recent advancements in the development of solid polymer membrane electrolyzers have resulted in incorporating an anion or proton exchange membrane (e.g., Nafion) inside a compressed cell stack. Even if effective and safe gas separation is accomplished, the fact that HER and OER remain linked (as in a typical electrolyzer, see Figure 2.10a) will result in the HER's rate being constrained by the slower OER. Recent advancements in the use of redox mediators to “decouple” these processes have been developed. In essential words, a mediator with a suitable redox potential may be used to link the OER to the mediator's reduction rather than to the direct production of hydrogen. Similarly, the HER may be carried out independently of the OER by connecting hydrogen production to mediator reoxidation rather than water oxidation (Figure 2.10b and 2.10c). Since each half-reaction occurs independently, the HER may be carried out at much higher rates than is feasible with traditional water electrolysis. Additionally, the ability to conduct the HER and OER in distinct locations (“spatial separation”) and at different times (“temporal separation”) substantially improves the flexibility for collecting hydrogen effectively and safely and eliminates the need for any gas purification procedures. The characteristics of a suitable mediator must include stability in both the oxidized and reduced states, as well as a reversible redox couple with a potential between the OER and HER onset potentials. According to the preceding definition, decoupled electrolysis is any process in which the ultimate anodic and cathodic products of electrolysis are generated under at least one of the following conditions: i) at rates that are not intrinsically linked, ii) at different times, or iii) in entirely different electrochemical cells.

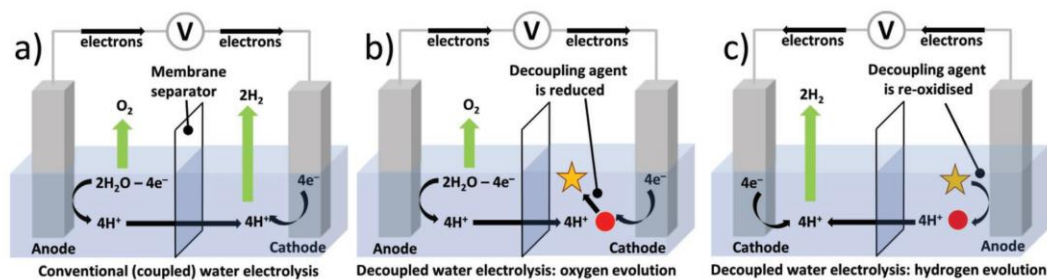
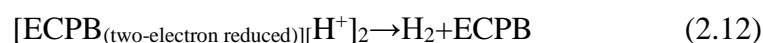


Figure 2.10 Under acidic conditions, a comparison of (a) conventional (coupled) water electrolysis vs (b) Decoupled water electrolysis: OER and (c) decoupled water electrolysis: HER.

2.3.2 Soluble redox mediator

Symes and Cronin pioneered decoupled electrolysis in 2013 using the polyoxometalate phosphomolybdic acid ($\text{H}_3\text{PMo}_{12}\text{O}_{40}$) (Mallouk, 2013; Symes and Cronin, 2013). This polyoxometalate was employed in one compartment of a two-compartment cell, with a semipermeable membrane separating the two sides of the cell (see Figure 2.11). Equations 2.10 and 2.11 were then used to accomplish decoupled water electrolysis. To begin, anodic water oxidation was used to generate O_2 , protons, and electrons. However, rather than combining to form hydrogen at the cathode, the counter electrode reaction was the reduction and protonation of the polyoxometalate (Equation 2.11). This reduced and protonated polyoxometalate may be reoxidized to generate electrons and protons, which could then be used to create hydrogen at the cathode (Equation 2.12).



One of the primary arguments made for decoupled electrolysis is that it may enable more practical device designs for solar-to-hydrogen systems when compared to

the concept of vast, flat arrays producing hydrogen and oxygen on either side of a gas-permeable membrane at a rate limited by the relatively low power provided by solar irradiation. In that research, a tungsten trioxide (WO_3) photoanode was used to conduct water oxidation inside a photoelectrochemical cell using a cathode reaction of phosphomolybdic acid reduction and protonation (Equation 2.11) rather than direct hydrogen generation (see Figure 2.12). Due to phosphomolybdic acid's higher positive redox potential than hydrogen (approximately +0.65 V versus SHE at pH 0.5), the photoanodes using WO_3 should be capable of driving water oxidation at the anode while simultaneously reducing phosphomolybdic acid at the cathode. As a result, no photocurrent was detected without phosphomolybdic acid in a configuration identical to that illustrated in Figure 2.11. However, with no external potential bias, photocurrents greater than 1 mA cm^{-2} were obtained for oxygen production at the WO_3 photoanode (connected to phosphomolybdic acid reduction at the cathode) when illuminated with AM 1.5 light at 1 Sun intensity. These photocatalytic water oxidation current densities compared well to photocurrents produced at low pH (but with applied biases) in previous research employing WO_3 photoanodes. Notably, no hydrogen was produced during this photocatalyzed water oxidation and phosphomolybdic acid reduction process, removing any possibility of a gas crossover. Due to the decreased decoupling agent's resistance to spontaneous reoxidation, the polyoxometalate solution may be trickle-charged at low current densities while oxygen is slowly evolved at the photoanode and allowed to vent to the atmosphere. Once the appropriate level of reduction is achieved, the reduced polyoxometalate solution may be pumped to a separate hydrogen-evolving cell and reoxidized at high current density, releasing hydrogen at the cathode for compression and storage. Hydrogen production at a point-

source electrolyzer located apart from the light collecting array would significantly improve the efficiency and safety of hydrogen gathering. Additional cost savings may be achieved by combining several polyoxometalate-reducing photoarrays with a single polyoxometalate reoxidation cell to optimize the usage of any costly components (e.g., hydrogen evolution electrocatalysts) in this hydrogen generating cell.

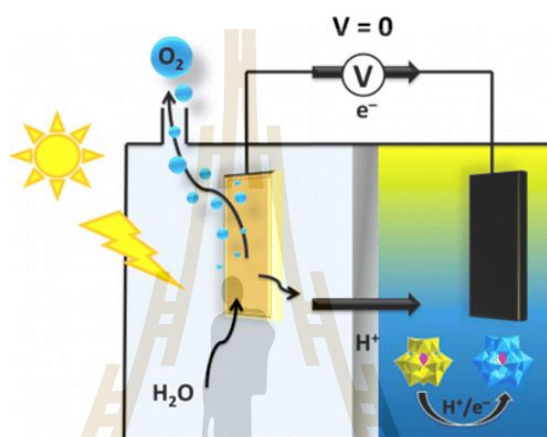


Figure 2.11 A photoelectrochemical cell that created by Bloor et al. (Bloor et al., 2016) for the reduction of phosphomolybdic acid at a carbon cathode that is powered by visible light irradiation of a WO_3 photoanode.

A similar concept, Goodwin and Walsh introduced a novel approach to spatially decouple the OER and HER, which made use of the $\text{Fe}(\text{CN})_6^{3-}/\text{Fe}(\text{CN})_6^{4-}$ redox couple and a closed bipolar electrode (Goodwin and Walsh, 2017). Bipolar electrodes are conducting components capable of promoting both anodic and cathodic reactions concurrently; they are sometimes referred to as "closed" electrodes when their poles are in two distinct solutions. Goodwin and Walsh used two carbon cloths linked by a wire as the closed bipolar electrode in their arrangement, which served as a bridge between two distinct two-compartment cells (Figure 2.12). One end of the closed bipolar electrode was immersed in a solution of $\text{K}_3\text{Fe}(\text{CN})_6/\text{K}_4\text{Fe}(\text{CN})_6$ in 0.1M KOH within

each two-compartment cell. A Nafion membrane partitioned each cell into two compartments, one holding the closed bipolar electrode and the other containing a Pt electrode in 0.1M KOH. The device operated by oxidizing water at a platinum electrode and reducing Fe(CN)_6^{3-} at the closed bipolar electrode in one cell, while oxidizing Fe(CN)_6^{4-} at the other end of the closed bipolar electrode with concurrent hydrogen evolution at the second Pt electrode in the other. Since the HER and OER were conducted in completely separate cells in this configuration, they avoided gas mixing. However, via the closed bipolar electrode, the rates of generation of these gases remained intrinsically connected. Each redox species may be regenerated by regularly changing the current direction, allowing for continuous operation.

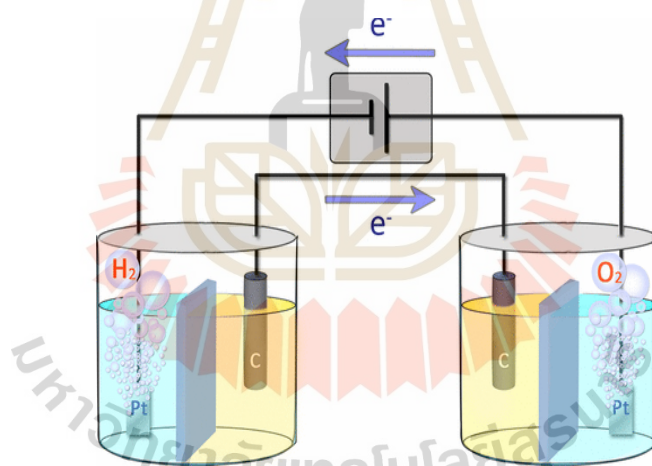


Figure 2.12 Goodwin and Walsh utilized a closed bipolar electrode cell method to spatially isolate O_2 and H_2 generation from water electrolysis (Goodwin and Walsh, 2017).

2.3.3 Solid state redox mediator

Wang and Xia's groups proposed a solid-state decoupled electrolysis system in early 2016, utilizing NiOOH/Ni(OH)_2 as the decoupling agent. The nickel hydroxide

was deposited on carbon nanotubes to form a solid-state mediator/electrode system, which was utilized to decouple the OER and HER of water splitting at high pH, as shown in Figure 2.13. Thus, the HER step involves the oxidation of Ni(OH)₂ to NiOOH (the Ni²⁺ core is oxidized to Ni³⁺). The decoupling agent is subsequently reduced to Ni(OH)₂ in the OER phase, resulting in oxygen generation. The researchers verified via cyclic voltammetry that the NiOOH/Ni(OH)₂ redox pair was located between the onset potentials of the HER and OER. Then, 100 redox cycles were performed, with voltage measurements indicating steady functioning throughout this successive H₂ and O₂ production stages. The purity of the gaseous products produced was determined using in situ differential electrochemical mass spectrometry. No O₂ above the background level was found during the hydrogen evolution phase. Similarly, an examination of the gases produced during the oxygen evolution phase showed that no H₂ was created, indicating that the NiOOH/Ni(OH)₂ electrode had fully decoupled the two water splitting half-reactions. The gaseous products were measured, and the HER and OER had more than 90% Faradaic efficiencies. In addition to Wang and Xia, the Grader and Rothschild groups reported using the identical NiOOH/Ni(OH)₂ mediator in a closed bipolar electrode-type system for decoupled water electrolysis under alkaline conditions (Landman et al., 2017; Landman et al., 2020). In two spatially separated, two-compartment cells with 1M NaOH electrolytes, simultaneous hydrogen and oxygen production were accomplished. Both cells used a NiOOH/Ni(OH)₂ electrode connected through copper wire and a Ni foil electrode to produce the gaseous products. The system was capable of constantly producing both H₂ and O₂ over 20 hours at a current density of 5 mA/cm². Once the cell voltage reached a certain value (showing that the nickel hydroxide electrodes had been completely charged/discharged), the

current polarity was switched, causing the reactions in each cell to proceed in the other direction. The overall charge/discharge time for each cycle decreased by an average of 0.3 percent each cycle during the 20 hours; this was ascribed to insufficient charging of the NiOOH/Ni(OH)₂ electrode in the HER cell. Following that, the researchers ran lengthier cycles (>6 hours) with the electrodes charged to 448 mAh (34% of their rated capacity) for a total of 125 hours. Analyses of the generated gases showed that H₂ and O₂ were created with a Faradaic efficiency of 100 percent. The NiOOH/Ni(OH)₂ closed bipolar electrode cell arrangement was combined with a Si photovoltaic module to create a solar-powered water splitting system with a 7.5 percent solar-to-hydrogen conversion efficiency. This result was similar to those achieved at the time of writing using state-of-the-art solar-powered water splitting devices (Jia et al., 2016; Luo et al., 2014) (May et al., 2015).

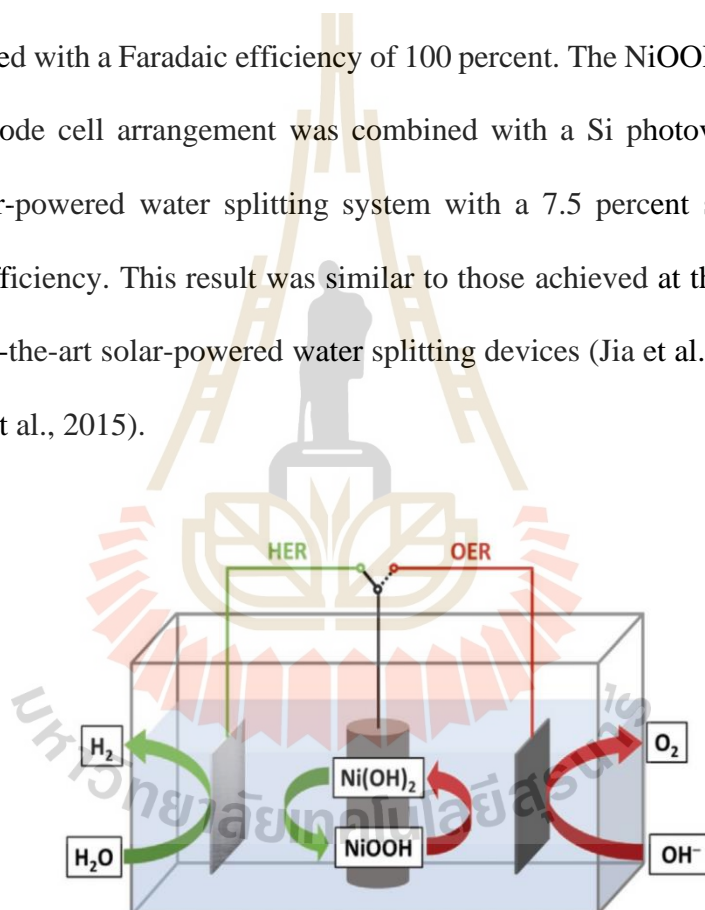


Figure 2.13 The mechanism of NiOOH/Ni(OH)₂ as a solid decoupling agent electrode is shown schematically. The OER is linked to the reduction of NiOOH (red arrows), whereas the HER is coupled to the oxidation of Ni(OH)₂ (green arrows) (McHugh et al., 2020).

2.4 Oxygen vacancies in transition-metal oxides and photoelectrochemical/ photocatalyst

2.4.1 Photo-induced oxygen vacancy in transition-metal oxides

The carrier densities on metal oxide surfaces can be controlled by the creation of oxygen vacancy states induced by light irradiation, such as two-dimensional electron gas (2DEG) in SrTiO₃ (Meevasana et al., 2011b), and capacitance enhancement in Bi_{0.95}La_{0.05}FeO₃ (BLFO) (Nathabumroong et al., 2020) as shown Figures 2.14 and 2.15. Figure 2.16 shows valence band spectra of SrTiO₃ and Bi_{0.95}La_{0.05}FeO₃, respectively, for different exposures to UV light the spectrum shows clear oxygen 2p (O2p) states between ~ 3 –9 eV, and no significant spectral weight in the band gap (0–4 eV). As the exposure time increases, the spectral weight of the O2p state decreases slightly and its leading edge shifts to higher binding energy. This indicates an increase in the valence band maximum to surface Fermi level separation, consistent with a downward band bending and development of a 2DEG at the surface (Figure 2.16a). Together with the valence band shift we also observe a broad in-gap state developing. This state is most likely associated with oxygen vacancies at the surface.

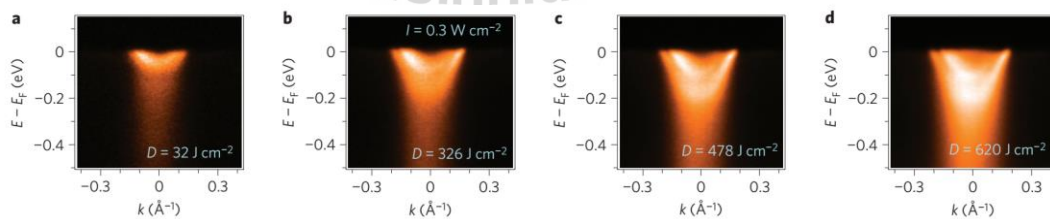


Figure 2.14 Variation in the charge density of 2DEG in response to different UV irradiation doses. The APES results in (a)-(d) correspond to the given irradiation doses in SrTiO₃.

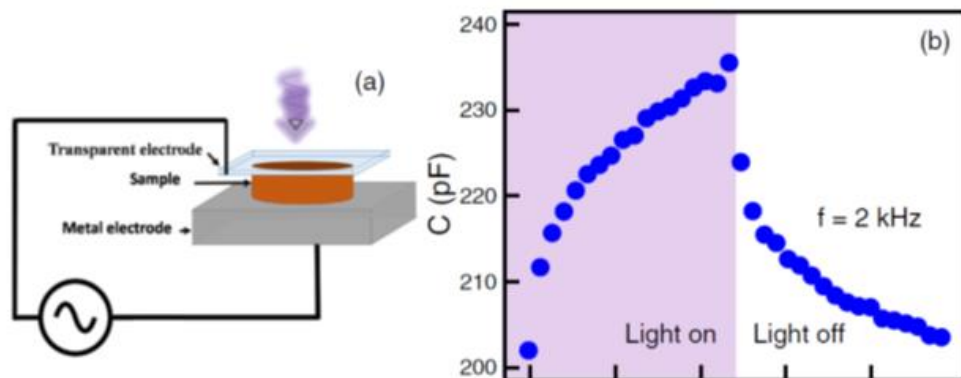


Figure 2.15 (a) Schematic of capacitance measurement allowing for light irradiation of the top electrode. (b) Capacitance of the BLFO as a function of UV laser irradiation at $f = 2$ kHz with a time scale of 480 s.

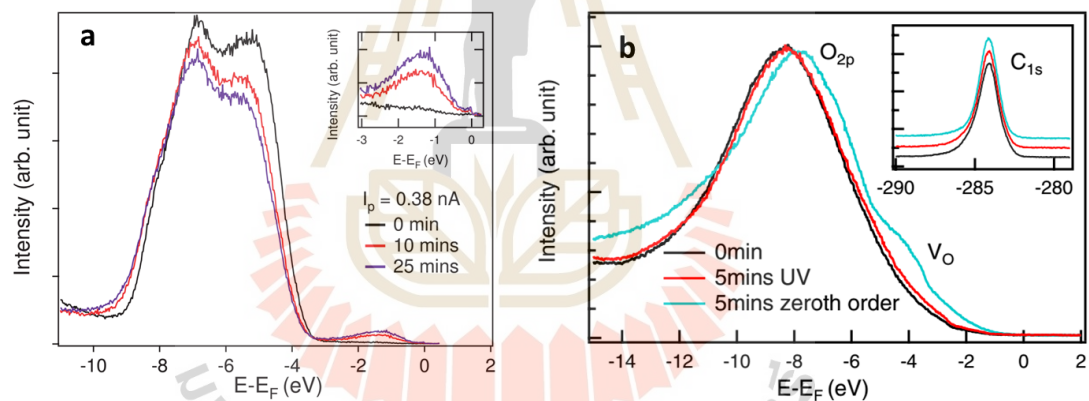


Figure 2.16 (a) and (b) Evolution of the valence band (VB) spectra of SrTiO_3 and $\text{Bi}_{0.95}\text{La}_{0.05}\text{FeO}_3$, respectively, from the pristine cleaved surface to the exposed surface. The inset (a) shows the evolution of the in-gap state with increasing exposure to UV light. And inset (b) shows clearly indicates no binding energy shift of C_{1s} state which is confirming the character of BLFO (Meevasana et al., 2011b; Nathabumroong et al., 2020).

2.4.2 Role of surface oxygen vacancy in photoelectrochemical

Oxygen vacancies in semiconductors significantly reduce electron-hole recombination, which has significant implications for photocatalysis and photoelectrochemical applications. It resulted in a substantial increase in the lifetimes of photogenerated charge carriers after visible light stimulation (Lv et al., 2016). The photocurrent-time (It) curves shown in Figure 2.17a are used to determine the photocatalysts charge carrier separation capabilities. Increased photocurrent implies improved electron-hole separation, with AgBiVO_4OV exhibiting excellent photoelectric conversion under simulated solar irradiation. The degradation process of AgBiVO_4OV is shown in Figure 2.17b. The photocatalytic process started by direct excitation usually involves the following: (1) electrons (e^-) in the VB are excited to the CB, resulting in the production of an equal number of h^+ ; (2) photogenerated e^- and h^+ diffuse to the bulk and surface, respectively; (3) surface oxidation mediated by h^+ and/or derivative active species.

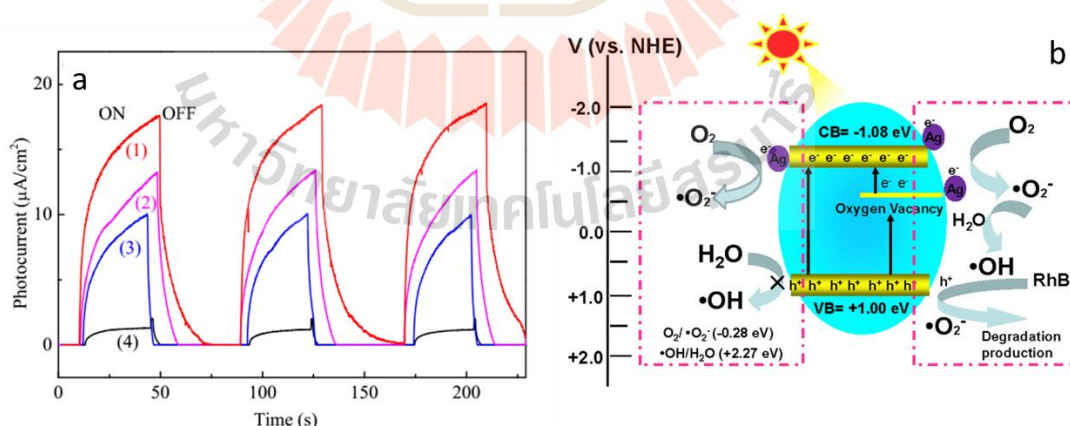


Figure 2.17 (a) Photocurrents curves for (1) $\text{Ag-BiVO}_4\text{-OV}$, (2) $\text{BiVO}_4\text{-OV}$, (3) Ag-BiVO_4 , and (4) BiVO_4 electrodes, under visible light ($\lambda > 420 \text{ nm}$). (b) The schematic diagram shows the mechanism of charge separation and the photocatalytic reaction of $\text{Ag-BiVO}_4\text{-OV}$, under simulated solar light irradiation (Shi et al., 2018).

2.5 Application of CuO and Cu₂O on photoelectrochemical water splitting

Cu₂O and CuO are the most typical *p*-type binary oxides developed for solar water splitting applications. Apart from their advantageous bandgap energies, which enable the use of visible light (Figure 2.18), the low cost, abundance on the earth, and nontoxicity of Cu all contribute to the development of Cu-based photoelectrodes. Cu₂O, with a direct bandgap of 2.0 eV, is an appealing oxide for solar water reduction, allowing for potentially 14.7 mA/cm² photocurrent and an 18% solar to hydrogen conversion efficiency.

The major limitation of Cu₂O is photocorrosion during photoexcitation. Upon illumination, the transform Cu₂O into Cu or CuO by photoexcited electron and hole consumptions, are shown in Equation 2.12 and 2.13.

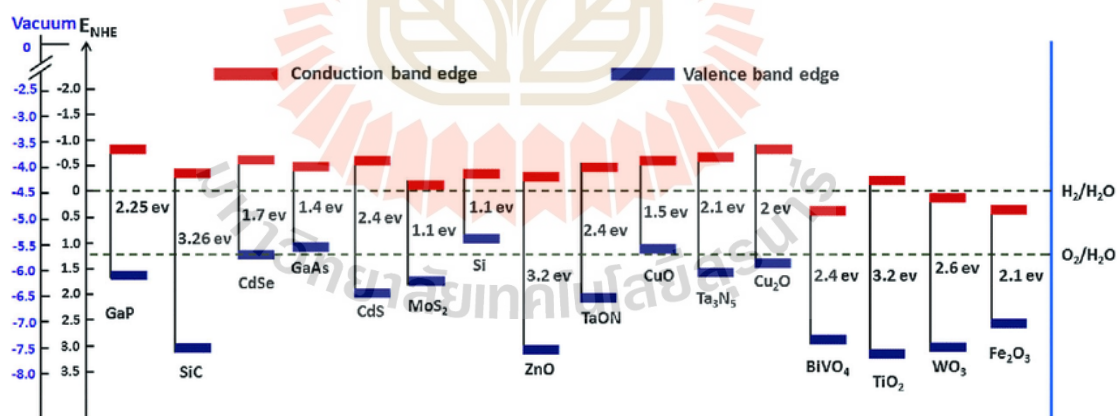
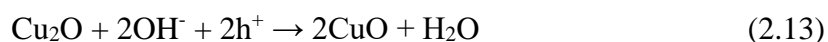


Figure 2.18 Band edge positions of semiconductors in contact with an aqueous electrolyte at pH = 0 compared to NHE and vacuum. Additionally, the redox potentials of HER and OER are given for comparison.

Electron-mediated photocorrosion:



Hole-mediated photocorrosion:



Yang et al. showed the synthesis of a $\text{Cu}_2\text{O}/\text{CuO}$ bilayer hybrid by electrodeposition and subsequent thermal oxidation (Yang et al., 2016c). Combining electrodeposition and thermal oxidation enables the production of $\text{Cu}_2\text{O}/\text{CuO}$ heterogeneous photocathodes for HER in a simple, low-cost, and scalable manner. $\text{Cu}_2\text{O}/\text{CuO}$ photocathode showed a substantial increase in photoactivity and excellent photostability toward HER, particularly at high potentials in alkaline solution. The photocurrent density of HER was $3.15 \text{ mA}/\text{cm}^2$ at 0.40 V vs. RHE, which was one of the highest values recorded for the same potential on copper-oxide-based photocathodes. During the four-hour tests, excellent photostability was observed (Figure 2.19 and 2.20).

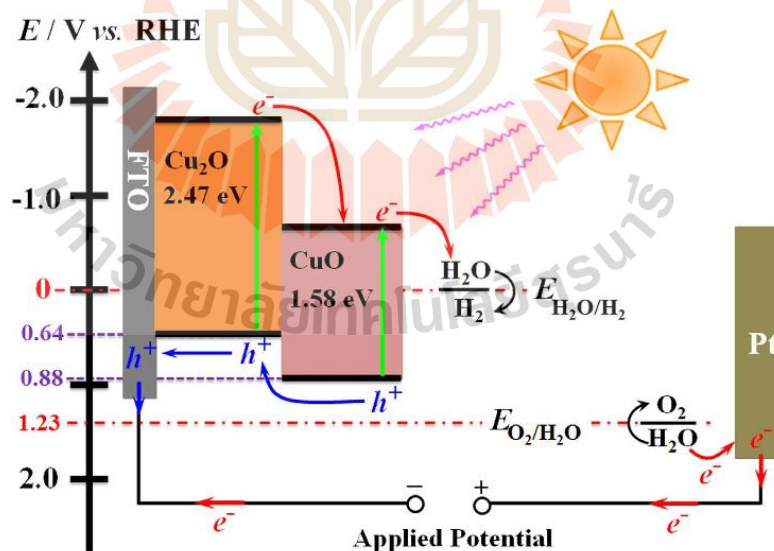


Figure 2.19 The schematic show energy band structure of the $\text{Cu}_2\text{O}/\text{CuO}$ bilayered composite in contact with solution during PEC HER.

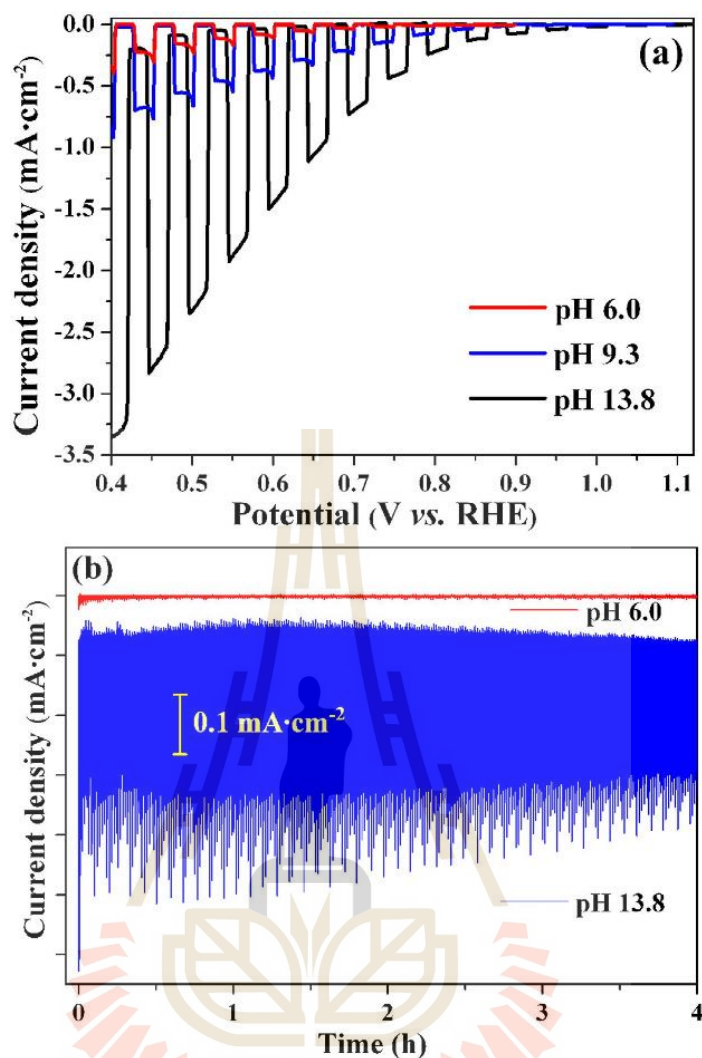


Figure 2.20 The activity (a) and stability (b) of the Cu₂O/CuO bilayered composites at different pH levels in 0.5M Na₂SO₄ solution. Cu₂O/CuO composites were produced by deposition with r-DPPC for 2.5 minutes followed by thermal oxidation at 400°C for 2 hours. In addition, stability tests were conducted at a significantly high HER potential of 0.76 V compared to RHE.

CHAPTER III

RESEARCH METHODOLOGY

Chapter III describes the experimental methods of the research, which can be generally categorized into the following five main sections:

- (i) Synthesis of CuO-Cu(OH)_2 via the surface oxidation of copper in alkaline solution and characterization of the electrode by SEM and XRD techniques.
- (ii) Electrochemical characterization and electrode activation
- (iii) Fabrication of two-cell water electrolysis system
- (iv) Performance of a two-cell water electrolysis system and photo-enhanced pure gas production
- (v) *In-situ* X-ray absorption spectroscopy (XAS) and Photoemission spectroscopy (PES)

This chapter will give a brief introduction to these techniques and facilities, and the background theories of these methods will also start one by one.

3.1 Synthesis and characterization of CuO-Cu(OH)_2 electrode

3.1.1 Preparation of CuO-Cu(OH)_2 on copper foil

The Cu(OH)_2 nanowire/microflower-like CuO films on Cu foil were synthesized by chemical oxidation. A Cu foil (9 μm , 99%, MTI USA) was cut into $2.5 \times 5 \text{ cm}^2$ sheets and cleaned by ultrasonication in acetone, ethanol, and distilled water, sequentially. Impurities and oxide layers were removed from the surface by immersing

in a 1M HCl solution for 30 mins. The cleaned Cu foil was then immersed in an aqueous solution consisting of 24 mL 10M NaOH, 12 mL 1M $(\text{NH}_4)_2\text{S}_2\text{O}_8$, and 54 mL distilled water (Wang et al., 2015; Xu et al.) at room temperature (25°C). After 15 mins, a dark-blue film covered the Cu foil surface, indicating the formation of $\text{Cu}(\text{OH})_2$. The $\text{Cu}(\text{OH})_2$ coated Cu foil was then taken from the solution, rinsed with water, then ethanol, and dried in air.

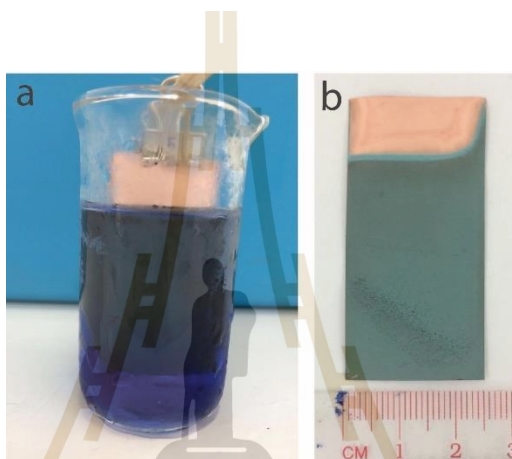


Figure 3.1 $\text{Cu}(\text{OH})_2\text{-CuO}$ electrode preparation (a) surface oxidation of Cu in alkaline solution (b) As-prepared $\text{Cu}(\text{OH})_2\text{-CuO}$ electrode.

3.1.2 Electrode characterization

The morphology and chemical composition of the $\text{Cu}(\text{OH})_2$ nanowire/microflower-like CuO was examined by scanning electron microscopy and Energy-Dispersed Analysis of X-rays (SEM-EDAX, ZEISS Auriga, operated at 5 keV). The crystal structures of the samples were analyzed using an X-ray diffractometer (XRD, Bruker D2 Advance diffractometer) with Cu-K α radiation ($\lambda = 0.1506 \text{ nm}$) with a scan rate of $10^\circ \text{ min}^{-1}$ at a step width of 0.02° .

3.1.2.1 Field emission scanning electron microscopy (FESEM)

SEMs are that generate pictures of material by scanning the surface with a focused beam of electrons. The electrons interact with atoms in the sample, producing various signals that contain information on the surface topography and composition of the sample. The most signals employed imaging are low secondary electrons (SE) with energies less than 50 eV, high energy backscattered electrons (BSE) with energies more than 50 eV, and distinctive X-rays (Figure 3.2) (Henning and Adhikari, 2017; Inkson, 2016). As the secondary electrons are lower in energy than the backscattered electrons, they can be separated from the high energy backscattered electrons with an electric field. Because of the secondary electrons' low energy, they only escape from the topmost layers of the sample and hence carry information from these layers. A secondary electron image thus gives information about the topography of the sample. The higher energy backscattered electrons can escape from more rooted in the sample. The number of backscattered electrons depends on the atomic number of the sample. Hence a backscatter electron image gives information about the composition of the sample. Additionally, Characteristic X-rays are emitted when the electron beam removes an inner shell electron from the sample, causing a higher-energy electron to fill the shell and release energy. The energy or wavelength of these characteristic X-rays can be measured by Energy-dispersive X-ray spectroscopy or Wavelength-dispersive X-ray spectroscopy. It is used to identify and measure the abundance of elements in the sample and map their distribution (Figure 3.3) (Henning and Adhikari, 2017; Inkson, 2016).

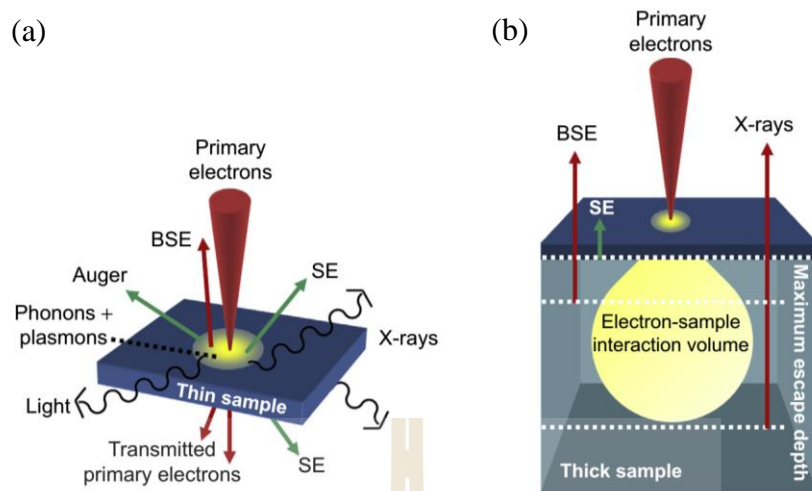


Figure 3.2 The interaction of electron beam on the sample (a) the signal produced by the electron interaction in the thin sample; (b) the absorption of secondary electrons, backscattered electrons, and X-rays in the thick sample, by inelastic scattering within the interaction volume will limit the depth of specimens (Inkson, 2016).

3.1.2.2 X-ray diffractometer

X-ray diffractometry (XRD) is the widely used method for determining the crystal structure of solids, such as the lattice constant (a), the crystallite size (D), and the atomic spacing (d). In a typical XRD measurement of crystalline materials, incident X-rays impinge on the film and are diffracted into a range of angles. These diffracted X-rays (forming Bragg peaks) are then collected. According to Bragg's Law, constructive interference occurs when the path difference between the incident and diffracted beams is an integer multiple n of the X-ray source wavelength λ

$$2d \sin \theta = n\lambda \quad (3.1)$$

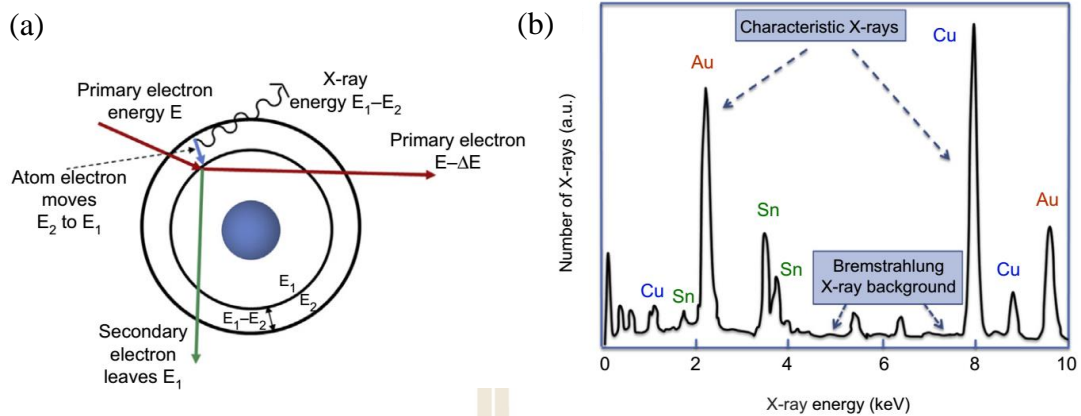


Figure 3.3 X-ray emission caused by electrons (a) Characteristics of X-ray formation. X-rays are generated when electrons move to fill the vacant electron energy level vacated by secondary electrons. (b) A schematic of an energy-dispersive X-ray (EDX) spectra showing many characteristic X-rays at specific energy (Inkson, 2016).

as illustrated in Figure 3.4. Based on this law, a spectrum of diffraction intensity versus the angle between the incident and diffraction beams can be obtained by continuously changing the angle between the incident X-ray beam and the sample. However, for the characterization of thin films, the incident X-ray beam angle is kept constant at a shallow level while a detector moves along an arc to capture the diffracted rays. The resulting intensity peaks occur at angles corresponding to the constructive interference of the beams diffracted by the first few atomic planes of the sample. The locations (angles) of these peaks reveal the underlying crystal structure. The crystal quality, on the other hand, can be inferred from the full-width half-maximum (FWHM) of the peaks, where the peak width is inversely related to the crystal grain size. For polycrystalline materials, the average grain size D can be estimated from the FWHMs of the diffraction peaks using Scherrer's formula

$$D = \frac{\beta\lambda}{FWHM \cdot \cos\theta} \quad (3.2)$$

where λ is the wavelength of the X-ray, θ is Bragg's angle in radians and β is a correction factor close to unity (Ingham and Toney, 2014).

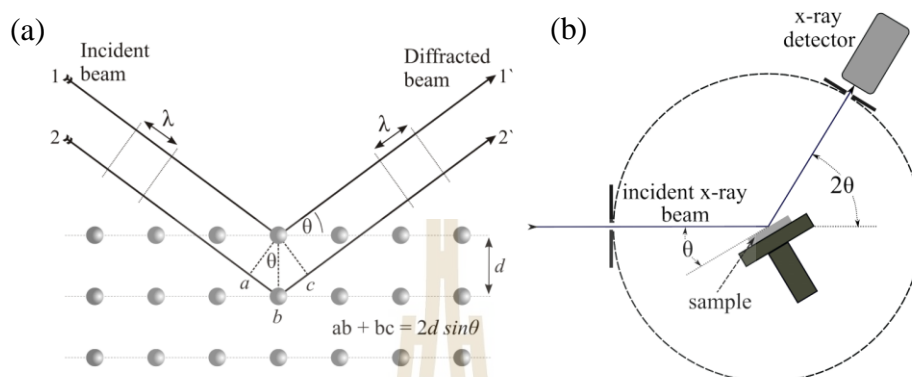


Figure 3.4 (a) Bragg's diffraction law. Two identical wavelengths and phased beams are dispersed off of two distinct atomic planes. The lower beam travels an additional $2d\sin\theta$ length. When its length is an integer multiple of the wavelength, constructive interference occurs. (b) Schematic setup of the XRD measurement system (Elzwawi, 2015).

3.2 Electrochemical characterization and electrode activation

3.2.1 Electrochemical characterization under dark and solar irradiation

The electrochemical measurements were carried out on a potentiostat/galvanostat. The $\text{Cu}(\text{OH})_2$ nanowire/microflower-like CuO redox electrode was used as the working electrode (WE) in an electrochemical cell operated in a conventional three-electrode system with a Pt counter electrode (CE) and an Ag/AgCl reference electrode (RE) in an aqueous electrolyte solution of 1M NaOH in deionized water. Cyclic voltammetry (CV) and galvanostatic charge-discharge (GCD) measurements of half-cell electrodes (size $1 \times 1 \text{ cm}^2$) were performed under dark, laser

light (450 nm), and solar irradiation. The light source applied for the illumination is simulated sunlight from a PET solar simulator (model SS100AAA)

3.2.2 Electrode activation

The activation process of $\text{Cu}(\text{OH})_2\text{-CuO}$ electrode was carried out using a three-electrode system setup, as presented in the 3.2.2 section and Figure 3.5. During the activation process, the working electrode was charged and discharged in the potential window of -1.3 V to 0.55 V vs. Ag/AgCl at 4 mA/cm² and 0 V to 0.6 V vs. Ag/AgCl at 10 mA/cm² until its discharge capacity stabilized. The discharge capacity of the electrode can be calculated from the discharge curves using the following equation:

$$C_m = \frac{I_d \cdot \Delta t}{m \Delta V} \quad (3.3)$$

Where C_m (F/g) is the specific capacitance, I_d (mA) is the discharge current, Δt (s) is the discharge time, ΔV (V) is the discharge potential rang, and m (mg) is the mass of active material. At the end of the activation process, one of the redox electrodes (size 2.5x4 cm²) was charged and converted to $\text{CuO-Cu}(\text{OH})_2$ by constant current charging (4 mA/cm², 1.5h), whereas the other one (size 2.5x4 cm²) was discharged and converted to Cu_2O by constant current discharging (-4 mA/cm², 1.5h).

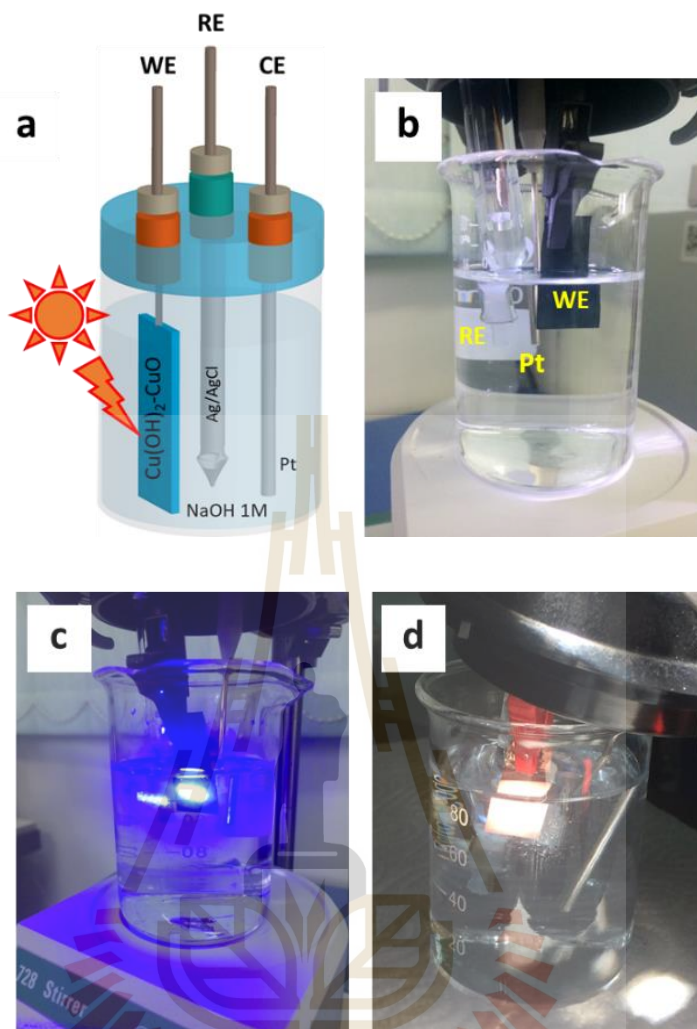


Figure 3.5 Three-electrode electrochemical cell setup. (a) Schematic of three-electrode system. Electrochemical measurement under (b) dark, (c) laser light (450 nm) and (d) solar irradiation.

3.3 Two-cell water electrolysis system

3.3.1 Considerations for selecting the redox mediator electrodes

The conditions for decouple water must be considered. 1) The redox reactions of the mediator electrodes that mediate the OH^- ion exchange with the primary electrodes must be reversible and stable in alkaline electrolyte. This is the key to the

continuous operation of two-cell water splitting. 2) These reactions must be carried at potentials between the hydrogen and oxygen evolution reaction (HER and OER) potentials of the electrodes. Otherwise O_2 may evolve at the mediator electrode in the hydrogen cell and vice versa. 3) Mediator electrodes need to have required both photo-sensitive and pseudocapacitive properties because they are important for improving H_2 and O_2 gas production. Finally, the mediator electrodes must be abundant, low cost, benign and non-toxic materials, and their density should not change much during extended operation with multiple cycles. If this is not the case, the mediator electrodes will disintegrate over time due to swelling and will not sustain many cycles of charging and discharging.

All these prerequisites are met by the $CuO-Cu(OH)_2/Cu_2O$ redox couple, which is widely used in rechargeable batteries, pseudocapacitors (Senthilkumar et al., 2015; Xu et al., 2019; Xu et al., 2016; Xu et al., 2015) and photoelectrochemical system (John and Roy, 2019; Wu et al., 2010; Yang et al., 2016a). Therefore, the redox-reversible $CuO-Cu(OH)_2/Cu_2O$ electrodes are used as mediator electrodes in our two-cell water electrolysis system.

3.3.2 Fabrication of two-cell water electrolysis system

A two-cell water electrolysis system (shown in Figure 3.6) was constructed with Ni foam primary electrodes ($2.5 \times 4 \text{ cm}^2$) and $CuO-Cu(OH)_2/Cu_2O$ ($2.5 \times 4 \text{ cm}^2$) redox electrodes that had been activated beforehand as described above. The primary Ni electrodes (anode and cathode) were dipped in two glass bottles filled with alkaline aqueous solution (1M NaOH in deionized water) and connected to a potentiostat/galvanostat. Two-electrode experiments were performed by attaching the

counter and reference electrodes together, thereby giving a floating reference configuration. The redox electrodes were placed in the respective bottles near the

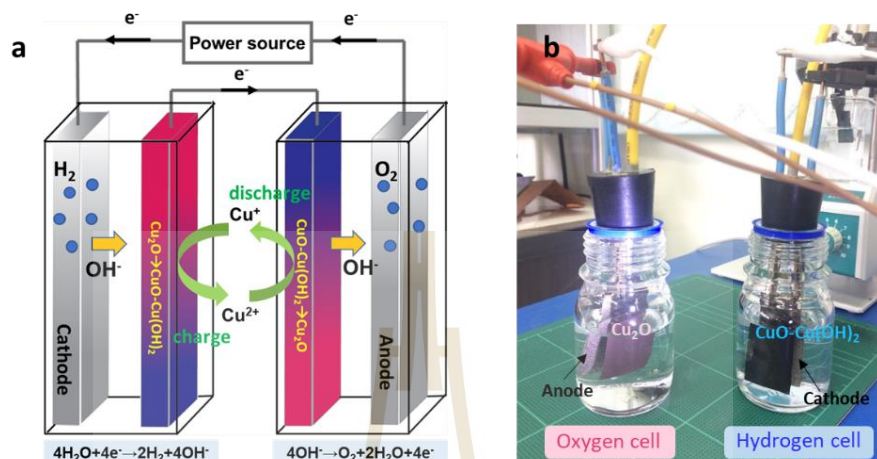


Figure 3.6 The membrane-free configuration for alkaline water electrolysis in separate oxygen and hydrogen cell. (a) Schematic illustration and (b) experimental setup of a two-cell water electrolysis system after operated 20 minutes, respectively.

primary electrodes (~1.5 cm). The CuO-Cu(OH)₂ electrode was placed close to the Ni anode in the oxygen cell. And finally, the Cu₂O electrode was placed close to the Ni cathode in the hydrogen cell. The duration time of electrolysis cycles was 1.5 h with an applied constant voltage of 2.0-3 V. The threshold limit was set at 3 V in order to avoid gas generation at the redox mediator electrodes.

3.4 Performance of two-cell water electrolysis system and photo-enhanced pure gas production

In order to measure gas volume and the Faradaic efficiency of the total water electrolysis process at a constant applied voltage of 3 V in the two-electrode system,

the volume of H₂ and O₂ production were measured using a custom-built device (shown in Figure 3.7). The mixing of gases during water electrolysis was monitored by an in-situ gas chromatography technique. Before all gas analysis, the electrolyte and seal cells were purged with pure Ar (99%) or N₂ (99%) and pumped down to vacuum in several pump-purge cycles.

3.4.1 Gas measurement and Faradaic efficiency.

Before electrolysis operation, the NaOH 1M was purged with Ar (or N₂) gas for 30 mins. The air and Ar gas were extracted in a two-cell water electrolysis system before H₂ and O₂ measurement in several pump-purge cycles. The effluent gas from the hermetically sealed cells was measured at several time points during the electrolysis test using a custom-built device for gas volume measurement, as shown in Figure 3.8. The generated gas can be collected on U-tube. The volume of generated gas can be read from the shift of liquid level during the measurement.

The Faradaic efficiency (η_F) can be calculated from the volume of gases from hydrogen and oxygen cells, which was compared with the charge transferred between the Ni foam electrodes during that time, $Q = \int Idt$. The η_F for the O₂ and H₂ generation was calculated from the following equation (Landman et al., 2017):

$$\eta_F = \frac{n(\text{gas})_{\text{measured}}}{n(\text{gas})_{\text{calculated}}} = \frac{PV(\text{gas})_{\text{measured}}/RT}{Q/zF} \quad (3.4)$$

wherein P is the pressure (1 atm), V is the volume of the effluent gas, R is the gas constant, T is the temperature (298 K), $Q = \int Idt$ the charges, z is the stoichiometric charge number (2e⁻ per H₂ molecule and 4e⁻ per O₂ molecule) and F is the Faraday constant.

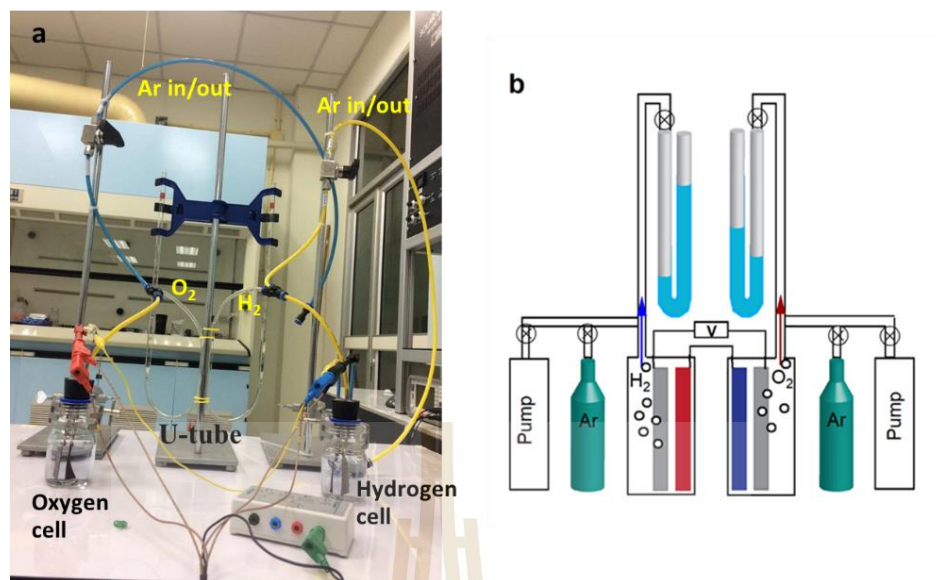


Figure 3.7 (a) and (b) Measurement setup and schematic illustration of a typical custom-built devices for measured volume of gases, respectively.

3.4.2 *In-situ* Gas chromatography

The *in-situ* GC measurement was performed with the applied constant voltage of 3 V to investigate the gas production and the mixing of gas in a two-cell water electrolysis system (Figure 3.8). The purity of H₂ and O₂ were obtained from the experiment at room temperature.



Figure 3.8 Photograph of *in-situ* GC measurement system.

For the photo-enhanced gas production measurement, the redox mediator electrode was exposed to simulated sunlight from Solar simulator class AAA with an AM 1.5G filter (LOT-QD). The light was reflected from a mirror and projected onto the sample (illumination area 20 cm²) with an intensity of 80 mW/cm². The photoresponse of mediator electrodes during water electrolysis was performed under on-off light irradiation.

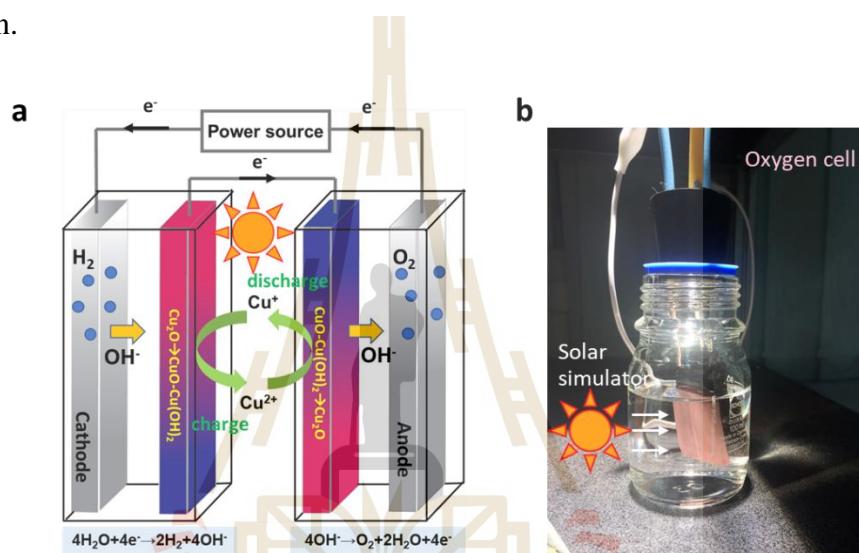


Figure 3.9 Schematic illustration and Experimental setup of a two-cell water electrolysis system, respectively.

3.5 *In-situ* X-ray absorption spectroscopy (XAS)

X-ray absorption spectroscopy (XAS) is an effective method since it provides information on crystalline and amorphous materials and may be used in reaction settings. The theory of X-ray absorption spectroscopy is briefly demonstrated in Figure 3.10, both in terms of XANES (X-ray absorption near-edge structure) and EXAFS (extended X-ray absorption fine structure) spectroscopy. When the input X-ray energy is at or above the desired element's absorption edge, core electrons are excited to

unoccupied states. As a result, the incident X-ray is strongly absorbed, resulting in a considerable shift in the spectrum, referred to as the X-ray absorption near edge structure (XANES). Because the energy of core electrons is modified by the electron distribution in the valence state, XANES is sensitive to electronic transitions, site symmetry, and changes in the oxidation state of the investigated element (Bressler and Chergui, 2004; Koningsberger, 1988). When the energy of the X-rays is increased further, the core electrons are excited to the continuum state. The interferences between outgoing and scattering waves with nearby atoms in the extended X-ray absorption fine structure (EXAFS) generate the oscillation, which represents an element's local environment in terms of coordination number, bond length, and chemical species of the closest atoms. (Giorgetti, 2013). This oscillatory fine structure may be retrieved using the EXAFS-function $\chi(k)$. Assuming that the photo-electron scatters just once throughout its lifetime, theory indicates that the EXAFS function may be estimated using the so-called single scattering approach (Equation 3.5)(Grunwaldt and Baiker, 2005):

$$\chi(k) = \sum_j N_j S_0^2 F_j(k) e^{-2\sigma_j^2 k^2} e^{-2r_j/\lambda_j(k)} \frac{\sin(2kr_j + \phi_{ij}(k))}{kr_j^2} \quad (3.5)$$

where r_j is the distance between the absorber atom i and the neighbouring atoms in the j^{th} shell, N_j the number of neighbouring atoms in the j^{th} shell, $F_j(k)$ the backscattering amplitude, $\phi_{ij}(k)$ the phase shift experienced by the photoelectron in the scattering process. S_0^2 is the amplitude reduction factor and leads to a certain damping of the signal. Additional damping factors are the exponential terms with the Debye–Waller factor σ^2 and with the mean free pathlength λ ; the latter being only a

few Å which makes EXAFS ideal as a local probing technique (in the XANES region the mean free pathlength is much longer, leading to multiple scattering effects).

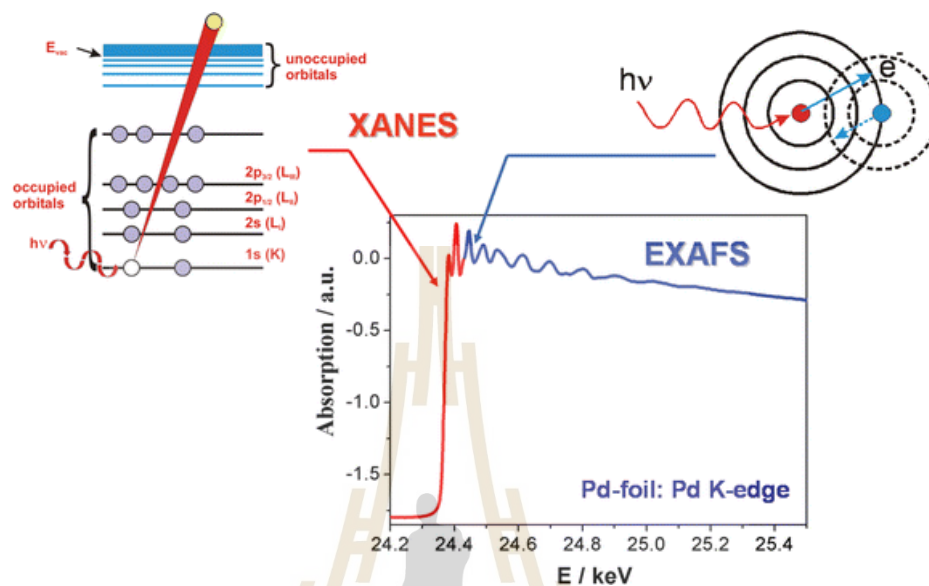


Figure 3.10 The X-ray absorption near edge structure (XANES) and extended X-ray absorption fine structure (EXAFS) spectroscopies (Grunwaldt and Baiker, 2005).

In summary, XANES provides a "fingerprint" of the structure surrounding the absorber atom, such as its oxidation state and symmetry. In contrast, the EXAFS region can reveal the kinds and structure (distances and coordination numbers) of nearest-neighbor atoms by applying appropriate fitting routines using the EXAFS formula above. Furthermore, due to the oscillating nature of the EXAFS function, Fourier transformations of the EXAFS data ($\chi(k)$ -function) are often an advantage, yielding a radial distribution function.

Three XAS modes are available for specimen testing (Figure 3.11b and 3.11c). After the X-ray interacts with the specimen, the transmission mode detects the difference between the incident and transmits X-ray (I_0 and I , respectively). In addition, the X-ray absorption coefficient ($\mu(E)$) may be used to quantify the attenuation

of X-ray intensity (Koningsberger, 1988), according to Beer's law as equation (3.6) (Beer, 1852). In terms of data quality, the sample should be concentrated and homogeneous (Beer, 1852). The fluorescence mode collects the X-rays generated from an element. This mode is ideal for dilute specimens since the emission intensity is affected by self-absorption apart from the element's absorption. The $\mu(E)$ is determined using Equation 3.7. Finally, the electron yield mode quantifies the photoelectrons emitted. In contrast to the bulk-sensitive modes discussed above, the electron yield mode is surface-sensitive owing to the photoelectrons' straightforward mean free path ($\sim 10 \text{ \AA}$).

$$\mu(E)x = -\ln\left(\frac{I}{I_0}\right) \quad (3.6)$$

$$\mu(E) = C\left(\frac{F}{I_0}\right) \quad (3.7)$$

where x is the thickness of the sample, F is the intensity of the fluorescence X-rays, and C is approximately constant.

The majority of electrocatalytic processes include chemical absorption and electron transfers, which result in a change in the oxidation state and local structure, which is the short-range bonding structure, within 5 \AA , respectively (Wang et al., 2019; Wu et al., 2017). These changes are reversible and difficult to identify using ex-situ characterizations. However, XAS, especially *in-situ*, can probe oxidation state and local structure under real-reaction circumstances. By using this technique, the Cu K-edge X-ray absorption experiments were conducted in fluorescent mode at BL5.2 of the Synchrotron Light Research Institute (SLRI), Thailand. The electron energy was 1.2 GeV, beam current 80-150 mA, and maximum photon flux was about $1.1\text{-}1.7 \times 10^{11} \text{ photons}\cdot\text{s}^{-1}$. The X-ray beam size was $25 \text{ mm}(\text{width}) \times 1 \text{ mm}(\text{height})$. The normalized

XAS spectra were processed and analyzed using Athena software. For in situ XANES and EXAFS measurements, all spectra were collected during water electrolysis at a constant voltage of 3 V in both the presence and absence of blue laser light irradiation (80 mW/cm^2) on mediator electrodes.

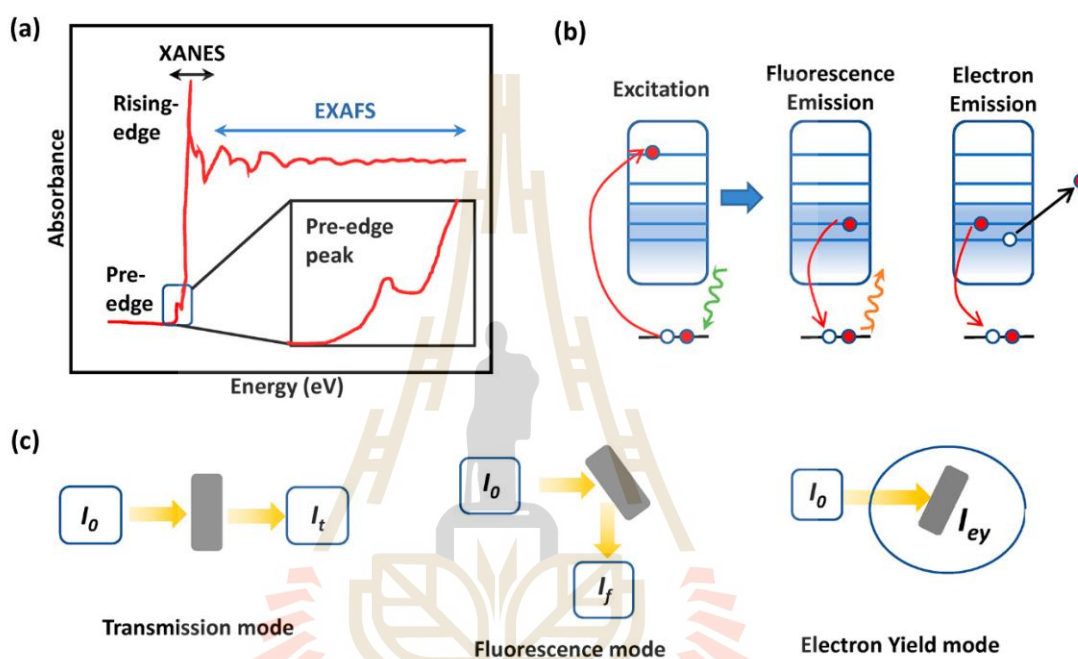


Figure 3.11 (a) XAS diagram, showing the pre-edge, X-ray absorption near edge structure (XANES), and X-ray absorption fine structure (EXAFS) areas. (b) The spectrum of XAS. (c) Three distinct ways of XAS detection: transmission, fluorescence, and electron yield (Jin and Seifitokaldani, 2020).

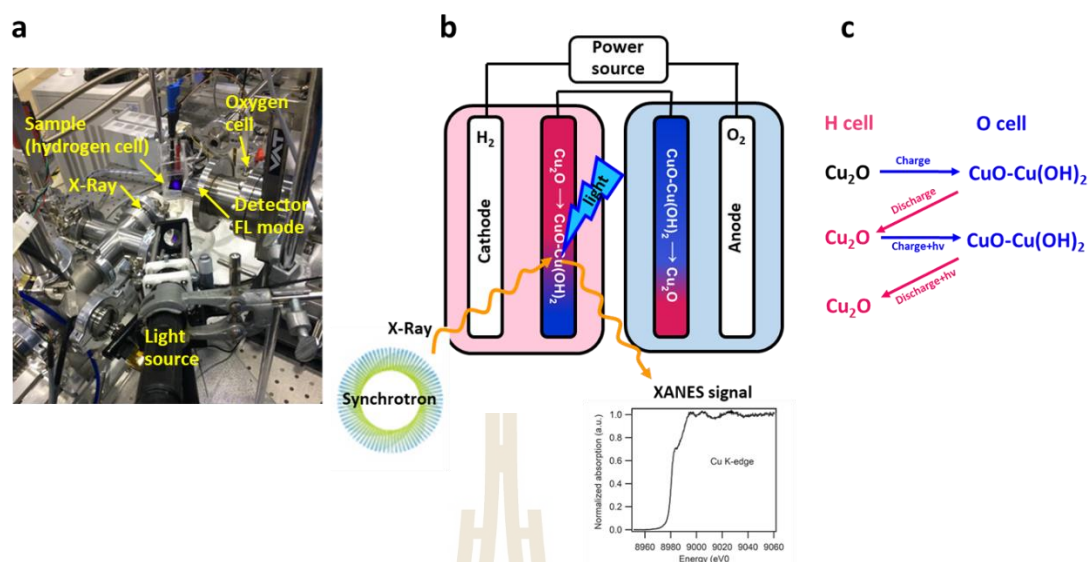


Figure 3.12 (a) *In situ* Cu K-edge fluorescence measurement setup, (b) schematic, and (c) process of electrolysis operation of mediator electrode during charging and discharging under dark and blue light illuminations in two-cell water electrolysis at 3 V.

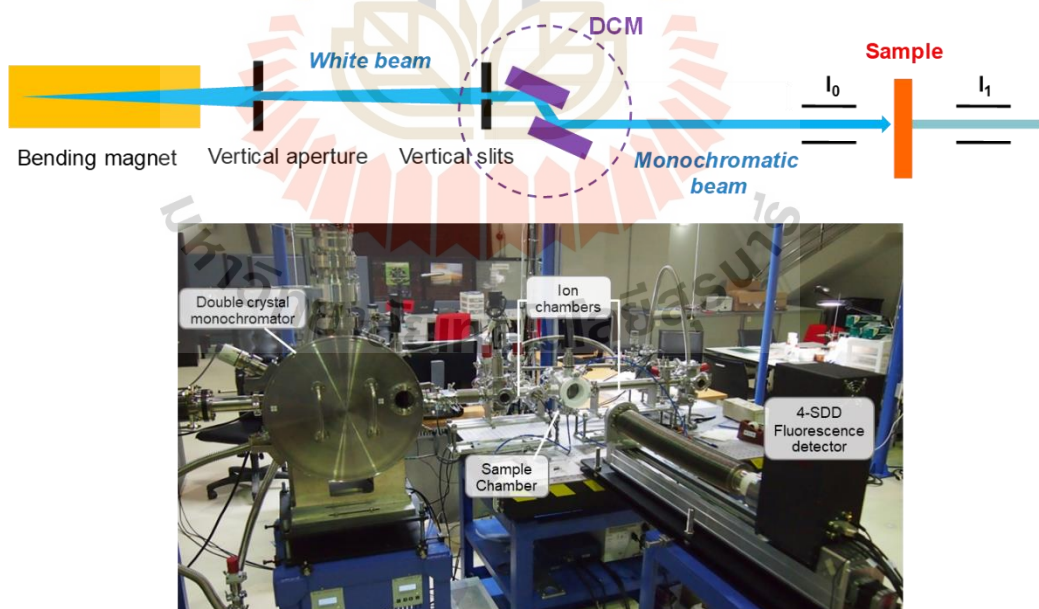


Figure 3.13 XAS setup at beamline 5.2.

3.6 Photoemission spectroscopy (PES)

PES is an experimental standard tool for surface analysis, it excels very high surface sensitivity, due to the very small electron mean free paths of electrons with kinetic energies in the range of 10-2000 eV (typically 1-2 nm). PES involves bombarding a sample with high-energy radiation, generally UV or X-ray, which results in the ejection of electrons from the material. The ejected electrons go from the sample to an energy analyzer, which records their kinetic energies, and then to a detector, which counts the number of photoelectrons at different kinetic energies. Below is a simplified diagram of this procedure (Figure 3.14).

The energy required to eject an electron from the sample is known as the electron's ionization energy or binding energy. We know the energy of the radiation ($h\nu$) used to eject the electron. So, by measuring the kinetic energy of the photoelectron (KE), we can calculate the binding energy (BE) of the electron in the sample from the following Equation 3.8 (Benigna, 2014):

$$BE = h\nu - KE - \phi \quad (3.8)$$

where ϕ is the work function induced by the analyzer.

The binding energy of an electron in an atom is location-dependent around the nucleus (Figure 3.15). Since electrons in the outermost shell (valence electrons) are shielded and farther away from the nucleus on average, they have the lowest binding energies of all the electrons in an atom. In contrast, electrons in inner shells (core electrons) are less shielded and are generally closer to the nucleus, resulting in greater binding energies. Understanding the link between the binding energy of an electron and its position is critical for interpreting PES data.

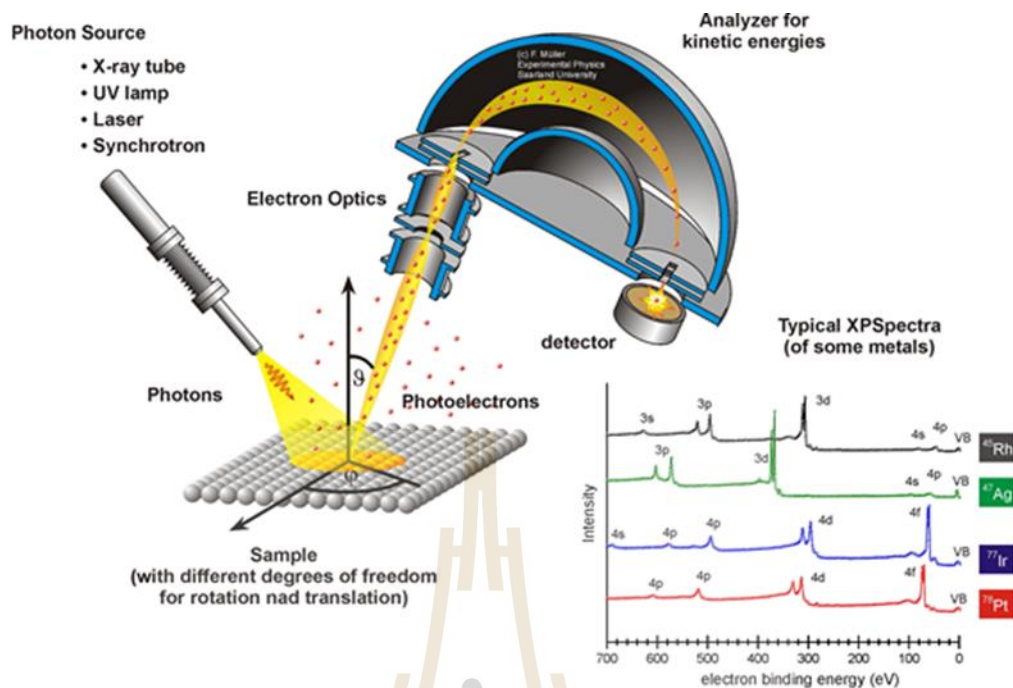


Figure 3.14 A typical XPS setup is shown schematically. It includes a photon source (X-rays, UV-light, laser, or synchrotron radiation), sample manipulation with several degrees of freedom in linear and rotational directions, electron optics, and dispersive energy analyzer, and a detector. XPS spectra (intensity vs. binding energy) of four different metals are illustrated with their element-specific distribution of core-level photoemission.

PES data are shown as photoelectron count vs. binding energy, with binding energy typically expressed as electron volts (eV). A typical PES spectrum has peaks corresponding to various binding energies. Because electrons in the same subshell of an atom have the same binding energy, each of these peaks represents electrons in a distinct subshell. The peak of binding energy indicates the amount of energy necessary to remove one electron from the subshell, while the peak's intensity indicates the subshell's relative electron number.

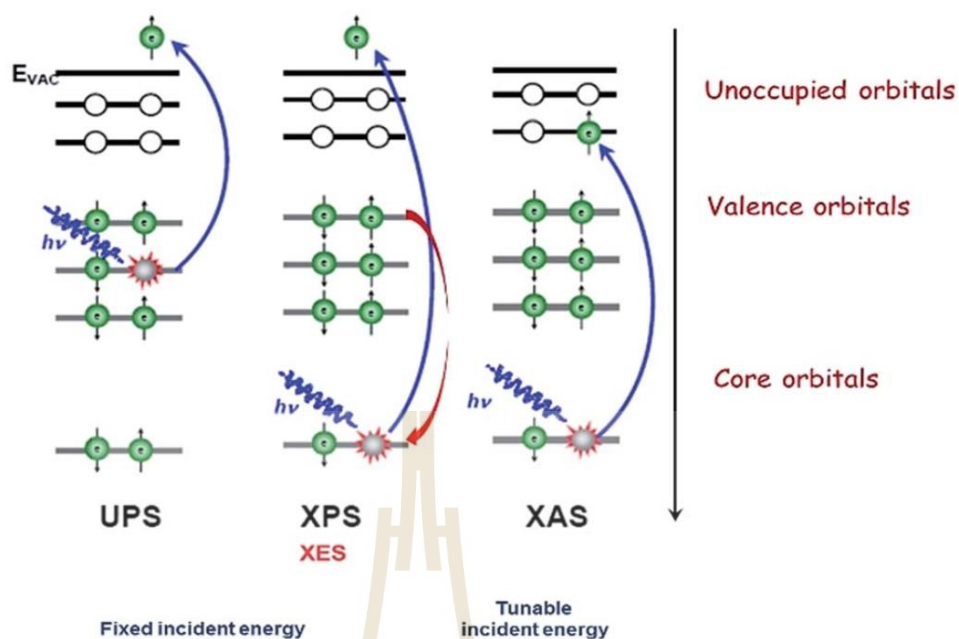


Figure 3.15 The type of core-level spectroscopies: ultraviolet photoelectron spectroscopy (UPS), X-ray photoelectron spectroscopy (XPS), X-ray absorption spectroscopy (XAS) and X-ray emission spectroscopy (XES) (Chergui, 2014).

In this work, we're going to use PES to understand the influence of light during electrolysis. The electronic structures of the mediator electrodes under blue laser light irradiation (80 mW/cm^2) were investigated by using ultraviolet photoemission spectroscopy (UPS) at room temperature with a photon energy of 90 eV and base pressure $<1 \times 10^{-8}$ mbar. The valence band spectra were collected on a Scienta R4000 analyzer at BL3.2a of the Synchrotron Light Research Institute (SLRI), Thailand.

CHAPTER IV

RESEARCH METHODOLOGY

This work reports a significant enhancement in the performance of a two-cell water splitting device by using a CuO-Cu(OH)₂/Cu₂O mediator electrode under solar irradiation. The experimental results and their discussion on the study of photo-enhanced water electrolysis in separate O₂ and H₂ cells using pseudocapacitive electrodes (CuO-Cu(OH)₂ and Cu₂O) are reported in this chapter. This chapter is divided into four sections. The first section describes the characterization of the CuO-Cu(OH)₂ electrodes. The characterization of the samples was done by various techniques in order to understand morphology, chemical composition, and microstructure using a scanning electron microscope (FESEM), energy dispersive X-ray (EDX), X-ray Diffraction (XRD). The Second section is the electrochemical properties of CuO-Cu(OH)₂/Cu₂O mediator electrodes. In the third section, two-cell water electrolysis was set up and operated under dark and solar irradiation. This section present a concept providing a significant enhancement in the production of pure gases in a two-cell water electrolysis system by using charge-discharge Cu₂O/CuO-Cu(OH)₂ redox mediator electrodes under solar irradiation. Finally, the electronic structure of CuO-Cu(OH)₂/Cu₂O during electrolysis in a two-cell water splitting system was *in-situ* X-ray absorption near edge structure (XANES), and X-ray photoemission spectroscopy (XPS).

4.1 Characterization of the CuO-Cu(OH)₂ electrodes

4.1.1 Scanning electron microscopy

The surface morphologies of the as-prepared electrode directly grown onto copper foil via surface oxidation in alkaline solution were investigated by scanning electron microscopy. Figure 4.1b shows the SEM image of the cleaned copper foil after pre-treated. At the reaction time of 15 mins 25°C, the Cu(OH)₂-CuO forms a blue thick film and covers the entire copper substrate uniformly and compactly at low magnification (Figure 4.1a and 4.1c). The higher magnification SEM image (Figure 4.1d and 4.1e) shows that the film is composed of nanowires and flower-like. The micro- flowers are standing on nanowire arrays. The length of a single nanowire is up to around 6 μm, with a width of about 200 nm. The flower-like is evident with a diameter of 6 μm, and the thickness of the flower petals is approximately 40-70 nm.

The SEM image of CuO-Cu(OH)₂ electrode after activation process was 300 activation cycles with charge and discharge steps at a constant current of 30 mA (5 A/g or 3 mA/cm²). After activation, the Cu(OH)₂ nanowire transform to CuO flower petals. Their nanoscale thickness and diameter of about 1 μm, as shown in Figures 4.2a and 4.2b.

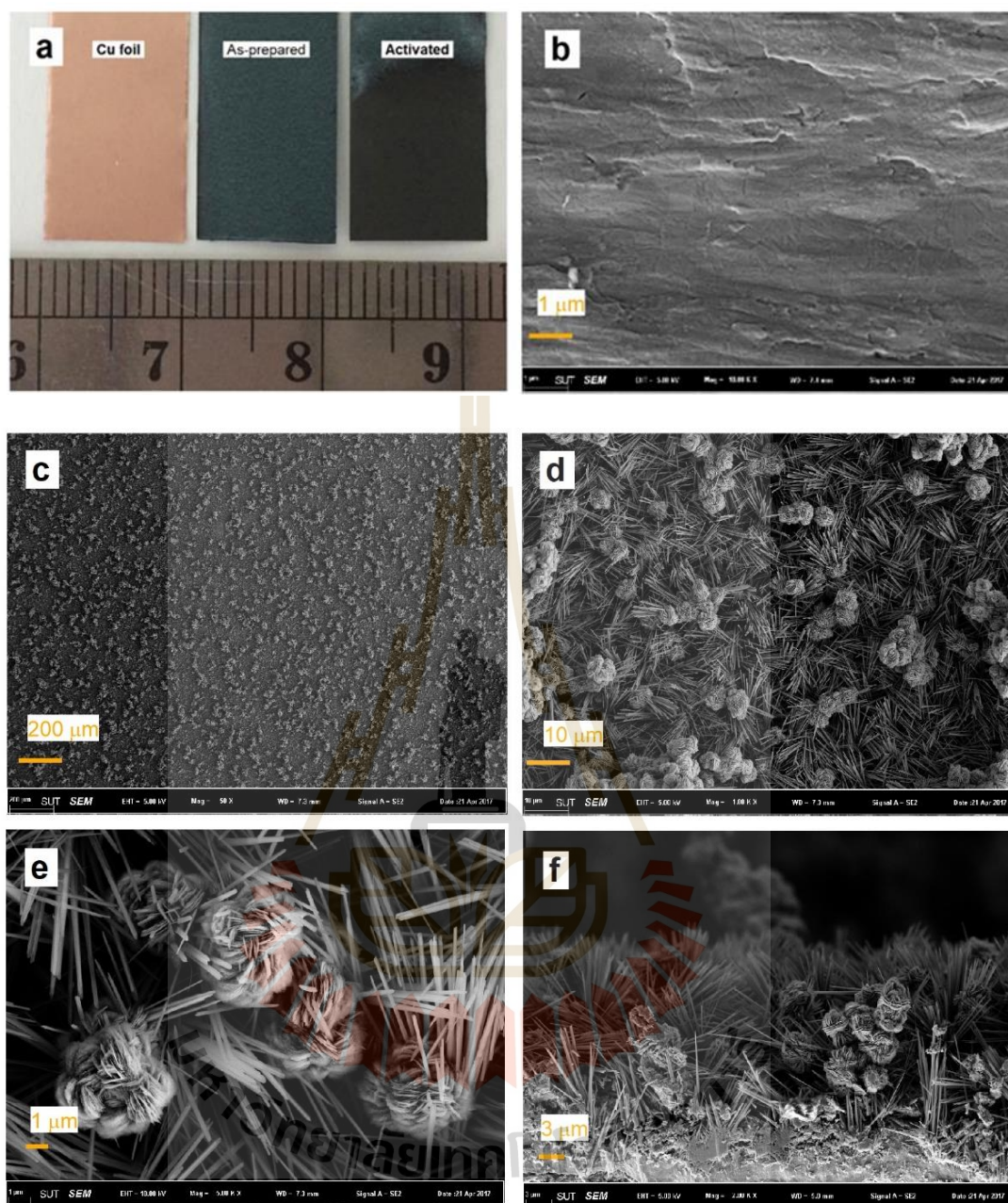


Figure 4.1 SEM micrographs of As-prepared electrode. (a) photograph of electrode before and after surface oxidation thick films. (b) pre-cleaned Cu-foil. (c)-(f) As-prepared electrode.

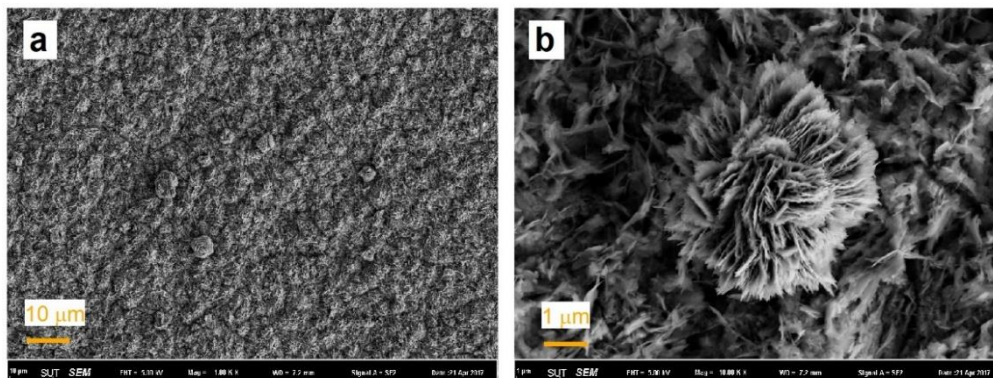


Figure 4.2 SEM micrographs of activated electrode.

Many studies supported these results; Cao's group and Yu's group report that electro-active materials were grown onto Cu-foil via surface oxidation in an alkaline solution composed of $\text{Cu}(\text{OH})_2$ nanowires and CuO micro-flower (Wang et al., 2015; Xu et al., 2015). Therefore, these results confirmed that the $\text{Cu}(\text{OH})_2$ and CuO nanostructure were formed on a Cu substrate. Then $\text{Cu}(\text{OH})_2$ nanowire have transferred into $\text{CuO-Cu}(\text{OH})_2$ nanosheets completely after charge-discharge of 300 cycles in NaOH electrolyte.

4.1.2 EDS analysis

EDS analyses were performed on several nanowires and micro-flower structures. The results obtained from the analysis of each structure shown in SEM images are tabulated in the Table 1 and 2 on the right-hand side of the SEM image. The Cu/O ratios of micro-flower structure are 2/3, ascribed to the $\text{CuO-Cu}(\text{OH})_2$. In the nanowires structure case, the Cu/O ratios are 1/2, which indicate to the $\text{Cu}(\text{OH})_2$.

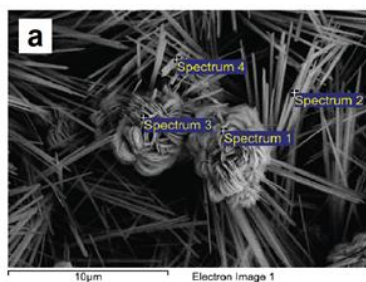


Table 1

Spectrum	Cu (at%)	O (at%)	C (at%)	Total	
1	40.98	54.35	4.68	100	CuO-Cu(OH) ₂
2	32.59	62.70	4.71	100	Cu(OH) ₂
3	41.39	54.62	3.99	100	CuO-Cu(OH) ₂
4	33.15	61.61	5.24	100	Cu(OH) ₂

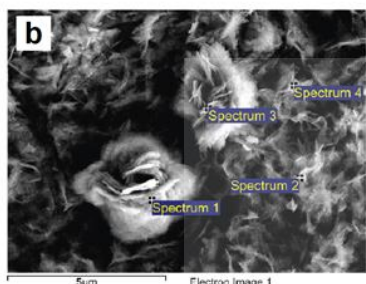


Table 2

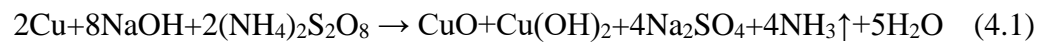
Spectrum	Cu (at%)	O (at%)	C (at%)	Total	
1	40.47	53.15	6.38	100	CuO-Cu(OH) ₂
2	40.47	52.96	6.57	100	CuO-Cu(OH) ₂
3	40.67	51.89	7.45	100	CuO-Cu(OH) ₂
4	40.12	52.64	7.24	100	CuO-Cu(OH) ₂

Figure 4.3 EDS analysis. Quantitative chemical composition analysis of as- prepared and after activation process electrodes taken 4 selected sites as shown in the SEM image ((a) and (b)). (a) The SEM image of as-prepared electrode. (b) The SEM image of activated electrode. Table 1 EDS data recorded on the as-prepared sample. Table 2 EDS data recorded on the sample after activation process (charge-discharge of 300 cycles).

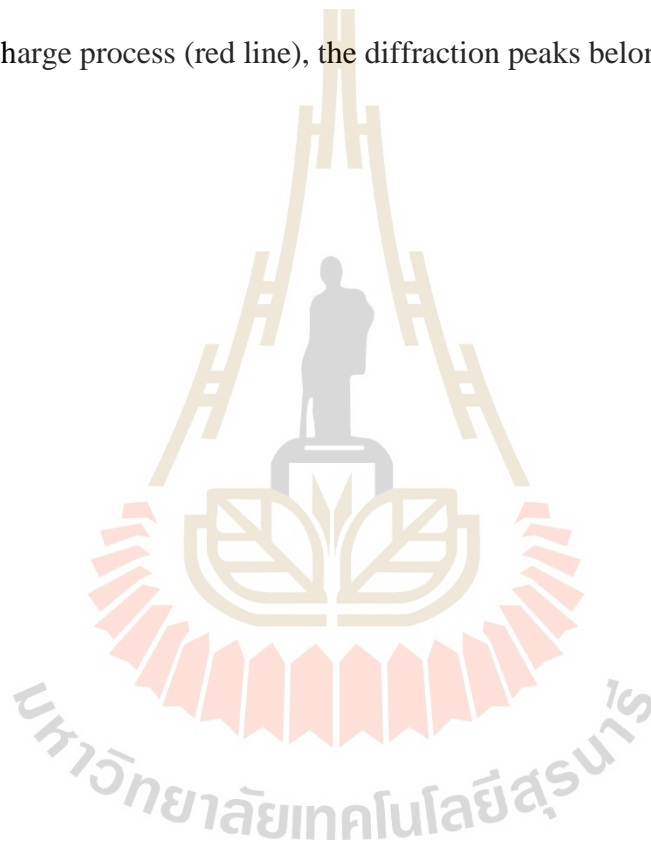
4.1.3 XRD analysis

The crystal phases of the samples after chemical oxidation (as-prepared), then charged and discharged electrodes in NaOH electrolyte were determined using XRD, as shown in Figure 4.4. After chemical oxidation, the XRD pattern of as-prepared electrode present strong diffraction peak indexed to the Cu substrate (JCPDS file no. 04-0836), orthorhombic Cu(OH)₂ (JCPDS file no. 80-056) and monoclinic CuO (JCPDS file no. 80-1916) perfectly. This indicates that the Cu(OH)₂/CuO nanostructure could be formed on a Cu substrate by the surface oxidation of copper in alkaline

solution as expressed by the following Equation 4.1, according to literature (Xu et al., 2015).



To better understand the charge storage mechanism, XRD patterns of the electrode after 50 cycles at 4 A/g in the range 0-0.6 V were also recorded. After the charging process (blue line), the diffraction peaks of CuO and Cu(OH)₂ can be observed simultaneously. After the discharge process (red line), the diffraction peaks belong to Cu₂O and CuO.



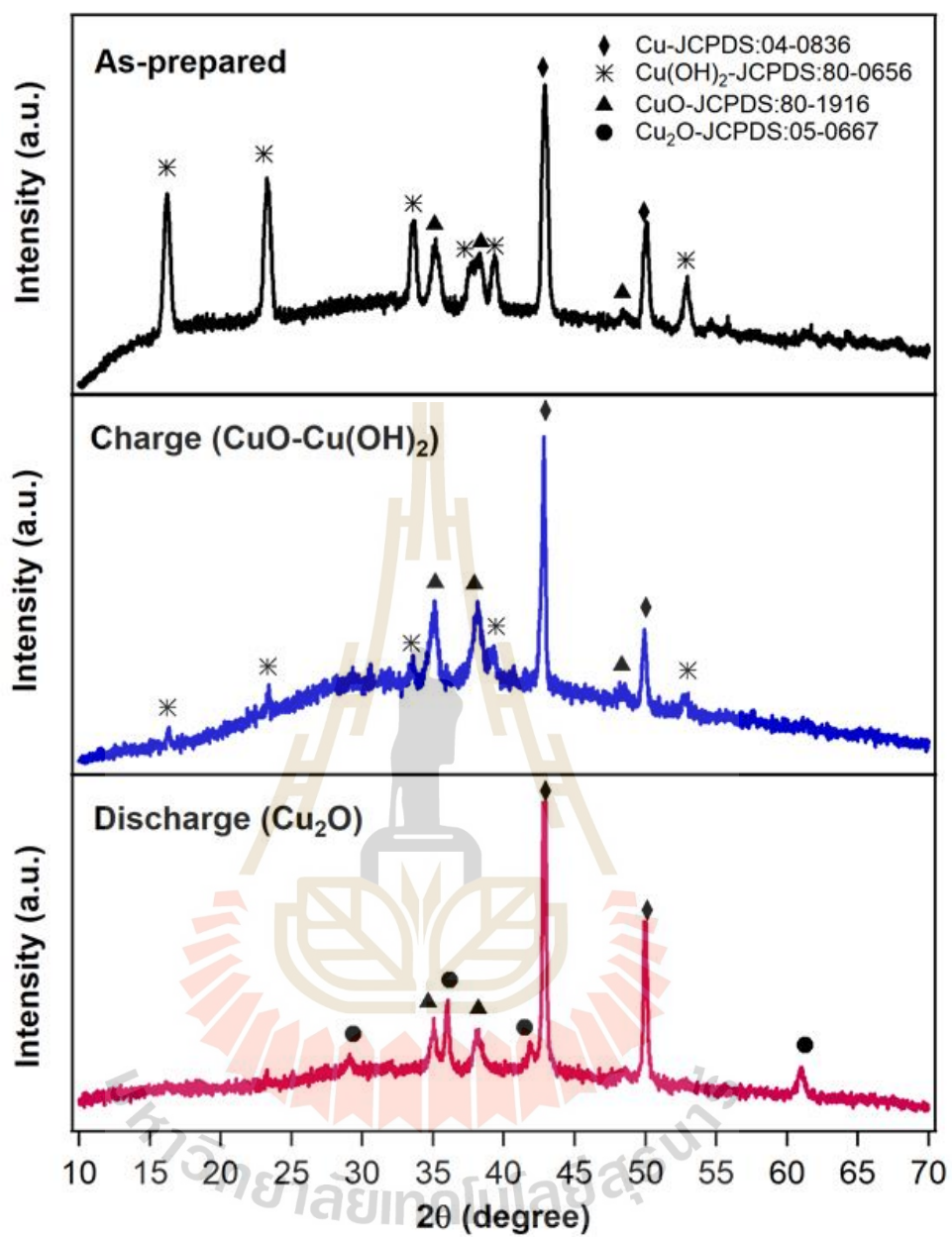


Figure 4.4 XRD patterns of as-prepared, charged (CuO-Cu(OH)₂) and discharged (Cu₂O) electrodes.

4.2. Electrochemical properties of electrodes

4.2.1 Cycle voltammogram (CV) and galvanostatic charge–discharge (GCD) measurements

The performance of electrodes could be evaluated with cycle voltammogram (CV) and galvanostatic charge–discharge (GCD) measurements. Figure 4.5a and 4.6a show the results of the CV studies of the as-prepared Cu(OH)₂-CuO on Cu-foil electrode (the geometrical area of 1 cm²) in 1M NaOH solution at various scan rates in -2 V to 0.9 V and 0 V to 0.8 V, respectively. The CV curves show lower slopes for lower scan rates, which indicates that lower scan rates allow a longer duration for the anions to access the bulk of the electrode; thereby showing ideal capacitive behavior. However, with increasing scan rate the anodic peak shifts towards positive potentials and the cathodic peak shifts towards negative potentials as has been observed conventionally. This demonstrates the quasi-reversible nature of redox reaction.

The CV curves of electrode are quite different from the ideal rectangular shape for double layer capacitance indicating that the electrodes possess pseudo-capacitance properties. The specific capacitance of the electrode could be calculated from the cathodic or anodic part of the CV data using the Equation 4.2 (Xu et al., 2015):

$$C_s = \frac{1}{mv(E_2 - E_1)} \int_{E_1}^{E_2} i(E) dE \quad (4.2)$$

where E_1 and E_2 are the cutoff potentials in the CV curves and $i(E)$ is the current at each potential, $E_2 - E_1$ is the potential window, v is the scan rate and m is the mass of the active materials. In this work, the mass loading of Cu(OH)₂-CuO on Cu substrate is around 0.5 to 1.7 mg/cm². The specific capacitance for Cu(OH)₂-CuO/Cu-foil electrode, based on CV curves are more than 400 F/g as show in Figure 4.5b and 4.6b.

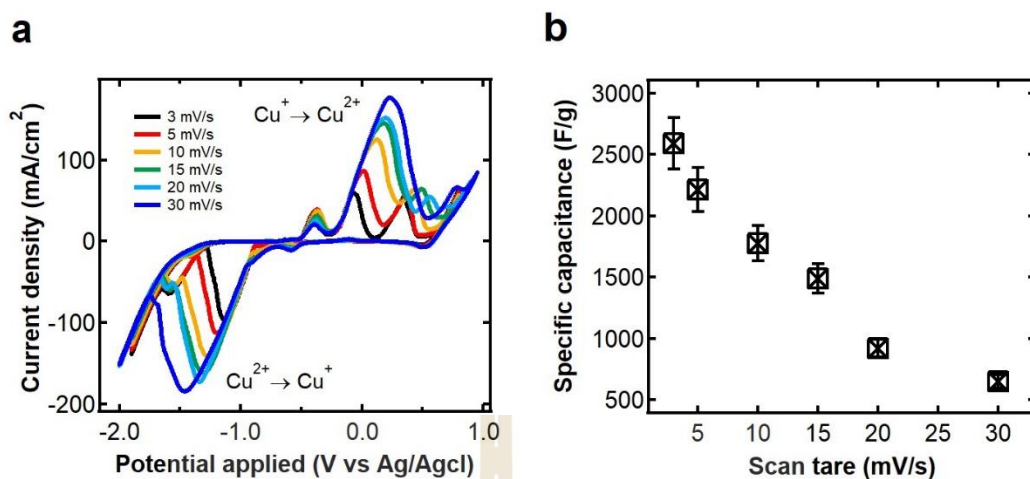


Figure 4.5 Electrochemical properties of electrode in potential window of -2 V to 0.9 V. (a) Cyclic voltammetry of electrode at different scan rate. (b) Variation of specific capacitance as a function of scan rate.

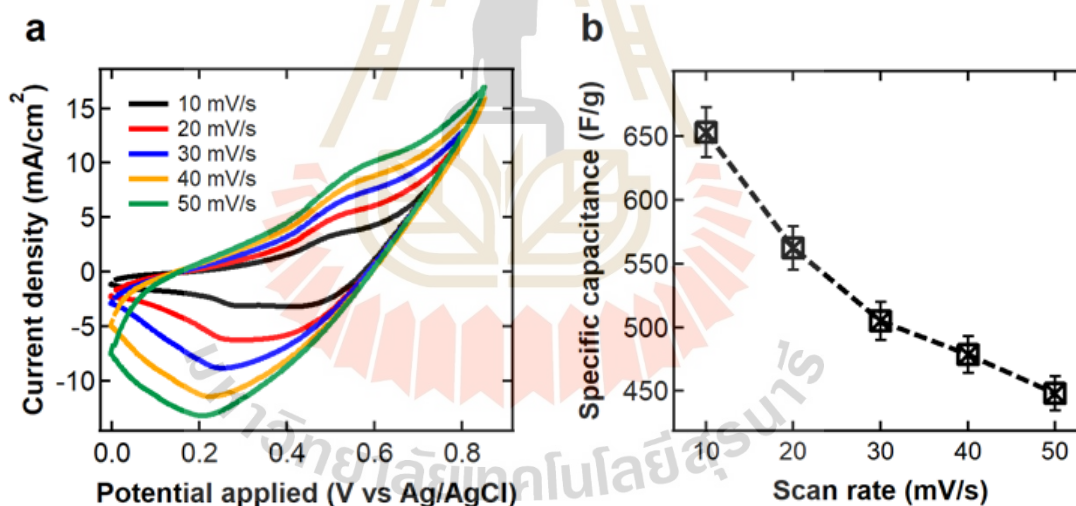


Figure 4.6 Electrochemical properties of electrode in potential window of 0 V to 0.9 V. (a) Cyclic voltammetry of electrode at different scan rate. (b) Variation of specific capacitance as a function of scan rate.

Apparently, when the voltage is beyond 0.8 V, the system occurs oxygen evolution phenomenon, thus the GCD measurement was tested in the potential window of -1.3 V to 0.55 V and 0 V to 0.6 V in 1M NaOH (Figure 4.7a and 4.8a) at constant

current. The obvious non-linear shape of the discharge curves further reveal that the capacitance of electrodes is not pure double-layer capacitance, but a pseudo-capacitance, involving a faradic capacitance, which mainly originates from the redox reactions. The specific capacitance of the electrodes can be calculated from the discharge curves using the following Equation 4.3 (Xu et al., 2015),

$$C_m = \frac{I_d \Delta t}{m \Delta V} \quad (4.3)$$

where C_m (F/g) is the specific capacitance, I_d (mA) is the discharge current, Δt (s) is the discharge time, ΔV (V) is the discharge potential range, and m (mg) is the mass of active materials. The specific capacitance values of the electrode (Figure 4.7b and 4.8b) in each potential range are in good agreement with the CV curves (Figure 4.5b and 4.6b). The potential drop between the charge and discharge curves (IR drop) is 0.005 V, which is generally caused by internal resistance and incomplete faradic reaction in the electrode.

4.2.2 Mediator electrodes activation

To ensure the stability of process during electrolysis, our CuO-Cu(OH)₂ electrodes were activated using the continuous charge/discharge process prior to fabricating the electrolytic cell. After activation, Cu(OH)₂ nanowires transform to CuO nanosheets with thickness approximately 50-100 nm as shown in Figure 4.1 and Figure 4.2, respectively. The changing of morphology provides large electrode-electrolyte interface for efficient redox reaction (see cyclic voltammetry (CV) curves in Figure 4.9a). The charge transfer and electrolyte diffusion resistance are smaller (Figure 4.12a) leading to its specific capacitance in a potential range of -1.3-0.6 V vs Ag/AgCl which becomes larger than as-prepared electrode (Figure 4.9a).

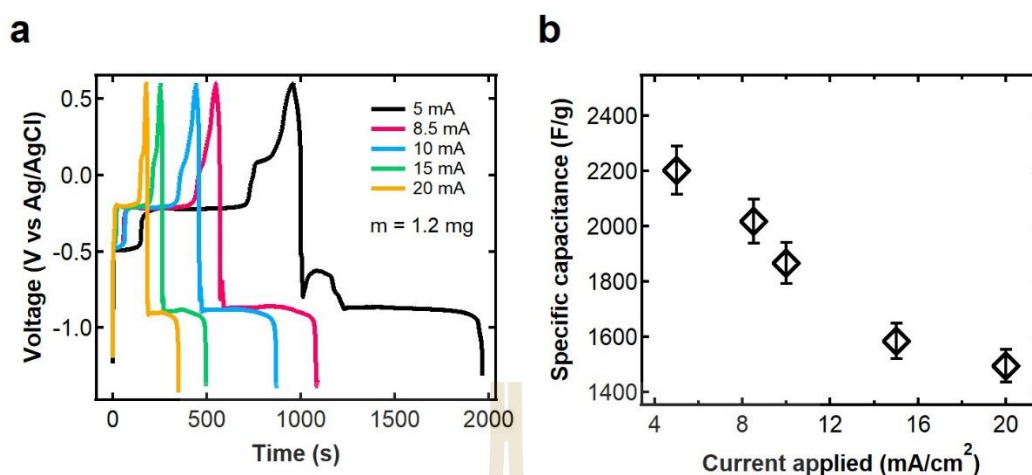


Figure 4.7 Electrochemical properties of electrode. (a) Charge-discharge curves of electrode at different current densities. (b) Variation of specific capacitance as a function of current density.

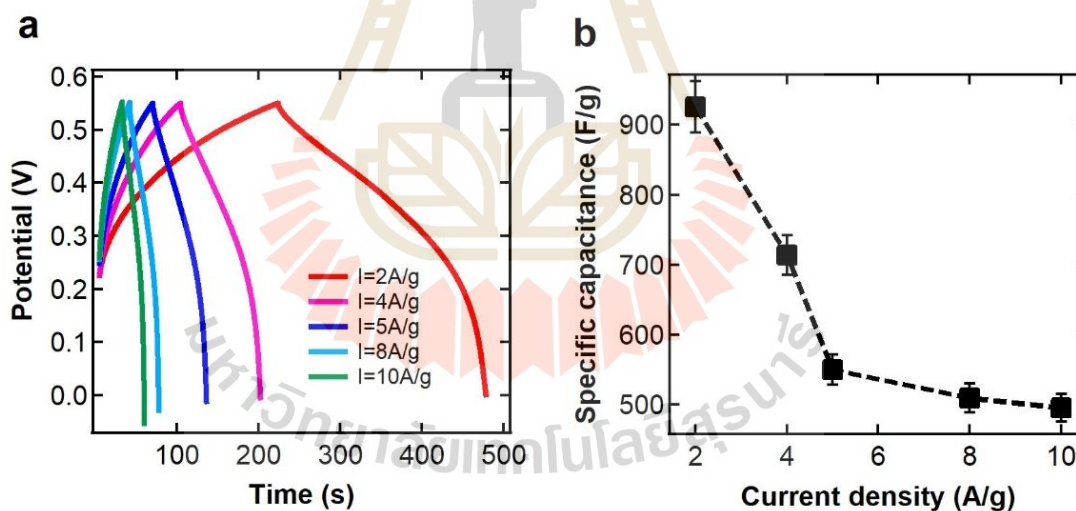


Figure 4.8 Electrochemical properties of electrode. (a) Charge-discharge curves of electrode at different current densities. (b) Variation of specific capacitance as a function of current density.

The cyclic stability of $\text{CuO-Cu(OH)}_2/\text{Cu}_2\text{O}$ mediator electrodes (measurement area 1 cm^2) was investigated by continuous charging and discharging for 1000 cycles

at a current density of 10 mA/cm^2 (8.3 A/g) in 1 M NaOH solution within the potential range of -1.3 - 0.6 V vs Ag/AgCl . The specific capacitance curve shows an excellent retention rate as shown in Figure 4.9b. The specific capacitance was measured to be $1,725 \text{ F/g}$ after 1000 cycles, around 92% compared to that of the initial activated electrode (highest specific capacitance is $1,867 \text{ F/g}$).

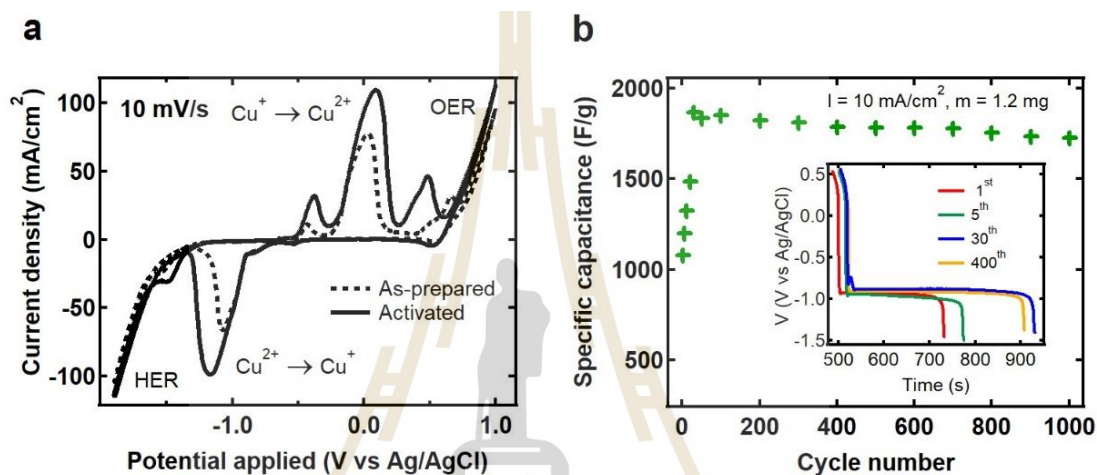
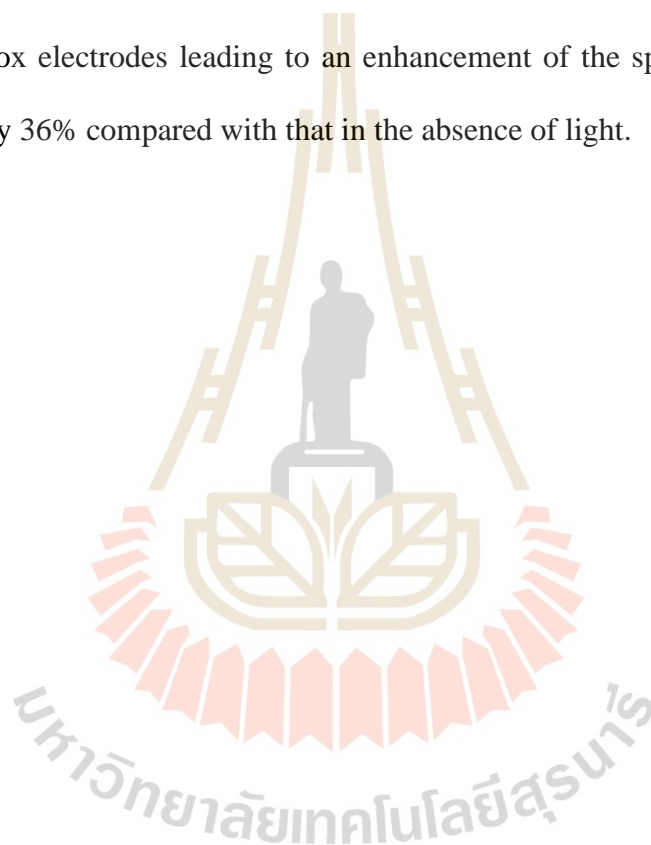


Figure 4.9 (a) CV curves of CuO-Cu(OH)_2 electrode before and after activation process at 10 mV/s with potential range from -2 V to 1 V vs Ag/AgCl . (b) The cycling stability and galvanostatic discharge curves (inset) of $\text{CuO-Cu(OH)}_2/\text{Cu-foil}$ electrode by charge/discharge measurement at 10 mA/cm^2 and -1.3 - 0.6 V vs Ag/AgCl in 1 M NaOH .

4.2.3 Electrochemical properties of electrodes under dark and sunlight illumination

To further elucidate the effect of solar irradiation on our system, the electrochemical properties of the $\text{CuO-Cu(OH)}_2/\text{Cu}_2\text{O}$ mediator pairs were investigated. The resulting cyclic voltammetry (CV) measurement is shown in Figure 4.10-4.12. This further supports evident that the $\text{CuO-Cu(OH)}_2/\text{Cu}_2\text{O}$ redox electrode

provides a higher current density and specific capacitance under light irradiation (solar irradiation and laser light). The specific capacitance was calculated following Equation 4.2 and then plotted vs the applied scan rates, as shown in Figure 4.10d and 4.12d. The specific capacitance exponentially decreased as the increasing of scan rate due to the diffusion limit. Photogenerated charge carriers drive the oxidation and reduction (An et al., 2019; Kalasina et al., 2017; Kalasina et al., 2018; Xia et al., 2012) of $\text{Cu}_2\text{O}/\text{CuO}-\text{Cu}(\text{OH})_2$ redox electrodes leading to an enhancement of the specific capacitance by approximately 36% compared with that in the absence of light.



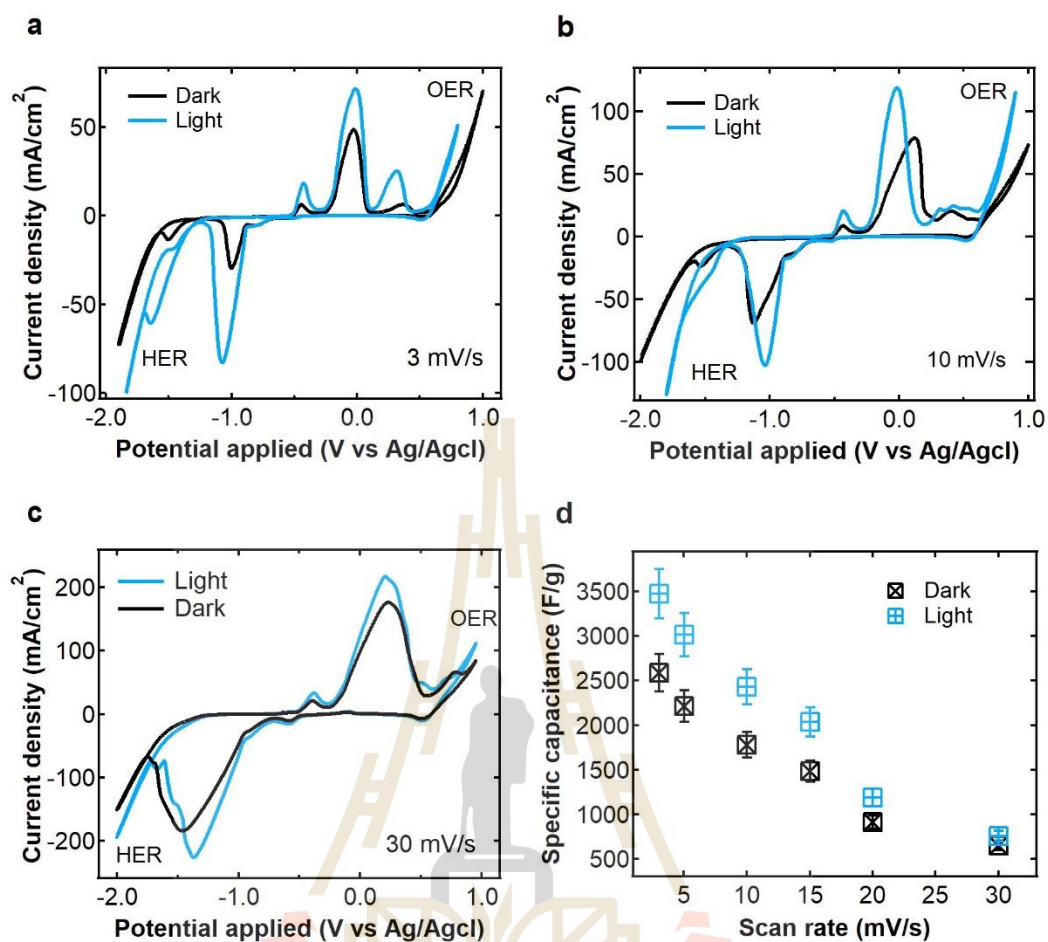


Figure 4.10 Effect of sunlight on CuO-Cu(OH)₂/Cu₂O redox mediator electrode. (a), (b), and (c) CV curve of CuO-Cu(OH)₂ electrode taken at the scan rate of 3, 10, 30 mV/s, respectively, under dark and sunlight illuminations. (d) Variation of specific capacitance as a function of scan rate under dark and sunlight illumination.

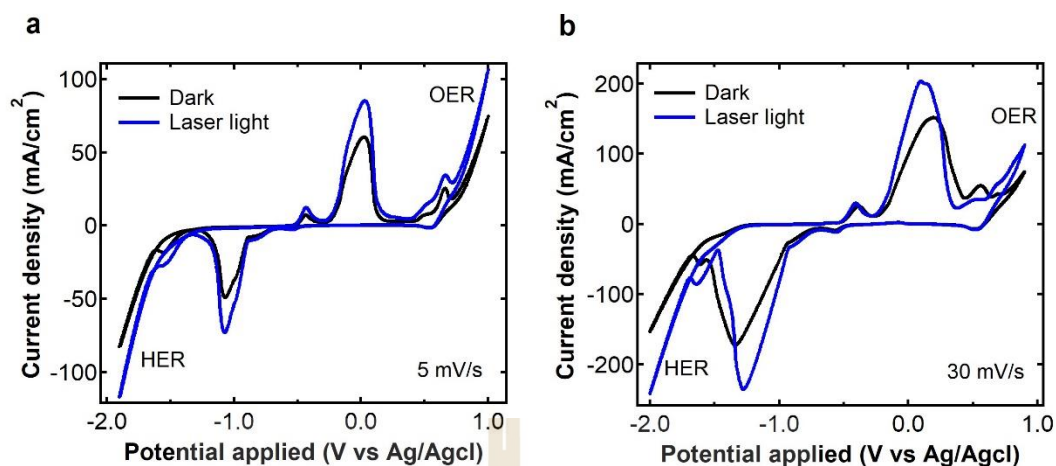


Figure 4.11 Effect of laser light (450 nm) on CuO-Cu(OH)₂/Cu₂O redox mediator electrode. (a) and (b) CV curve of CuO-Cu(OH)₂ electrode at 5 and 30 mV/s, respectively, in three electrode electrochemical under dark and laser light illumination.

GCD of the half-cell electrode was further investigated by applied the constant current density ($I=4$ A/g) under a potential range of 0-0.6 V. The GCD curve under irradiation display a longer charge/discharge time than that in dark condition, indicating the different charge storage mechanisms in these two conditions.

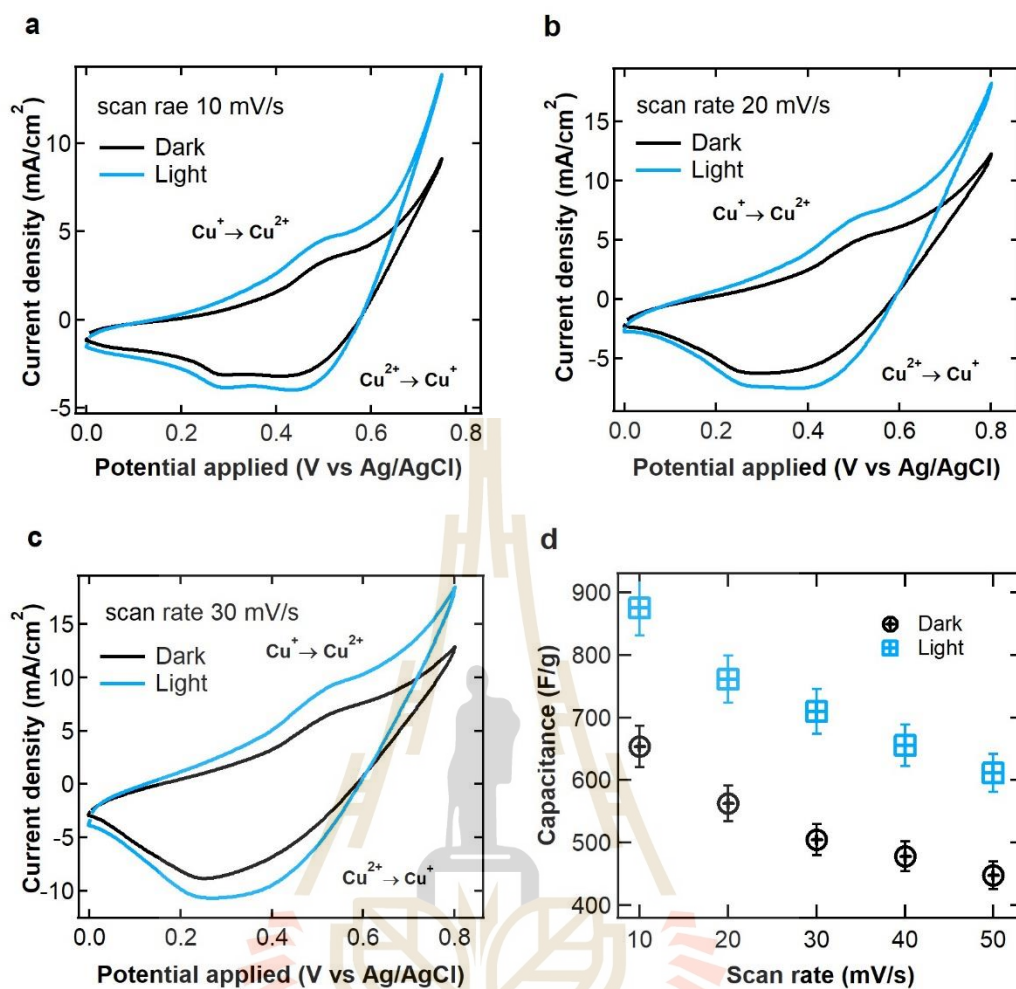


Figure 4.12 (a)-(c) CV curves of the half-cell electrode under dark and sunlight illumination at 10, 20, and 30 mV/s, respectively. (d) Specific capacitance of CuO-Cu(OH)₂ electrode under dark and solar irradiation.

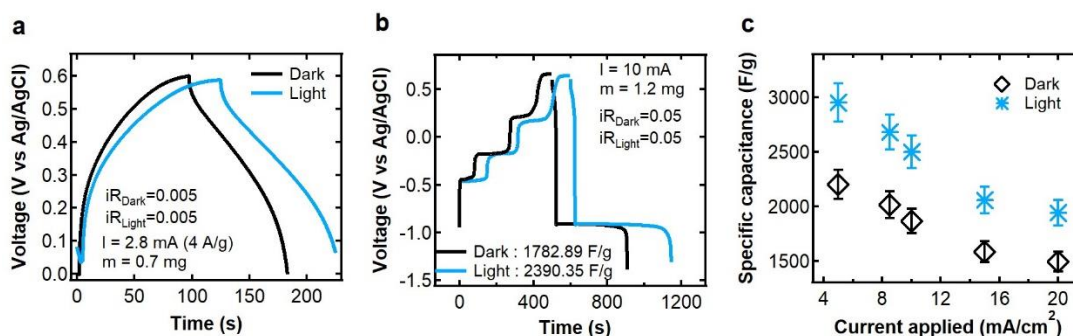


Figure 4.13 (a) and (b) Galvanostatic charge-discharge profiles under dark and sunlight condition at constant currents in a potential range of 0 to 0.6 V and -1.5 to 0.5 V vs Ag/AgCl, respectively. (c) Specific capacitance as a function of current density under a dark condition and a light illumination.

4.2.4 Electrochemical impedance spectroscopy study of electrodes

For activation process, it can be improving the stability of process and specific capacitance of electrodes. To clarify the mechanism, EIS study were carried out. The main propose of the EIS experiments is to study the effect of NaOH on the interfacial properties of electrodes (capacitance and charge transfer resistance). Figure 4.14a shows the Nyquist plots of the As-prepared and activated electrode after charge-discharge of 5, 30 and 400 cycles, which were measured at open circuit potential in 1M NaOH solution. All the plots consisted of approximately a semicircle at high frequency and a linear region at low frequency. The intercept of the semicircle on real axis at high frequency represents solution resistance (R_s), diameter of semicircle corresponds to the charge transfer resistance (R_{ct}). The diameter of semicircle corresponds to charge transfer resistance (R_{ct}) caused by Faradic reactions (Li et al., 2014), due to $\text{Cu}^{2+}/\text{Cu}^+$ redox couple. The result as shown in Figure 4.14a can be seen that the charge-transfer resistance decreased with increasing the activated cycles. In the low frequency, the

inclined straight line corresponds to Warburg impedance (Z_w) related to the diffusion of electrolyte within the CuO-Cu(OH)_2 structures. The straight line part leans more toward the imaginary axis, indicates that the electrode has a good capacitive behavior (Zhang et al., 2013). In Figure 4.14b, the appearance of semi-circular feature of EIS measurement both in the dark and solar irradiation was observed, suggesting that charge transfer resistance controls the kinetics at the electrode interface. This result shows the arc radii under illumination were smaller than that in the dark, which is due to the increased electron conductivity of the electrodes when irradiated.

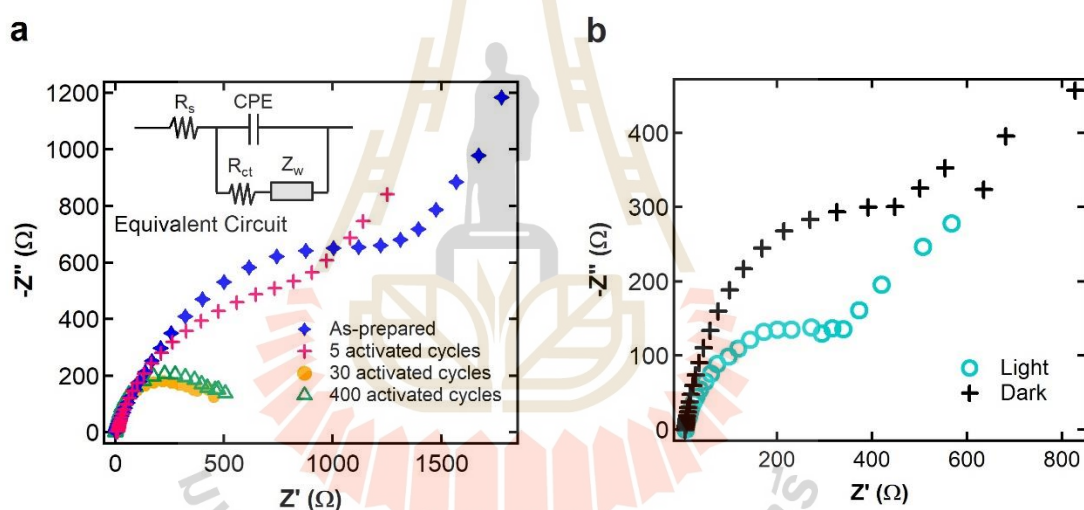


Figure 4.14 Electrochemical impedance spectroscopy study of electrodes in a three-electrode system. (a) EIS plot of the as-prepared and activated electrodes after charge-discharge of 5, 30 and 400 cycles. (b) EIS plot of electrode under dark and light irradiation.

4.2.5 UV-visible spectra

To gain better understanding the property–function relationship of the materials, their electronic properties of $\text{CuO-Cu(OH)}_2/\text{Cu}_2\text{O}$ and their intermediates were further

investigated by UV-visible spectrometry. Figure 4.15 shows the UV-visible spectra of the as-prepared, after charge (CuO-Cu(OH)_2), and after discharge (Cu_2O) electrodes, which all are dispersed in DI-water. The absorption spectrum of the as-prepared and after charge (CuO-Cu(OH)_2) electrodes show the same result which are Ultraviolet (UV) region. While the absorption spectrum of after discharge electrode covers UV-visible light region and displays the highest intensity at 280 nm and 480 nm.

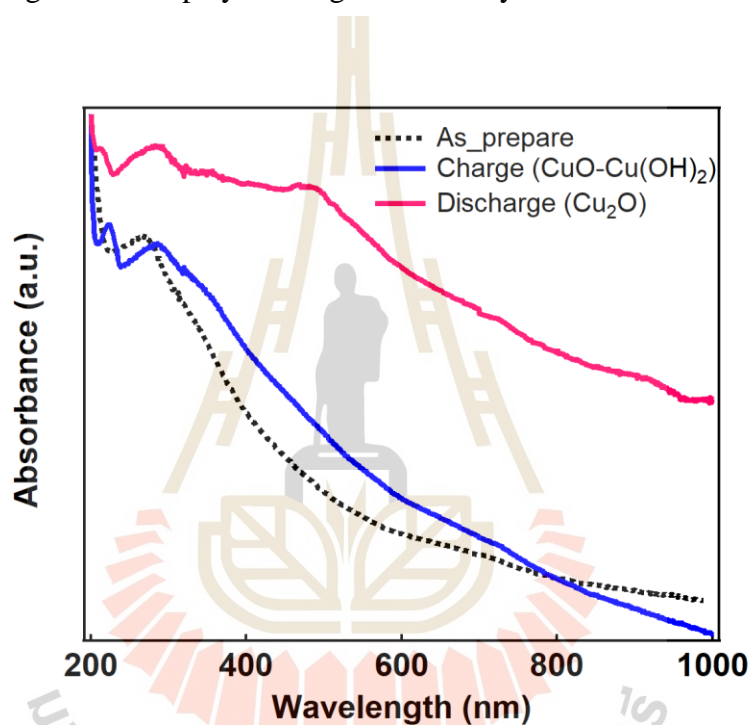


Figure 4.15 UV-vis spectra of as-prepared (black dash line), CuO-Cu(OH)_2 (blue line) and Cu_2O (red line) electrodes dispersed in DI water.

4.3 The operation of two-cell water electrolysis system.

A $\text{CuO-Cu(OH)}_2/\text{Cu}_2\text{O}$ redox couple (active area = 10 cm^2 and active material = 24 mg) was used as a mediator electrode in a two-cell water electrolysis system, as shown in the Figure 4.16. The Cu_2O is used in the hydrogen production cell and CuO-Cu(OH)_2 is used in the oxygen production cell. Electrons are transferred from Cu_2O to

CuO-Cu(OH)₂ and ions (OH⁻) are exchanged between the primary electrodes (cathode and anode) by charging and discharging of the Cu₂O/CuO-Cu(OH)₂ mediator electrodes. The CuO-Cu(OH)₂ convert to Cu₂O during O₂ production at the anode (4OH⁻→O₂+2H₂O+4e⁻), while Cu₂O simultaneously converts to CuO-Cu(OH)₂ during H₂ production at the cathode (4H₂O+4e⁻ → 2H₂+4OH⁻). This process is accompanied by a visible color change from red to dark blue (see Figure 4.16b). The charge and discharge cycle of the mediator pair depends on the reversible transformation of CuO-Cu(OH)₂/Cu₂O, which typically falls within the potential range of -1.2 to 0.7 V(Guan et al., 2017; Xu et al., 2019; Xu et al.; Zaaferany and Boller, 2009) (Figure 4.16). The electrochemical reactions are as follows:



The proposed system can be continuous operation by cycling (charge/discharge) of the Cu₂O and CuO-Cu(OH)₂ mediator electrode (Figure 4.17). They can be easily recharged by switching the applied voltage between the anode and cathode. In fact, the cycle duration can be adjusted easily. It's depending on the charge of the mediator electrode, on the applied voltage and on the electrolysis current. Therefore, the cycle duration can be extended by increasing the charge, or reducing the applied voltage, or reducing the applied current. To clarify this point, Figure 4.18 show two-cell water electrolysis test with different charge of mediator electrodes in chronopotentiometry measurements. In Figure 4.18a, the mediator electrodes were charged to 22.4 mAh, the cycle duration was short (34 min at 40 mA) and the longer cycles of 1.6 hours achieved by charging the mediator electrodes to 63.6 mAh with an applied current of 40 mA as show Figure 4.18b. The average V_{app} of electrolysis cycle is 2.3 V, ending with a

suddenly jump to the threshold limit (± 3.3 V). The sudden jumps at the end of the cycles indicate complete discharge of redox mediator electrodes, which must be recharged to continue the process.

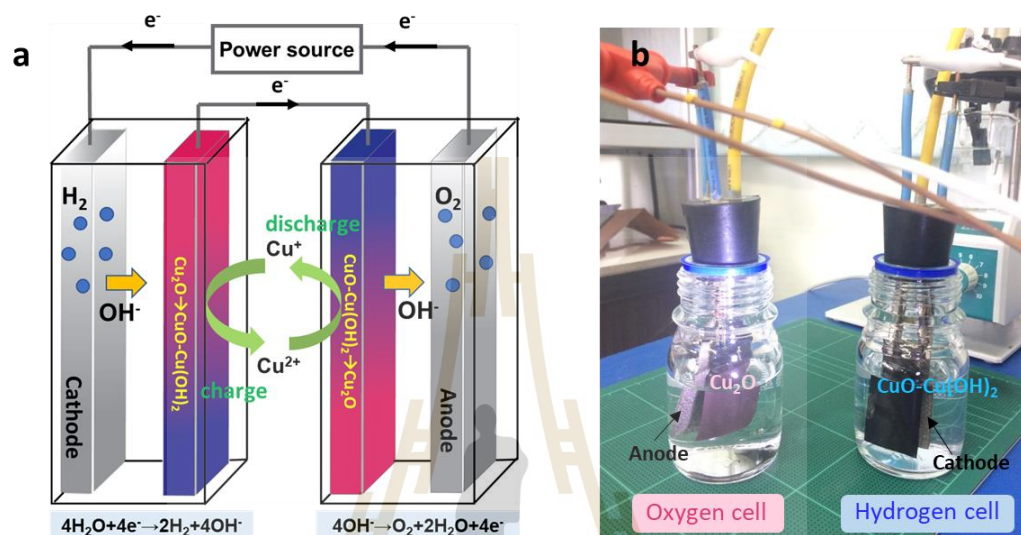


Figure 4.16 Our two-cell water electrolysis system setup. (a) Schematic of two-cell water electrolysis system with $\text{CuO-Cu(OH)}_2/\text{Cu}_2\text{O}$ redox mediator electrodes. (b) The photograph of the Cu_2O and CuO-Cu(OH)_2 redox mediator electrodes after electrolysis at 1.5 hours.

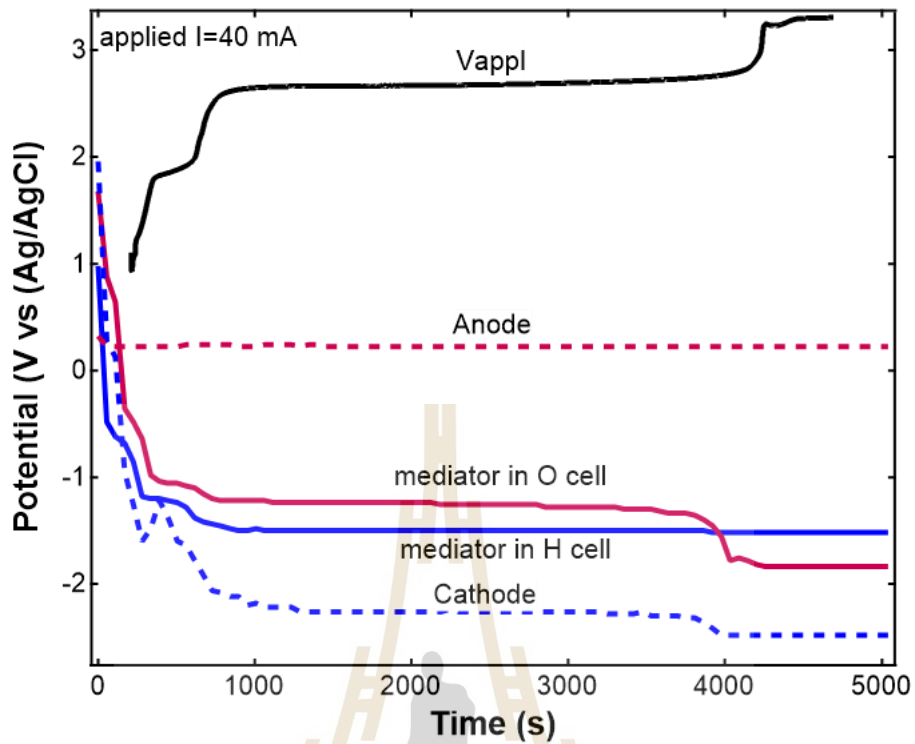


Figure 4.17 The potentials of the electrodes in hydrogen and oxygen cells of two-cell water electrolysis system. The potential of mediator electrodes during electrolysis are shown by blue and pink line curves, respectively.

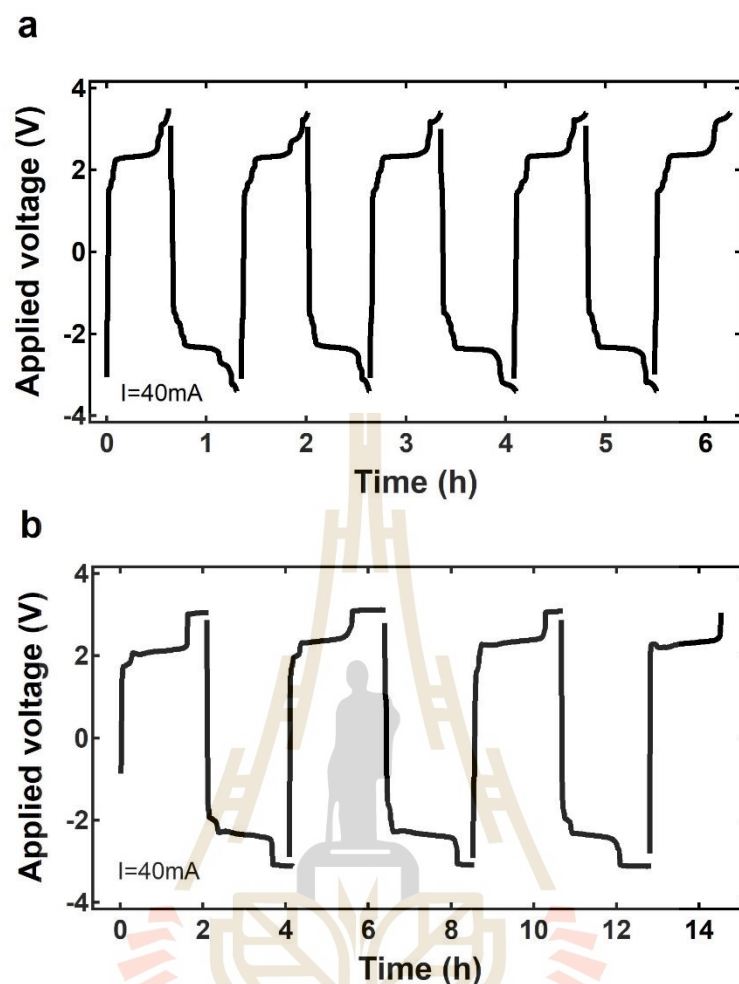


Figure 4.18 Two-cell water electrolysis test with different charge of mediator electrodes. The chronopotentiometry curve (voltage as a function of time) of the electrolysis system at a constant applied current of 40 mA (current density of 4 mA/cm²). (a) The mediator electrodes were charged to 22.4 mAh, the electrolysis cycle was short (34 mins). (b) The longer electrolysis cycle of >1 h achieved by charging the mediator electrodes to 63.6 mAh.

4.3.1 Redox mediator electrode optimization

The CuO-Cu(OH)₂/Cu₂O redox potential is not close to the OER potential, but the actual reversible reaction potential depends on the electrode's SOC (state-of-

charge), composition, and the pH of the solution; therefore parasitic reactions maybe occur. The redox electrode's SOC range and composition can be optimized to enable charging without concurrent oxygen evolution. Similarly, the electrode can be discharged without hydrogen evolution if a full discharge is avoided. These are providing for complete gas separation without co-generation of H₂ and O₂ in the same cell. To select the appropriate SOC operation window, several parameters must be considered: (i) the overall charge, which is calculated based on operating current and the required operation time ($Q = It$); (ii) the extent of the parasitic oxygen evolution reaction (OER) during charging, which increases with state of charge (SOC) and electrode potential; (iii) the extent of the hydrogen evolution reaction (HER) during discharging, which occurs if the electrode is reduced beyond full discharge; and (iv) the stability of the redox mediator electrodes throughout the operation (full charge/discharge should be avoided).

The charging efficiency is measure of the parasitic reaction, so different charge depths of mediator electrode was investigated to estimate the maximum SOC can be reached before parasitic OER (see Figure 4.19). In this experiment, electrochemical profile of a CuO-Cu(OH)₂/Cu₂O redox mediator electrodes (2.5×4 cm², m=48mg) was investigated with different charge depths in two-cell water electrolysis system [Working electrode: CuO-Cu(OH)₂ electrode; Counter electrode: Ni foam (2.5×4 cm²); Reference electrode: Ag/AgCl; Electrolyte: 1M NaOH] as show in Figure 4.19b. To measure the mediator electrode capacity, a redox electrode sample was charged at a current of 40 mA for 2.82 hours to reach the full charge depth, and then discharged at 40 mA to a cutoff potential of -1.3 V (vs. Ag/AgCl). All cycle was performed under dark and solar irradiation. The total electrode capacity under solar irradiation was

estimated at 112.8 mAh (Figure 4.19a). As shown in Figure 4.20, it can be detected that the corresponding discharge time is 2.71 hours (= 96% of charge time), indicating a reversible cycle. When the charge depths are controlled at 90% (2.5 hours), 80% (2.26 hours), 60% (1.7 hours), and 20% (0.55 hours), highly reversible charge/discharge profiles still can be observed clearly. The results shown in Figure 4.20a demonstrate that CuO-Cu(OH)₂ and Cu₂O electrodes can work well at various charge depths.

However, the capacity of electrode is only reached when charging is allowed to continue with concurrent parasitic oxygen evolution (overcharging). The charging efficiency (η_C) is defined as:

$$\eta_C = \frac{Q_{discharge}}{Q_{charge}} = \frac{(It)_{discharge}}{(It)_{charge}} \quad (4.6)$$

where Q_{charge} and $Q_{discharge}$ are the electric charge transferred during the charging and discharging steps, respectively. The charging efficiency is a measure of the parasitic reaction, thus with $\eta_C = 100\%$ no parasitic reactions are occurring. To estimate the maximum obtainable capacity of electrode without overcharging, the electrode was charged at 40 mA to different Q_{charge} values and then discharged at 40 mA to a cutoff potential and the charging efficiency (η_C) of each charging step are show as Figure 4.20b. This result show that the SOC range between 22-88 mAh are no parasitic reactions occur.

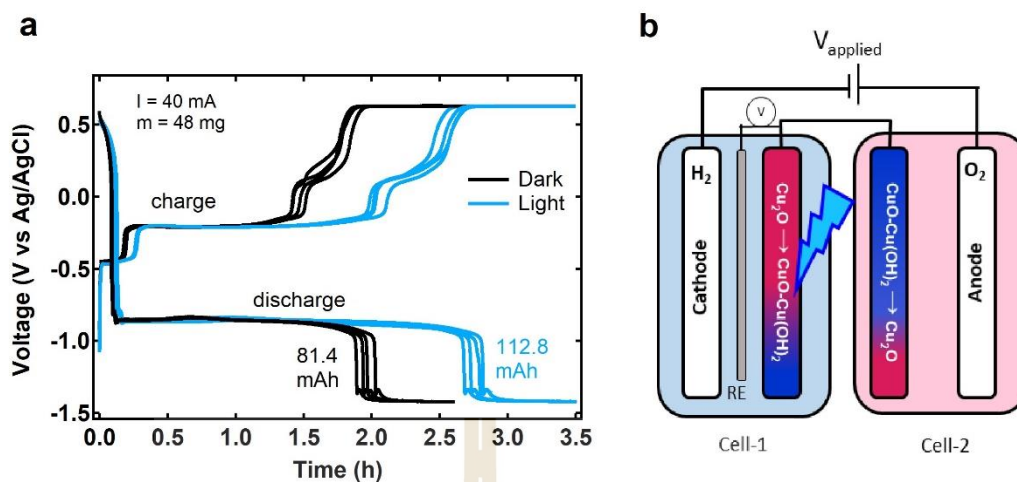


Figure 4.19 (a) Charge and discharge of redox mediator electrode under dark and solar irradiation. A sample was charged at a current of 40 mA for 4 hours to reach the full charge depth, and then discharged at 40 mA to a cutoff potential of -1.3 V (vs. Ag/AgCl). The total electrode capacity was estimated at 112.8 mAh. This experiment was repeated four times at each charge/discharge process. (b) A schematic of the charge depth test setup of the two-cell water electrolysis.

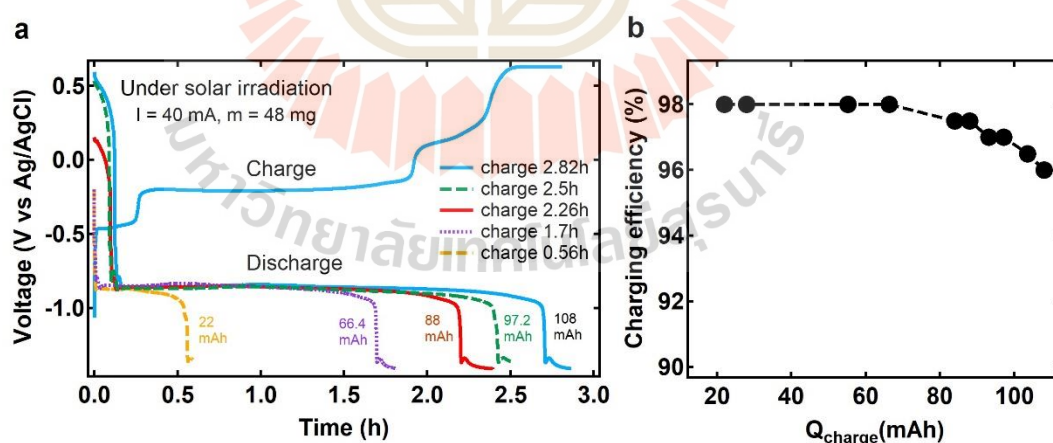


Figure 4.20 (a) Electrochemical profile of CuO-Cu(OH)₂ electrode at different charge depths tested in two-cell water electrolysis at a charge/discharge current of 40 mA. (b) Charging efficiency as a function of the electric charge transferred during charging step.

4.4 Gas measurement and Faradaic efficiency.

Prior to electrolysis operation, the electrolyte was purged with Ar gas for 30 mins. The air and Ar gas were extracted in two-cell water electrolysis system before H₂ and O₂ measurement in several pump-purge cycles. The volume of the effluent gas from the hermetically sealed cells (Figure 4.21a) was measured at several time points during the electrolysis test using a custom-built device for gas volume measurement as shown in Figure 4.21b. The generated gas can be collected in U-tube. The volume of generated gas can be read from the shift of liquid level during the measurement.

The electrolysis efficiency can be examined from the voltage efficiency,

$$\eta_V = \frac{V_{rev}}{V_{app}} = \frac{1.23}{2.3} = 54\% \quad (4.7)$$

where $V_{rev} = 1.23$ V is the reversible voltage of water electrolysis (25°C).

In order to calculate the Faradaic efficiency (η_F), the volume of gases from a hydrogen and oxygen cells were compared with the charge that was transferred between the Ni foam primary electrodes during that time, $Q = \int Idt$. The Faradaic efficiency for the product gas (oxygen or hydrogen) generation was calculated according to the following equation (Landman et al., 2017):

$$\eta_F = \frac{n(gas)_{measured}}{n(gas)_{calculated}} = \frac{PV(gas)_{measured}/RT}{Q/zF} \quad (4.8)$$

wherein P is the pressure (1 atm), V the volume of the effluent gas, R the gas constant, T the temperature (298 K), $Q = \int Idt$ the charges, z the stoichiometric charge number (2 electrons per H₂ molecule and 4 electrons per O₂ molecule) and F the Faraday constant. Considering measurement errors such as spurious gas leaks, gas volume and pressure measurement errors, the Faradaic efficiency for hydrogen and oxygen evolution was approximately 95% (95%±2% and 95%±4%, respectively).

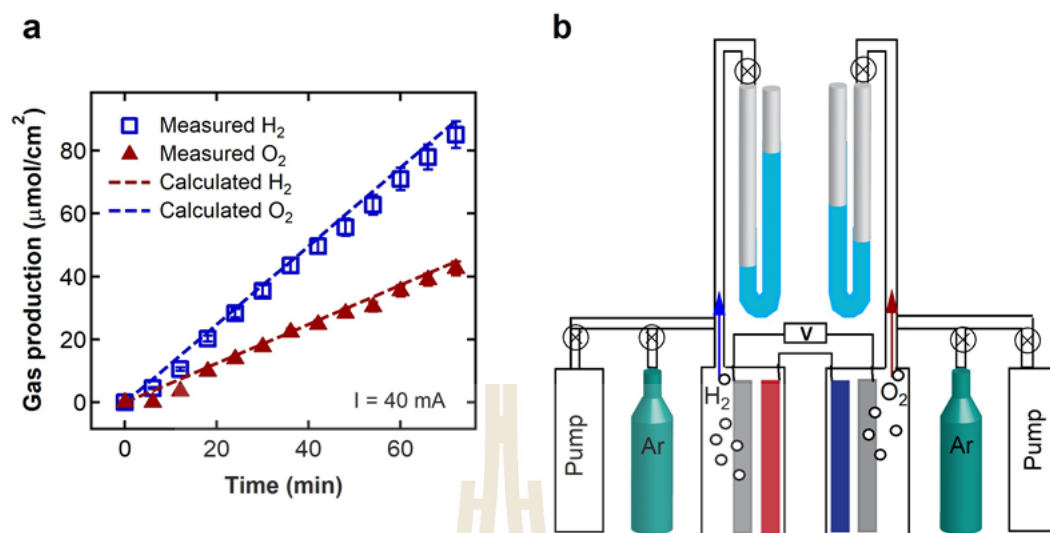


Figure 4.21 (a) The volume of effluent gas produced at the headspace of the oxygen and hydrogen cells (blue squares and brown triangle) as a function of time during a two-cell water electrolysis test at a constant current of 40 mA (current density of 4 mA/cm^2). The blue and brown lines show the theoretical volume of the respective gases, calculated based on the current \times time product assuming Faradaic efficiency of 100%. (b) Schematic illustration of a typical custom-built devices for gas volume measurement.

4.5 *In-situ* gas chromatography

The *in-situ* GC measurement was performed with the applied the constant voltage of 3 V to investigate the gases production and the mixing of gas in two-cell water electrolysis system. The purity of H_2 and O_2 which shown in chromatograms Figure 4.22a and Figure 4.22b were obtained from the experiment at room temperature. The composition of the evolved gas was analyzed by subtracting the background gas

composition of the blank measurements from the measurements that were carried out during operation. From these results can be confirmed that no H₂/O₂ crossover.

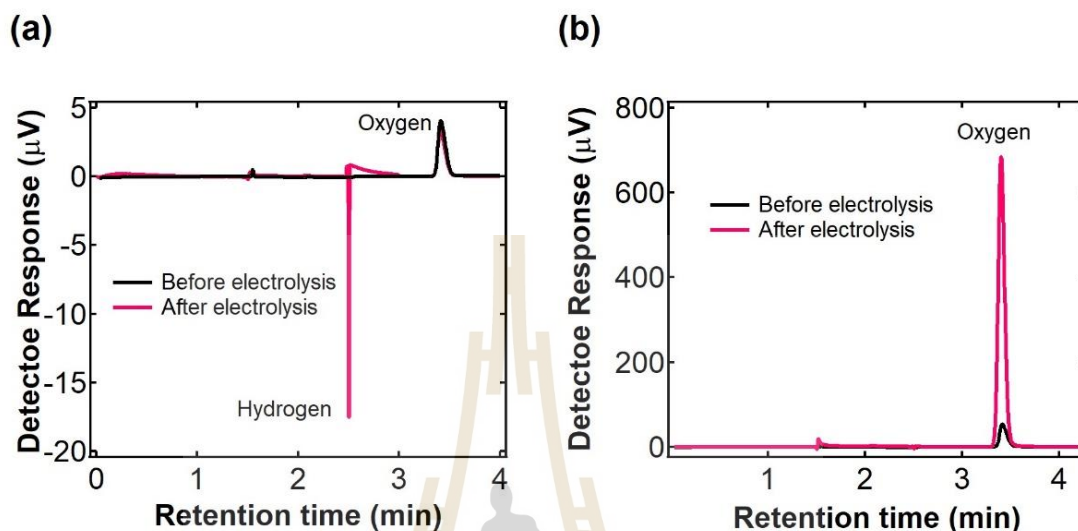


Figure 4.22 *In situ* purity measurement of H₂ and O₂. (a) Chromatogram of outlet gas taken from the headspace of the hydrogen cell and (b) the oxygen cell.

4.6 Gases production of two-cell water electrolysis under dark and light illumination

4.6.1 Chronoamperometry measurement (V constant)

To start the electrolysis process, a constant voltage (2.0, 2.5 and 3.0 V) was applied across the device for 20 minutes and 1 hour. Bubbles indicated the evolution of gaseous H₂ and O₂ at the cathode and anode (active area 10 cm²), respectively, while there are no bubbles forming at the mediator electrodes (active area 10 cm²). The volume of gas evolved as a function of time at V = 2 V is shown in Figure 4.23. The initial rates during the first 15 mins are 169.2 and 85.4 μmol h⁻¹cm⁻² (averaged rates of HER and OER are 93.1 and 46.9 μmol h⁻¹cm⁻²); the H₂-to-O₂ ratio is approximately 2:1

in the consecutive cycles similar to the previous studies (Goodwin and Walsh, 2017; Landman et al., 2017). Then, after approximately 1.5 hours, the mediator electrode pair was fully charged/discharged. Subsequent electrolysis could then be resumed by switching the applied voltage between the anode and cathode. Correlation of the quantity of gas produced with the charge passed during electrolysis showed good Faradaic efficiency of approximately 95% (Figure 4.21) and average electrolysis efficiency ($\eta_V = V_{rev}/V_{app}$) 54% (Equation 4.7), comparable to the Ni(OH)₂/NiOOH mediator pair studied in Ref. [(Chen et al., 2016; Landman et al., 2017)]. Deviation of the measured Faradaic efficiency from a theoretically achievable 100% yield is most likely due to a combination of gas leakage and dissolution of H₂ in the aqueous solution.

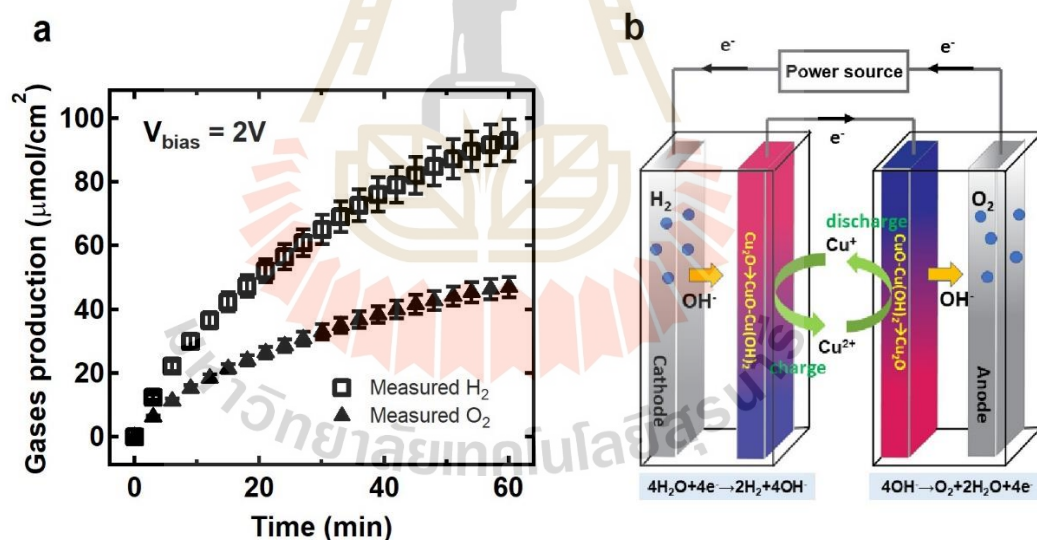


Figure 4.23 (a) H₂ and O₂ production that evolved during operation at a potential bias of 2 V in two-cell water electrolysis which was setup according to the schematic diagram in (b).

Interestingly, solar irradiation (AM 1.5G illumination at 80 mW/cm²) of the mediator electrodes during the charge and discharge processes led to an increase in the

evolution rate of both H₂ and O₂ gases. As shown in Figure 4.24a and 4.24b, H₂ and O₂ were evolved at 128.5 and 65.9 μmol h⁻¹cm⁻², representing an increase of approximately 40%, while initial evolution rates of 15 mins increase up to 45% (from 169.2 μmol h⁻¹cm⁻² in the dark to 244.5 μmol h⁻¹cm⁻² under irradiation). This reflects a corresponding increase in the charge transfer ($Q = \int I dt$) between anode and cathode (see Figure 4.24c), rising from 50 mAh in the absence of irradiation to 71 mAh under solar irradiation. The effect of solar irradiation was also studied by testing the two-cell water electrolysis under light on-off conditions. As shown in Figure 4.24c and inset, additional current density was observed when the CuO-Cu(OH)₂ and Cu₂O redox electrodes were operated under solar irradiation. This confirms that the presence of sunlight improves the yield of H₂ production.

The results as shown in Figure 4.25, the purpose for using constant applied voltage with short cycle duration is to emphasize that our electrolysis system can provide high H₂ production rate within very short time, which is quite difficult for conventional alkaline water electrolytic cells.

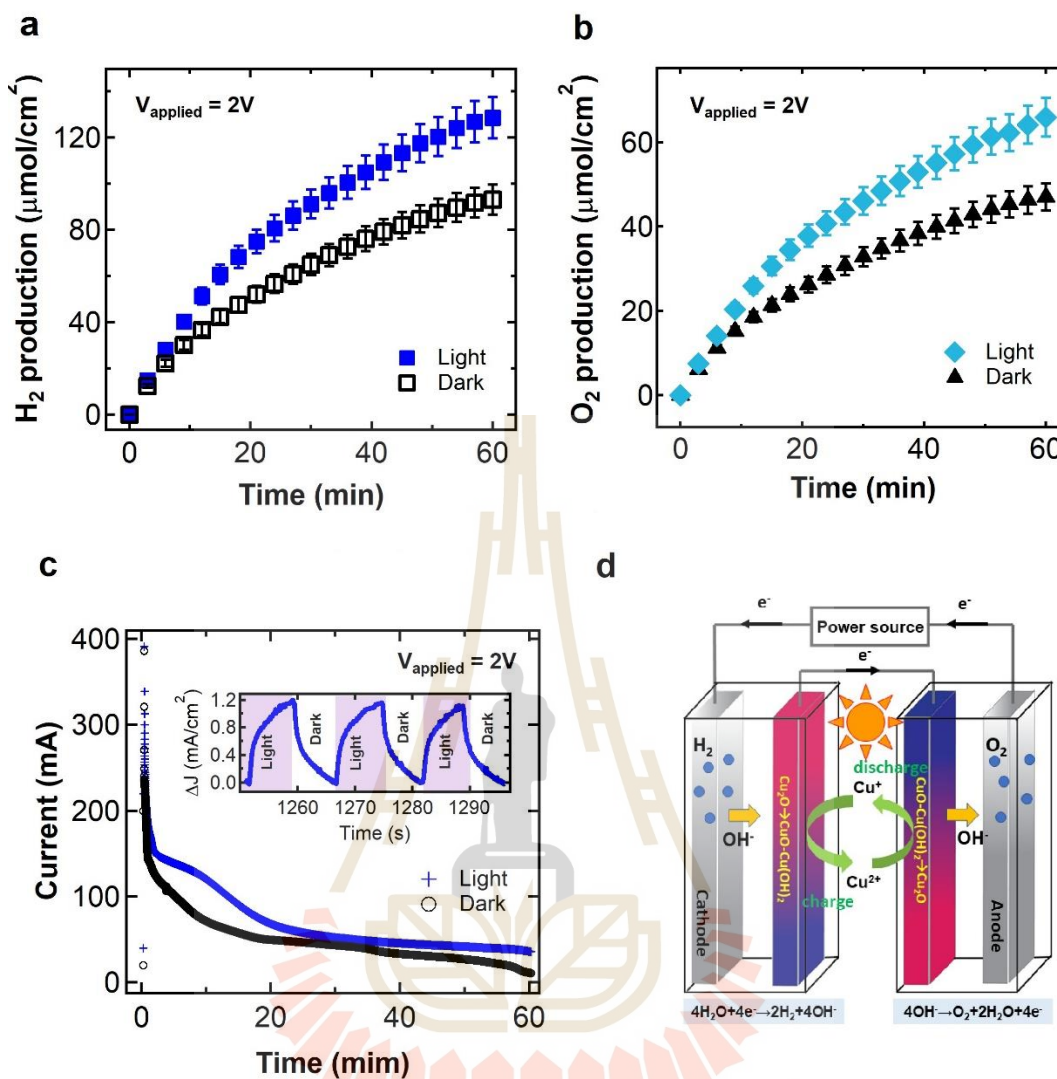


Figure 4.24 Effect of sunlight on CuO-Cu(OH)₂/Cu₂O redox mediator electrode. (a) and (b) show H₂ and O₂ production in two-cell water electrolysis system operated at a potential application of 2 V under dark and sunlight illumination. (c) Current density of two-cell water electrolysis system under sunlight conditions. The inset shows the additional current density depending on light on/off. (d) The schematic of two-cell water electrolysis operation under solar irradiation.

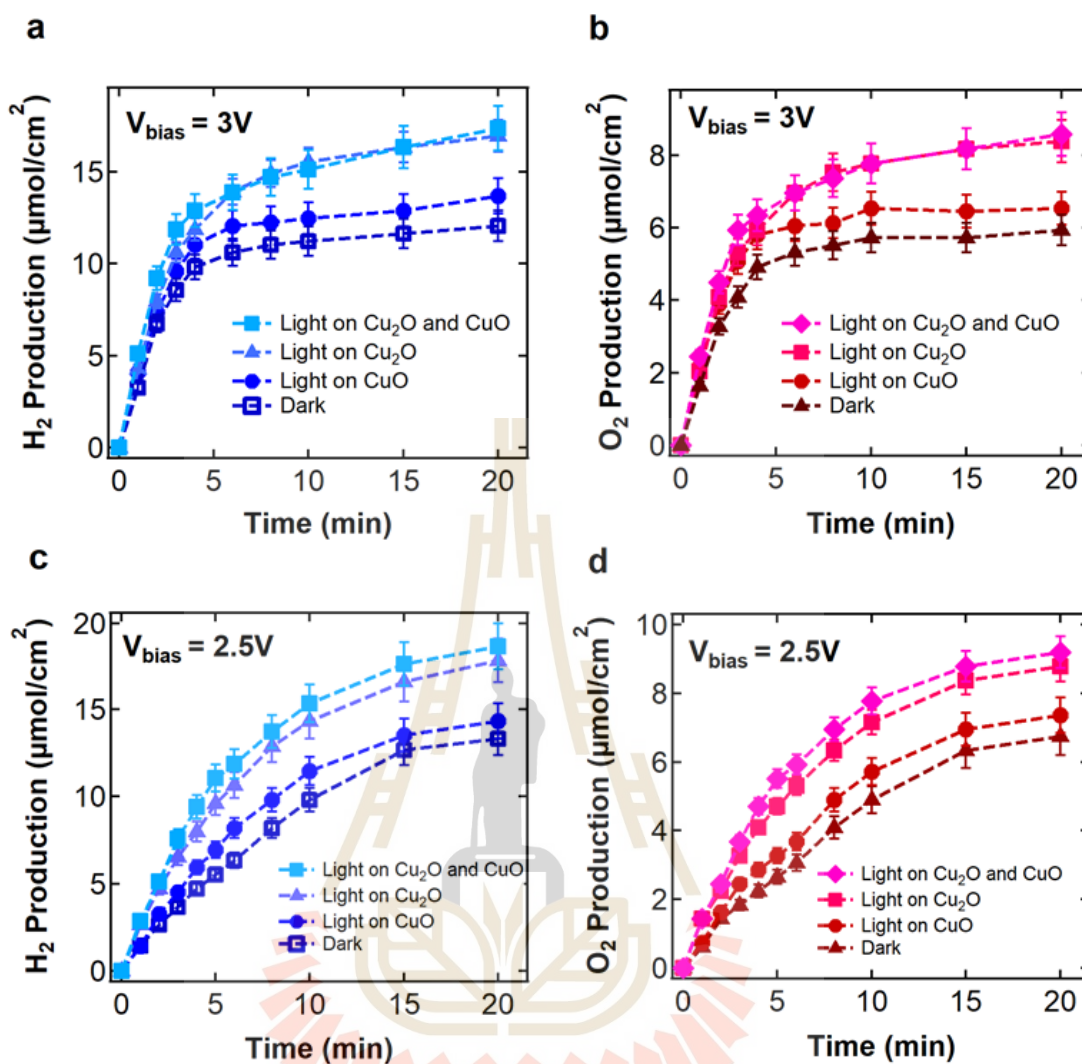


Figure 4.25 The amount of gases from the sealed cells of two-cell water electrolysis system with light irradiated on different mediator electrode. (a) and (b) The amount of H_2 and O_2 , respectively, during electrolysis at $V=3$ V. (c) and (d) The amount of H_2 and O_2 , respectively, during electrolysis at $V=2.5$ V.

4.6.2 chronopotentiometry measurements (I constant)

The operation by using constant applied current is also measured, which is show in Figure 4.26 to easily compare this electrolysis system with other works in the field. Figure 4.26 show applied voltage as a function of time during operated at a constant

current of 40 mA. From this result clearly that our electrolysis system required lower applied voltage and longer cycle duration with gases production increased 30% when operated under solar irradiation on mediator electrodes.

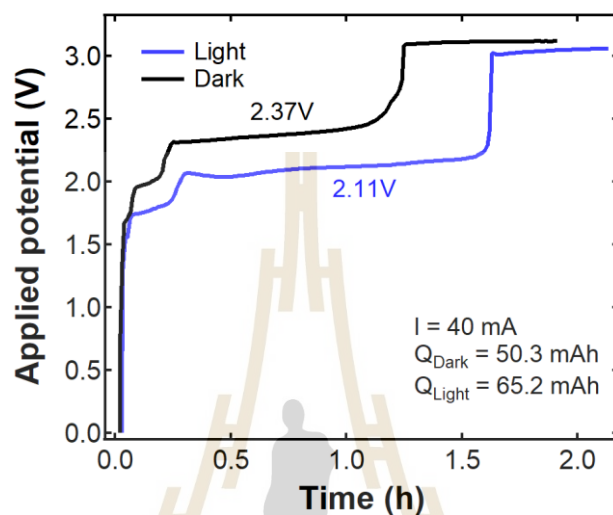


Figure 4.26 The applied potential as a function of time during operated two-cell water electrolysis system at a constant current of 40 mA (2 mA/cm^2) under dark and solar irradiation.

4.7 *In-situ* X-ray absorption spectroscopy (XAS)

The changing oxidation states in the $\text{CuO-Cu(OH)}_2/\text{Cu}_2\text{O}$ mediator electrode were tracked using *in-situ* X-ray Absorption Spectroscopy (XAS) during charging and discharging in the presence and absence of solar irradiation. Figure 4.27a and 4.27b show the resulting normalized Cu K-edge XANES spectra and the changes in the edge positions in the $\text{CuO-Cu(OH)}_2/\text{Cu}_2\text{O}$ mediator electrode, which was tracked during the electrolysis. The position of the absorption edge contains information on the electronic structure of Cu within the electrode. During the charging process of Cu_2O in the hydrogen cell, XANES spectra showed a clear shift to higher energy states (see blue

dash lines in the Figure 4.27a). This indicates a change in the Cu oxidation state from +1.15 to +1.43 during electrolysis at 3 V for 30 minutes. A shift of the XANES spectra in the opposite direction (see red lines in the Figure 4.27a) was observed during the discharging process of CuO-Cu(OH)₂ in the oxygen cell. The oxidation state of Cu reduced back to +1.16, which is near to the initial oxidation state (+1.15). These observations indicate the reversibility of redox in of CuO-Cu(OH)₂/Cu₂O mediator electrodes. The changes in oxidation state during the charge and discharge processes are similar to other transition metal oxides in previous reports (Pongha et al., 2015; Xuning et al., 2018). Interestingly, under light irradiation at 3 V on the mediator electrode during the charging process in the electrolysis system, the XANES Cu K-edge energy significantly shifts according to oxidation of the +1.16 to +1.52 (see blue spectra in Figure 4.27a and 4.27b). During the discharge process of the mediator electrode, a lower energy edge upon light irradiation (see red spectra in Figure 4.27a and 4.27b) indicated an increased amount of Cu⁺, with the average oxidation number changing from +1.52 to +1.12. This change of oxidation state is consistent with our CV measurements.

The Fourier transform of Cu K-edge EXAFS spectra of Cu₂O and CuO-Cu(OH)₂ during electrolysis under dark and light conditions provides coordination information from the radial distribution function (RDF), which is shown in Figure 4.28a and 4.28b, respectively. The first peak at about 1.45 Å corresponds to the nearest neighbor to Cu, and therefore originates from Cu-O bonds. The peak at 2.24 Å matches well with Cu-Cu bonds in the Cu-foil substrate, which is consistent with previous reports (Aregahegn et al., 2015; Dubale et al., 2015).

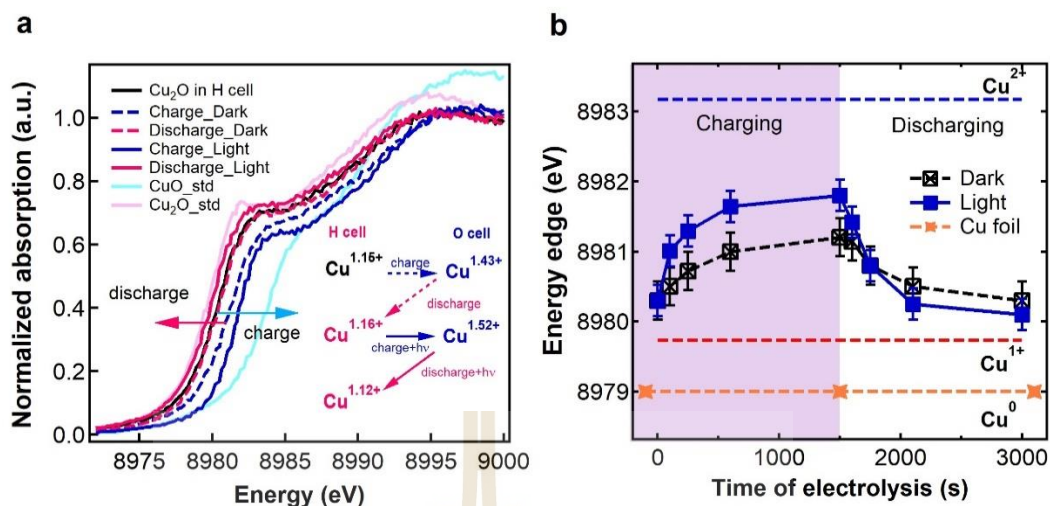


Figure 4.27 Electronic structure of CuO-Cu(OH)₂/Cu₂O redox mediator electrode. (a) In situ Cu K-edge fluorescence XANES spectra of mediator electrode during charging and discharging under dark and light illuminations in two-cell water electrolysis at 3 V. The changing of oxidation state for each condition is shown in the inset. (b) Changing absorption edge positions and of redox mediator electrodes during charging and discharging under dark and light illumination.

During the charging process (i.e. during electrolysis) under light irradiation, the radial distribution function obtained from EXAFS of the Cu₂O electrode showed a slight decrease in Cu-O bond length compared with the same measurement performed under dark conditions. This effect can be seen in Figure 4.28a, and corresponds to a significant change in the Cu-O coordination number resulting from fewer oxygen atoms as nearest neighbours. However, this effect was not observed in the case of CuO-Cu(OH)₂ electrode (see Figure 4.28b).

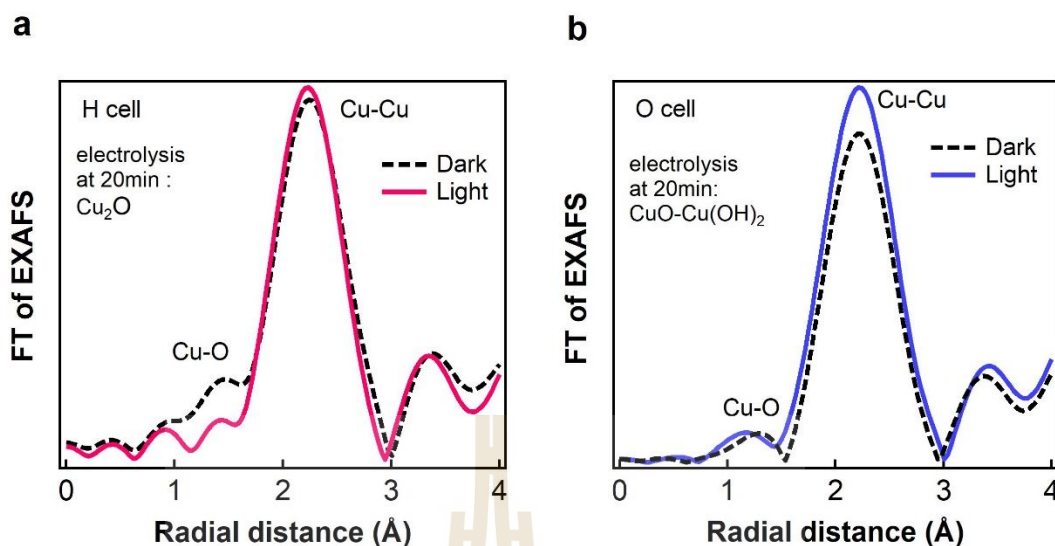


Figure 4.28 FT EXAFS structures of redox mediator electrodes during charging (a) and discharging (b) under dark and light illumination.

4.8 Photoemission spectroscopy analysis.

By using photoemission spectroscopy (PES), the electronic structure of the mediator electrode under illumination was also measured, which helps to elucidate the reaction mechanism at the electrodes during electrolysis (see Figure 4.29a and 4.29b). Figure 4.29a shows the valence band spectra of the Cu_2O mediator electrode with different carrier-dopants. It is clear that the valence band maximum is slightly shifted toward the Fermi level and the ratio of the Cu3d state (1.5-4 eV) to the O2p state (4-8 eV) (Wang et al., 2016) increases with increased carrier doping. This suggests a surface electron accumulation. It also indicates that electrons can be transferred from Cu_2O in the hydrogen cell to CuO-Cu(OH)_2 in the oxygen cell. This is consistent with the increase of current density in the CV curve and XAS results.

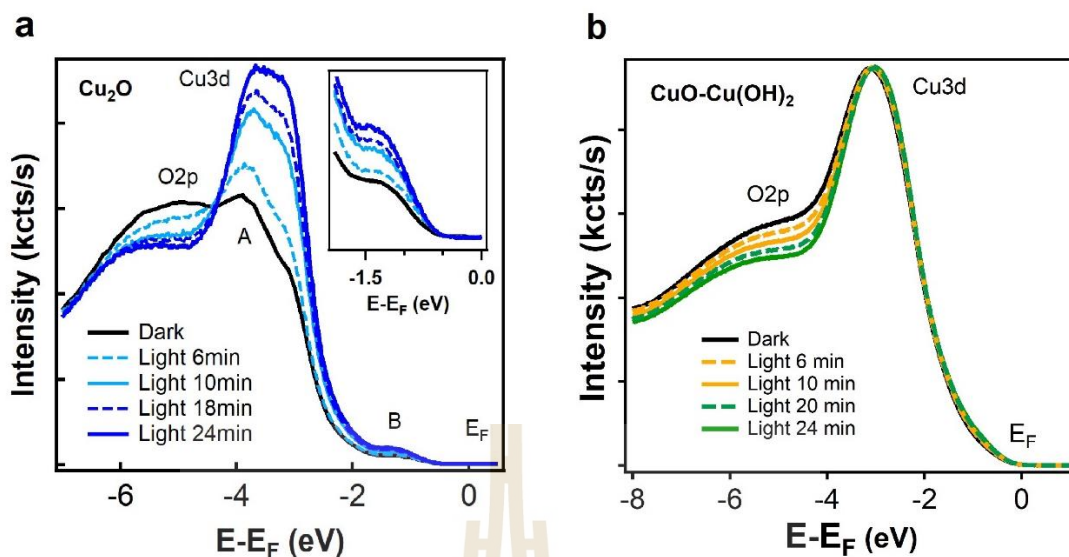


Figure 4.29 Electronic structure of the redox mediator electrode. (a) and (b) Evolution of the valence band (VB) spectra of Cu_2O and CuO-Cu(OH)_2 redox mediator electrode from the pristine fractured surface to the light irradiated surface, respectively. The inset in (a) shows the evolution of the in-gap state with increasing exposure time.

The change of surface chemical bonding of CuO-Cu(OH)_2 and Cu_2O before and under illumination was investigated with x-ray photoelectron spectroscopy (XPS). The O1s and Cu3s3p XPS spectra of electrodes shift to a lower binding energy (Figure 4.30), which are contributed to the formation of neighboring oxygen vacancies.

In contrast, the C1s state was also measured immediately after each UV irradiation ($h\nu = 500$ eV) which clearly indicates no binding energy shift of C1s state (Figure 4.30a and 4.30f) confirming the distinctive character of CuO sample.

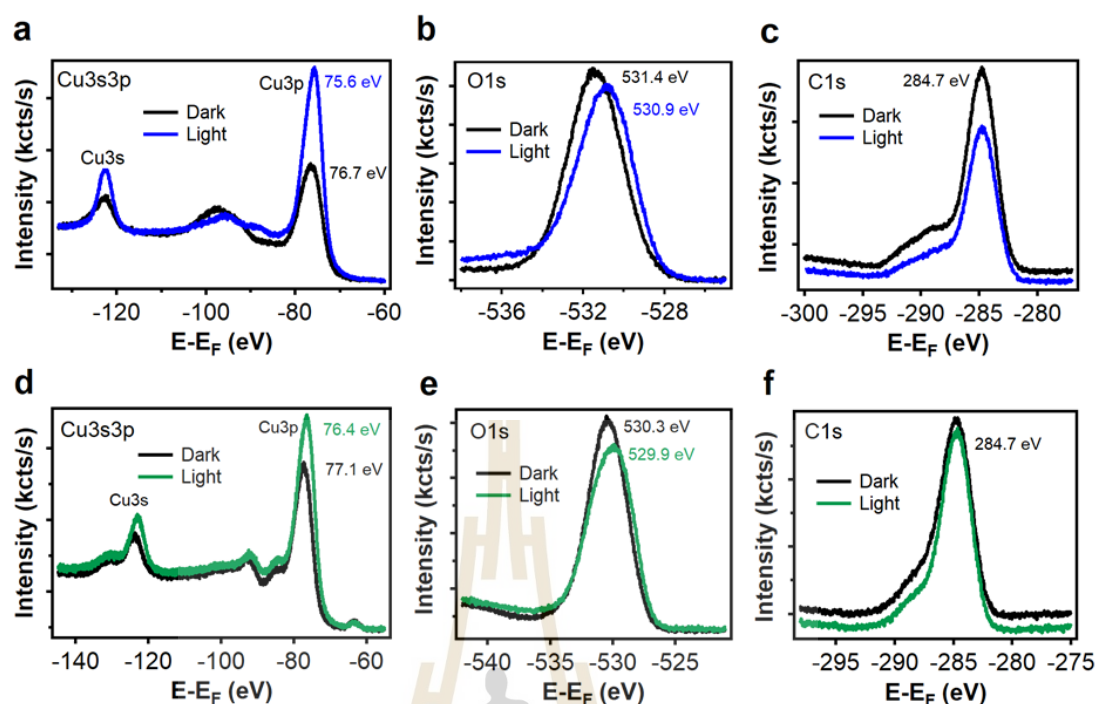


Figure 4.30 XPS spectra of mediator electrodes measured under dark and light condition. (a), (b) and (c) Cu3s3p, O1s and C1s, respectively, of Cu₂O electrode. (d), (e) and (f) Cu3s3p, O1s and C1s, respectively, of CuO-Cu(OH)₂ electrode.

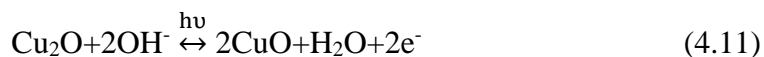
4.9 Discussion

In a two-cell water electrolysis system, the CuO-Cu(OH)₂ and Cu₂O present both pseudo-capacitive and photo-sensitive behavior with high specific capacitance and excellent cycling stability. The integration of photo-supercapacitive behavior with a mediator system in a single electrode offers important advantages. Specifically, the rate of evolution of H₂ and O₂ gases is significantly increased during sunlight irradiation onto the mediator electrodes. This is because the sunlight has an important influence on the pseudo-capacitance behavior (Figure 4.10 and 4.13). The solar power can be captured and directly stored chemically in redox mediator electrodes.

Under light irradiation, the charge in the electrolysis system was increased by 42% compared to that under dark conditions. In turn, the initial H₂ and O₂ evolution rates were significantly enhanced up to 45%. However, this effect depends strongly on which electrode is irradiated, as shown in the Figure 4.20. Irradiation of either the Cu₂O electrode alone or both electrodes at once produces similar increase in gas evolution. On the other hand, when only the CuO-Cu(OH)₂ electrode in the oxygen cell is irradiated, there is a much weaker increase in the rate of gas evolution. This is because the conduction band minimum (CBM) of Cu₂O is higher in energy than the CBM of CuO (Dubale et al., 2015; Yang et al., 2016b). Therefore, during the charge/discharge process, photogenerated electrons can easily transfer from Cu₂O to CuO but not the other way around.

The redox mechanism of the Cu₂O and CuO-Cu(OH)₂ mediator electrode pair during the charging/discharging process under light illumination in two-cell electrolysis involves a photo-assisted charging mechanism of electrodes. During the charging process in the hydrogen cell, the valence electrons of Cu₂O are excited to the conduction band under light illumination, resulting in the generation of electron-hole pairs (Equation 4.9). The holes accumulate at the Cu_xO/water interface and oxidize Cu₂O into CuO (Equation 4.10) (Aguirre et al., 2017; An et al., 2019; Huang et al., 2009; Kakuta and Abe, 2009; Saratale et al., 2018; Toe et al., 2018; Zheng et al., 2009). Simultaneously, the photo-generated electrons pass through the external circuit (Dias et al., 2015) to reduce the CuO-Cu(OH)₂ electrode in the oxygen cell. During the discharge process in the oxygen cell, CuO-Cu(OH)₂ can be reduced back to Cu₂O by following a reversible redox reaction process (Equation 4.11).

The redox mechanism under light irradiation is as follows (An et al., 2019; Huang et al., 2009; Toe et al., 2018)



More importantly, during light illumination, the photogenerated holes with oxidation reacts with mediator electrodes. This promotes the utilization of the electrode materials and further enhances the specific capacitance.

In-situ Cu K-edge XANES was used to study the local electronic structure of redox mediator electrodes during electrolysis at a constant system voltage of 3 V. Upon light irradiation of the Cu₂O mediator electrode in the hydrogen cell, a larger shift of the Cu K-edge energy (Figure 4.27) during charging indicated a greater positive shift in the oxidation state of Cu compared with the same experiment performed in the absence of light. This suggests that the photogenerated holes (van Oversteeg et al., 2017; Yoshida et al., 2014) in the Cu₂O electrode assisted the oxidation of Cu₂O to CuO-Cu(OH)₂. On the other hand, the reduction of the Cu oxidation state in CuO-Cu(OH)₂ during the discharging process under irradiation suggests the migration of electrons from the Cu₂O electrode to the CuO-Cu(OH)₂ electrode. These electrons consequently reduced CuO-Cu(OH)₂ to Cu₂O. The reduction was more pronounced under light irradiation due to the difference in charge storage between dark and light conditions. These results confirm the photo-assist charging of the mediator electrodes during water electrolysis, which is in good agreement with electrochemical results.

The Fourier transforms of Cu K-edge EXAFS spectra (shown in Figure 4.28) of Cu₂O during electrolysis under dark and light conditions were also studied to support

the observations made from XANES. Interestingly, the only significant change in these arose from shifts in the Cu-O bond peak. A lower coordination number of Cu-O bonds under irradiation is indicated, suggesting that oxygen vacancies (Xiao et al., 2017; Zhang et al., 2019) are created in the Cu₂O electrode during electrolysis under light irradiation.

Electronic change local to the surface of the redox mediator electrodes, were also tracked by taking valence band photoemission spectra of Cu₂O and CuO-Cu(OH)₂ during irradiation (Figure 4.29). As exposure time increased, the O2p state decreases and its leading edge shifts slightly toward Fermi level. It is accompanied by an increase in the intensity of the sub-gap state peak around 1.3 eV (inset in Figure 4.29a). Looking at previous studies, we consider that this sub-gap defect state is most likely associated with oxygen vacancies at the surface (Masingboon et al., 2013; Meevasana et al., 2011a; Nathabumroong et al., 2020; Singh et al., 2018; Suwanwong et al., 2015). The surface oxygen vacancies on Cu₂O electrodes play an important role in the separation of photogenerated electron-hole pairs and in the improvement of redox behavior involving photocapacitive performance (Khan et al., 2017; Liu et al., 2017; Liu et al., 2018; Lu et al., 2018; Lv et al., 2016; Nathabumroong et al., 2020; Singh et al., 2018; Zhao et al., 2019). When Cu₂O is irradiated by light greater than its optical bandgap (valence band maximum (VBM) shift to EF), electron-hole pairs are generated (Equation 4.9). Then, the photogenerated electrons are trapped by surface oxygen vacancies (peak at 1.3eV) (Khan et al., 2017; Liu et al., 2018; Yan et al., 2019). These charges captured momentarily by surface oxygen vacancies are then readily transmitted to the Cu substrate (Cheng et al., 2016; Liu et al., 2018) (see schematic Figure 4.31). Meanwhile, the photogenerated holes act to oxidize Cu₂O to CuO and H₂O as in Equation 4.10. Our

spectroscopic observations are consistent with the capacitive improvement of the mediator electrodes under solar irradiation as demonstrated in the CV curve. Importantly, oxygen vacancies enhance the electrical conductivity of transition metal oxides (Lu et al., 2018; Suwanwong et al., 2015) as a mediator electrode. The electron-hole pairs can be efficiently separated (inset in Figure 4.24c), resulting in higher gas evolution rates compared to that in the absence of light.

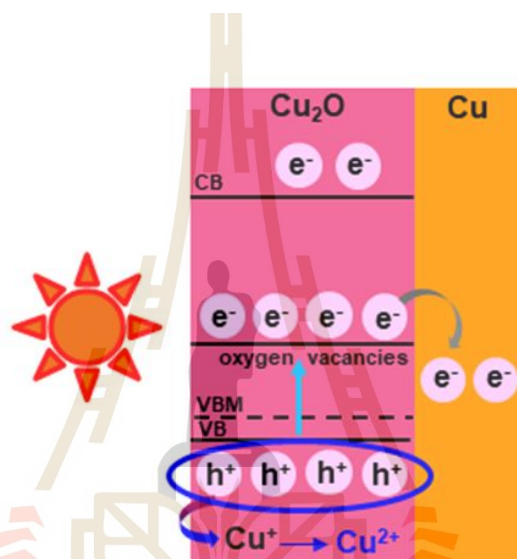


Figure 4.31 Schematic diagram illustrating the proposed mechanism of charge separation and photooxidation of Cu₂O to CuO.

CHAPTER V

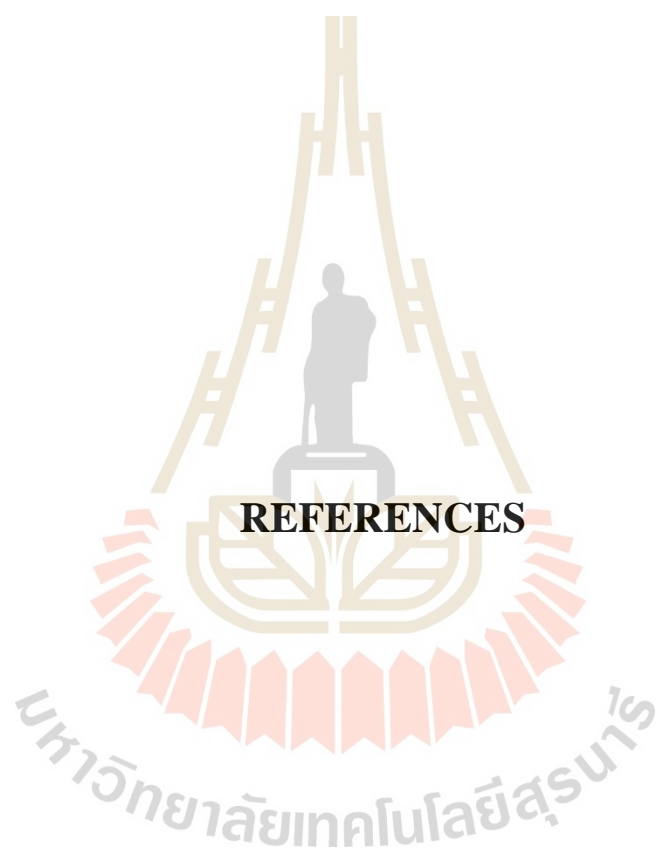
CONCLUSIONS

The conventional alkaline electrolysis was successfully split into two cells using CuO-Cu(OH)₂/Cu₂O as a recyclable redox mediator. The separate H₂ and O₂ production overcomes the challenge of H₂/O₂ mixing and facilitates the operation of alkaline electrolysis even with unstable power inputs. Furthermore, two-cell electrolysis can be carried out repeatedly through cycling the mediator electrodes by switching the applied voltage. Therefore, our proposed system can be continuous operation due to the excellent cycling durability of the CuO-Cu(OH)₂/Cu₂O mediator electrodes, which can be cycled thousands of times (or maybe more).

A two-cell electrolytic water splitting system has been developed with electrodes acting as both a redox mediator and as a photo-supercapacitor for improved H₂ and O₂ gas production. The solar-driven pseudocapacitive behavior on CuO-Cu(OH)₂/Cu₂O mediator electrode pair exhibits an increase in the specific capacitance compared with that in the absence of light (36%). This implies direct storage of solar energy which provided an increase of the initial H₂ and O₂ production rates by 45%. Our observations indicate that as a Cu₂O electrode is irradiated with solar light in a hydrogen cell, surface-localized oxygen vacancies are created. These play an important role in the separation of photogenerated electron-hole pairs, providing an improvement of redox behavior and capacitive activity in our two-cell water electrolysis system

Regarding its application, this work provides new strategy of combining a two-cell water electrolysis system with photo-supercapacitor in one device which is a route to low-cost and sustainable hydrogen production. Firstly, the two-cell system requires no expensive protonexchange membranes (PEM) commonly used in water electrolysis systems. Furthermore, in our system, the free solar irradiation could boost the performance of H₂ production by 45% and effectively increase the energy storage capacity of the mediator electrode. The effective increase in this solar-enhanced capacity is important for the cost optimization since the effective cost of energy storage is usually many folds of the solar cell panels proposed as the clean electricity generator for the H₂ production system.

Future efforts should focus on (i) fabricating a prototype standalone solar water splitting and optimizing the redox electrode composition, cell architecture, and cycling process to improve the performance and reduce the capital and operating costs of solar water splitting plants, (ii) carry out to study new redox electrode materials and using advanced analytical methods to understand the correlations between electrode composition and microstructure, its functional properties, in order to develop the next generation of redox-based electrodes for two-cell water splitting process, (iii) improve their capacity (so that it can run longer processes) with fast charging and generation rates to enable high hydrogen production rates.



REFERENCES

REFERENCES

- Aguirre, M. E., Zhou, R., Eugene, A. J., Guzman, M. I. and Grela, M. A. (2017). Cu₂O/TiO₂ heterostructures for CO₂ reduction through a direct Z-scheme: Protecting Cu₂O from photocorrosion. **Applied Catalysis B: Environmental**. 217: 485-493.
- An, C., Wang, Z., Xi, W., Wang, K., Liu, X. and Ding, Y. (2019). Nanoporous Cu@Cu₂O hybrid arrays enable photo-assisted supercapacitor with enhanced capacities. **Journal of Materials Chemistry A**. 7(26): 15691-15697.
- Aricò, A. S., Bruce, P., Scrosati, B., Tarascon, J. M. and van Schalkwijk, W. (2005). Nanostructured materials for advanced energy conversion and storage devices. **Nature Materials**. 4(5): 366-377.
- Armaroli, N. and Balzani, V. (2011). The Hydrogen Issue. **ChemSusChem**. 4(1): 21-36.
- Beer, A. (1852). Bestimmung der Absorption des rothen Lichts in farbigen Flussigkeiten. **Ann. Physik**. 162: 78-88.
- Benigna, J. (2014). Photoelectron Spectroscopy in Advanced Placement Chemistry. **Journal of Chemical Education**. 91(9): 1299-1305.
- Bloor, L. G., Solaraska, R., Bienkowski, K., Kulesza, P. J., Augustynski, J., Symes, M. D. and Cronin, L. (2016). Solar-Driven Water Oxidation and Decoupled Hydrogen Production Mediated by an Electron-Coupled-Proton Buffer. **Journal of the American Chemical Society**. 138(21): 6707-6710.

- Bressler, C. and Chergui, M. (2004). Ultrafast X-ray Absorption Spectroscopy. **Chemical Reviews**. 104(4): 1781-1812.
- Chen, L., Dong, X., Wang, Y. and Xia, Y. (2016). Separating hydrogen and oxygen evolution in alkaline water electrolysis using nickel hydroxide. **Nature Communications**. 7: 1174.
- Cheng, Y., Lin, Y., Xu, J., He, J., Wang, T., Yu, G., Shao, D., Wang, W. H., Lu, F., Li, L., Du, X., Wang, W., Liu, H. and Zheng, R. (2016). Surface plasmon resonance enhanced visible-light-driven photocatalytic activity in Cu nanoparticles covered Cu₂O microspheres for degrading organic pollutants. **Applied Surface Science**. 366: 120-128.
- Chergui, M. (2014). Introductory Lecture: Emerging photon technologies for chemical dynamics. **Faraday Discuss**. 171.
- Choi, N. S., Chen, Z., Freunberger, S. A., Ji, X., Sun, Y. K., Amine, K., Yushin, G., Nazar, L. F., Cho, J. and Bruce, P. G. (2012). Challenges facing lithium batteries and electrical double-layer capacitors. **Angew Chem Int Ed Engl**. 51(40): 9994-10024.
- Dias, P., Schreier, M., Tilley, S. D., Luo, J., Azevedo, J., Andrade, L., Bi, D., Hagfeldt, A., Mendes, A., Grätzel, M. and Mayer, M. T. (2015). Transparent Cuprous Oxide Photocathode Enabling a Stacked Tandem Cell for Unbiased Water Splitting. **Advanced Energy Materials**. 5(24): 1501537.
- Dotan, H., Landman, A., Sheehan, S. W., Malviya, K. D., Shter, G. E., Grave, D. A., Arzi, Z., Yehudai, N., Halabi, M., Gal, N., Hadari, N., Cohen, C., Rothschild, A. and Grader, G. S. (2019). Decoupled hydrogen and oxygen evolution by a

two-step electrochemical–chemical cycle for efficient overall water splitting. **Nature Energy**. 4(9): 786-795.

Dubale, A. A., Pan, C. J., Tamirat, A. G., Chen, H. M., Su, W. N., Chen, C. H., Rick, J., Ayele, D. W., Aragaw, B. A., Lee, J. F., Yang, Y. W. and Hwang, B. J. (2015). Heterostructured Cu₂O/CuO decorated with nickel as a highly efficient photocathode for photoelectrochemical water reduction. **Journal of Materials Chemistry A**. 3(23): 12482-12499.

Dunn, B., Kamath, H. and Tarascon, J. M. (2011). Electrical Energy Storage for the Grid: A Battery of Choices. **Science**. 334(6058): 928.

Elzwawi, S. (2015). **Cathodic Arc Zinc Oxide for Active Electronic Devices**. Ph.D. Dissertation, University of Canterbury, New Zealand.

Giorgetti, M. (2013). A Review on the Structural Studies of Batteries and Host Materials by X-Ray Absorption Spectroscopy. **ISRN Materials Science**. 2013: 938625.

Goodwin, S. and Walsh, D. A. (2017). Closed Bipolar Electrodes for Spatial Separation of H₂ and O₂ Evolution during Water Electrolysis and the Development of High-Voltage Fuel Cells. **ACS Applied Materials & Interfaces**. 9(28): 23654-23661.

Grunwaldt, J. D. and Baiker, A. (2005). *In situ* spectroscopic investigation of heterogeneous catalysts and reaction media at high pressure. **Physical Chemistry Chemical Physics**. 7(20): 3526-3539.

Guan, B. J., van Hoef, V., Jobava, R., Elroy-Stein, O., Valasek, L. S., Cargnello, M., Gao, X. H. Krokowski, D., Merrick, W. C., Kimball, S. R., Komar, A. A., Koromilas, A. E., Wynshaw-Boris, A., Topisirovic, I., Larsson, O. and

- Hatzoglou, M. (2017). A Unique ISR Program Determines Cellular Responses to Chronic Stress. **Molecular Cell**. 68(5): 885-900.e6.
- Henning, S. and Adhikari, R. (2017). Chapter 1-Scanning Electron Microscopy, ESEM, and X-ray Microanalysis. In: S. Thomas, R. Thomas, A. K. Zachariah and R. K. Mishra (Editors), *Microscopy Methods in Nanomaterials Characterization*. Elsevier. pp. 1-30.
- Holladay, J. D., Hu, J., King, D. L. and Wang, Y. (2009). An overview of hydrogen production technologies. **Catalysis Today**. 139(4): 244-260.
- Hou, M., Chen, L., Guo, Z., Dong, X., Wang, Y. and Xia, Y. (2018). A clean and membrane-free chlor-alkali process with decoupled Cl₂ and H₂/NaOH production. **Nature Communications**. 9(1): 438.
- Hu, L. and Xu, K. (2014). Nonflammable electrolyte enhances battery safety. **Proceedings of the National Academy of Sciences**. 111(9): 3205.
- Huang, L., Peng, F., Yu, H. and Wang, H. (2009). Preparation of cuprous oxides with different sizes and their behaviors of adsorption, visible-light driven photocatalysis and photocorrosion. **Solid State Sciences**. 11(1): 129-138.
- Ingham, B. and Toney, M. F. (2014). 1-X-ray diffraction for characterizing metallic films. In: K. Barmak and K. Coffey (Editors), *Metallic Films for Electronic, Optical and Magnetic Applications*. Woodhead Publishing. pp. 3-38.
- Inkson, B. J. (2016). 2-Scanning electron microscopy (SEM) and transmission electron microscopy (TEM) for materials characterization. In: G. Hübschen, I. Altpeter, R. Tschuncky and H.-G. Herrmann (Editors), *Materials Characterization Using Nondestructive Evaluation (NDE) Methods*. Woodhead Publishing. pp. 17-43.

- Jia, J., Seitz, L. C., Benck, J. D., Huo, Y., Chen, Y., Ng, J. W. D., Bilir, T., Harris, J. S. and Jaramillo, T. F. (2016). Solar water splitting by photovoltaic-electrolysis with a solar-to-hydrogen efficiency over 30%. **Nature Communications**. 7(1): 13237.
- Jin, L. and Seifitokaldani, A. (2020). *In Situ* Spectroscopic Methods for Electrocatalytic CO₂ Reduction. **Catalysts**. 10(5): 481.
- John, S. and Roy, S. C. (2019). CuO/Cu₂O nanoflake/nanowire heterostructure photocathode with enhanced surface area for photoelectrochemical solar energy conversion. **Applied Surface Science**. 144703.
- Kakuta, S. and Abe, T. (2009). Structural characterization of Cu₂O after the evolution of H₂ under visible light irradiation. **Electrochemical and Solid-State Letters**. 12(3): P1-P3.
- Kalasina, S., Pattanasattayavong, P., Suksomboon, M., Phattharasupakun, N., Wutthiprom, J., and Sawangphruk, M. (2017). A new concept of charging supercapacitors based on the photovoltaic effect. **Chemical Communications**. 53(4): 709-712.
- Kalasina, S., Phattharasupakun, N., Maihom, T., Promarak, V., Sudyoadsuk, T., Limtrakul, J., and Sawangphruk, M. (2018). Novel Hybrid Energy Conversion and Storage Cell with Photovoltaic and Supercapacitor Effects in Ionic Liquid Electrolyte. **Scientific Reports**. 8(1): 12192.
- Khan, M. E., Khan, M. M. and Cho, M. H. (2017). Ce³⁺-ion, Surface Oxygen Vacancy, and Visible Light-induced Photocatalytic Dye Degradation and Photocapacitive Performance of CeO₂-Graphene Nanostructures. **Scientific Reports**. 7(1): 5928.

- Koningsberger, D. C. (1988). X-ray absorption: principles, applications, techniques of EXAFS, SEXAFS, and XANES. **John Wiley and Sons**. United States.
- Kötz, R. and Carlen, M. (2000). Principles and applications of electrochemical capacitors. **Electrochimica Acta**. 45(15): 2483-2498.
- Landman, A., Dotan, H., Shter, G. E., Wullenkord, M., Houaijia, A., Maljusch, A., Grader, G. S. and Rothschild, A. (2017). Photoelectrochemical water splitting in separate oxygen and hydrogen cells. **Nature Materials**. 16: 646.
- Landman, A., Halabi, R., Dias, P., Dotan, H., Mehlmann, A., Shter, G. E., Halabi, M., Naseraldeen, O., Mendes, A., Grader, G. S. and Rothschild, A. (2020). Decoupled Photoelectrochemical Water Splitting System for Centralized Hydrogen Production. **Joule**. 4(2): 448-471.
- Le Goff, A., Artero, V., Jusselme, B., Tran, P. D., Guillet, N., Métayé, R., Fihri, A., Palacin, S. and Fontecave, M. (2009). From Hydrogenases to Noble Metal-Free Catalytic Nanomaterials for H₂ Production and Uptake. **Science**. 326(5958): 1384-1387.
- Li, N., Wang, Y., Tang, D. and Zhou, H. (2015). Integrating a Photocatalyst into a Hybrid Lithium-Sulfur Battery for Direct Storage of Solar Energy. **Angewandte Chemie International Edition**. 54(32): 9271-9274.
- Li, Q., Lu, X. F., Xu, H., Tong, Y. X. and Li, G. R. (2014). Carbon/MnO₂ Double-Walled Nanotube Arrays with Fast Ion and Electron Transmission for High-Performance Supercapacitors. **ACS Applied Materials & Interfaces**. 6(4): 2726-2733.

- Li, X., Wang, H. Y., Yang, H., Cai, W., Liu, S. and Liu, B. (2018). *In Situ/Operando* Characterization Techniques to Probe the Electrochemical Reactions for Energy Conversion. **Small Methods**. 1700395.
- Lifshin, E. (Ed.). (2008). X-ray Characterization of Materials. **John Wiley & Sons**. pp 1-103.
- Liu, J., Ke, J., Li, D., Sun, H., Liang, P., Duan, X., Tain, W., Tadó, M. O., Liu, S. and Wang, S. (2017). Oxygen Vacancies in Shape Controlled Cu₂O/Reduced Graphene Oxide/In₂O₃ Hybrid for Promoted Photocatalytic Water Oxidation and Degradation of Environmental Pollutants. **ACS Applied Materials & Interfaces**. 9(13): 11678-11688.
- Liu, Q., Wang, F., Lin, H., Xie, Y., Tong, N., Lin, J., Zhang, X., Zhang, Z. and Wang, X. (2018). Surface oxygen vacancy and defect engineering of WO₃ for improved visible light photocatalytic performance. **Catalysis Science & Technology**. 8(17): 4399-4406.
- Liu, Y., Li, N., Wu, S., Liao, K., Zhu, K., Yi, J. and Zhou, H. (2015). Reducing the charging voltage of a Li–O₂ battery to 1.9 V by incorporating a photocatalyst. **Energy & Environmental Science**. 8(9): 2664-2667.
- Lu, L., Xu, X., Yan, J., Shi, F. N. and Huo, Y. (2018). Oxygen vacancy rich Cu₂O based composite material with nitrogen doped carbon as matrix for photocatalytic H₂ production and organic pollutant removal. **Dalton Transactions**. 47(6): 2031-2038.
- Luo, J., Im, J. H., Mayer, M. T., Schreier, M., Nazeeruddin, M. K., Park, N. G., Tilley, S. D., Fan, H. J. and Grätzel, M. (2014). Water photolysis at 12.3% efficiency

- via perovskite photovoltaics and Earth-abundant catalysts. **Science**. 345(6204): 1593.
- Luo, J., Steier, L., Son, M. K., Schreier, M., Mayer, M. T. and Grätzel, M. (2016). Cu₂O Nanowire Photocathodes for Efficient and Durable Solar Water Splitting. **Nano Letters**. 16(3): 1848-1857.
- LV, Y., Yao, W., Zong, R. and Zhu, Y. (2016). Fabrication of Wide-Range-Visible Photocatalyst Bi₂WO_{6-x} nanoplates via Surface Oxygen Vacancies. **Scientific Reports**. 6: 19347.
- Mallouk, T.E. (2013). Divide and conquer. **Nature Chemistry**. 5(5): 362-363.
- Masingboon, C., Eknapakul, T., Suwanwong, S., Buaphet, P., Nakajima, H., Mo, S. K., Thongbai, P., King, P. D. C., Maensiri, S. and Meevasana, W. (2013). Anomalous change in dielectric constant of CaCu₃Ti₄O₁₂ under violet-to-ultraviolet irradiation. **Applied Physics Letters**. 102: 202903.
- May, M. M., Lewerenz, H. J., Lackner, D., Dimroth, F. and Hannappel, T. (2015). Efficient direct solar-to-hydrogen conversion by *in situ* interface transformation of a tandem structure. **Nature Communications**. 6(1): 8286.
- McHugh, P. J., Stergiou, A. D. and Symes, M. D. (2020). Decoupled Electrochemical Water Splitting: From Fundamentals to Applications. **Advanced Energy Materials**. 10(44): 2002453.
- Meevasana, W., King, P. D. C., He, R. H., Mo, S. K., Hashimoto, M., Tamai, A., Songsiriritthigul, P., Baumberger, F. and Shen, Z. X. (2011). Creation and control of a two-dimensional electron liquid at the bare SrTiO₃ surface. **Nature Materials**. 10: 114.

- Mir, W.J., Mahor, Y., Lohar, A., Jagadeeswararao, M., Das, S., Mahamuni, S. and Nag, A. (2018). Postsynthesis Doping of Mn and Yb into CsPbX₃ (X = Cl, Br, or I) Perovskite Nanocrystals for Downconversion Emission. **Chemistry of Materials**. 30(22): 8170-8178.
- Nathabumroong, S., Eknapakul, T., Jaiban, P., Yotburut, B., Siriroj, S., Saisopa, T., Mo, S. K., Supruangnet, R., Nakajima, H., Yimnirun, R., Maensiri, S. and Meevasana, W. (2020). Interplay of negative electronic compressibility and capacitance enhancement in lightly-doped metal oxide Bi_{0.95}La_{0.05}FeO₃ by quantum capacitance model. **Scientific Reports**. 10(1): 5153.
- Pandolfo, A.G. and Hollenkamp, A.F. (2006). Carbon properties and their role in supercapacitors. **Journal of Power Sources**. 157(1): 11-27.
- Pongha, S., Seekoan, B., Limphirat, W., Kidkhunthod, P., Srilomsak, S., Chiang, Y. M. and Meethong, N. (2015). XANES Investigation of Dynamic Phase Transition in Olivine Cathode for Li-Ion Batteries. **Advanced Energy Materials**. 5(15): 1500663.
- Qin, K., Liu, E., Li, J., Kang, J., Shi, C., He, C., He, F. and Zhao, N. (2016). Supercapacitors: Free-Standing 3D Nanoporous Duct-Like and Hierarchical Nanoporous Graphene Films for Micron-Level Flexible Solid-State Asymmetric Supercapacitors. **Advanced Energy Materials**. 6(18): 1600755.
- Rausch, B., Symes, M.D., Chisholm, G. and Cronin, L. (2014). Decoupled catalytic hydrogen evolution from a molecular metal oxide redox mediator in water splitting. **Science**. 345(6202): 1326.

- Reece, S. Y., Hamel, J. A., Sung, K., Jarvi, T. D., Esswein, A. J., Pijpers, J. J. and Nocera, D. G. (2011). Wireless Solar Water Splitting Using Silicon-Based Semiconductors and Earth-Abundant Catalysts. **Science**. 334(6056): 645-648.
- Safshekan, S., Herraiz-Cardona, I., Cardenas-Morcoso, D., Ojani, R., Haro, M. and Gimenez, S. (2017). Solar Energy Storage by a Heterostructured BiVO₄-PbO_x Photocapacitive Device. **ACS Energy Letters**. 2(2): 469-475.
- Saratale, R.G., Ghodake, G. S., Shinde, S. K., Cho, S. K., Saratale, G. D., Pugazhendhi, A. and Bharagava, R. N. (2018). Photocatalytic activity of CuO/Cu(OH)₂ nanostructures in the degradation of Reactive Green 19A and textile effluent, phytotoxicity studies and their biogenic properties (antibacterial and anticancer). **Journal of environmental management**. 223: 1086-1097.
- Senthilkumar, V., Kim, Y. S., Chandrasekaran, S., Rajagopalan, B., Kim, E. J. and Chung, J. S. (2015). Comparative supercapacitance performance of CuO nanostructures for energy storage device applications. **RSC Advances**. 5(26): 20545-20553.
- Shao, Y., El-Kady, M. F., Sun, J., Li, Y., Zhang, Q., Zhu, M., Wang, H., Dunn, B. and Kaner, R. B. (2018). Design and Mechanisms of Asymmetric Supercapacitors. **Chemical Reviews**. 118(18): 9233-9280.
- Shi, C., Dong, X., Wang, X., Ma, H. and Zhang, X. (2018). Ag nanoparticles deposited on oxygen-vacancy-containing BiVO₄ for enhanced near-infrared photocatalytic activity. **Chinese Journal of Catalysis**. 39(1): 128-137.
- Shu, X., Zheng, H., Xu, G., Zhao, J., Cui, L., Cui, J., Qin, Y., Wang, Y., Zhang, Y. and Wu, Y. (2017). The anodization synthesis of copper oxide nanosheet arrays and their photoelectrochemical properties. **Applied Surface Science**. 412: 505-516.

- Simon, P. and Gogotsi, Y. (2008). Materials for electrochemical capacitors. **Nature Materials**. 7(11): 845-854.
- Singh, M., Jampaiah, D., Kandjani, A. E., Sabri, Y. M., Della Gaspera, E., Reineck, P., Judd, M., Langley, J., Cox, N., van Embden, J., Mayes, E. L. H., Gibson, B. C., Bhargava, S. K., Ramanathan, R. and Bansal, V. (2018). Oxygen-deficient photostable Cu₂O for enhanced visible light photocatalytic activity. **Nanoscale**. 10(13): 6039-6050.
- Suen, N. T., Hung, S. F., Quan, Q., Zhang, N., Xu, Y. J. and Chen, H. M. (2017). Electrocatalysis for the oxygen evolution reaction: recent development and future perspectives. **Chemical Society Reviews**. 46(2): 337-365.
- Suwanwong, S., Eknapakul, T., Rattanachai, Y., Masingboon, C., Rattanasuporn, S., Phatthanakun, R., Nakajima, H., King, P. D. C., Hodak, S. K. and Meevasana, W. (2015). The dynamics of ultraviolet-induced oxygen vacancy at the surface of insulating SrTiO₃(001). **Applied Surface Science**. 355: 210-212.
- Symes, M. D. and Cronin, L. (2013). Decoupling hydrogen and oxygen evolution during electrolytic water splitting using an electron-coupled-proton buffer. **Nature Chemistry**. 5: 403.
- Tachibana, Y., Vayssieres, L. and Durrant, J. R. (2012). Artificial photosynthesis for solar water-splitting. **Nature Photonics**. 6(8): 511-518.
- Toe, C. Y., Scott, J., Amal, R. and Ng, Y. H. (2018). Recent advances in suppressing the photocorrosion of cuprous oxide for photocatalytic and photoelectrochemical energy conversion. **Journal of Photochemistry and Photobiology C: Photochemistry Reviews**. 40: 191-211.

- van Oversteeg, C. H. M., Doan, H. Q., de Groot, F. M. F. and Cuk, T. (2017). *In situ* X-ray absorption spectroscopy of transition metal based water oxidation catalysts. **Chemical Society Reviews**. 46(1): 102-125.
- Wang, M., Árnadóttir, L., Xu, Z. J. and Feng, Z. (2019). *In Situ* X-ray Absorption Spectroscopy Studies of Nanoscale Electrocatalysts. **Nano-Micro Letters**. 11(1): 47.
- Wang, Y., Jiang, T., Meng, D., Kong, J., Jia, H. and Yu, M. (2015). Controllable fabrication of nanostructured copper compound on a Cu substrate by a one-step route. **RSC Advances**. 5(21): 16277-16283.
- Wang, Y., Lany, S., Ghanbaja, J., Fagot-Revurat, Y., Chen, Y. P., Soldera, F., Horwat, D., Mücklich, F. and Pierson, J. F. (2016). Electronic structures of Cu_2O , Cu_3O_4 and CuO : A joint experimental and theoretical study. **Physical Review B**. 94(24): 245418.
- Wu, L., Tsui, L. K., Swami, N. and Zangari, G. (2010). Photoelectrochemical Stability of Electrodeposited Cu_2O Films. **The Journal of Physical Chemistry C**. 114(26): 11551-11556.
- Wu, Y., Jiang, J., Weng, Z., Wang, M., Broere, D. L., Zhong, Y., Brudvig, G. W., Feng, Z. and Wang, H. (2017). Electroreduction of CO_2 Catalyzed by a Heterogenized Zn-Porphyrin Complex with a Redox-Innocent Metal Center. **ACS Central Science**. 3(8): 847-852.
- Xia, X., Luo, J., Zeng, Z., Guan, C., Zhang, Y., Tu, J., Zhang, H. and Fan, H. J. (2012). Integrated photoelectrochemical energy storage: solar hydrogen generation and supercapacitor. **Scientific Reports**. 2: 981.

- Xiang, C., Papadantonakis, K. M. and Lewis, N. S. (2016). Principles and implementations of electrolysis systems for water splitting. **Materials Horizons**. 3(3): 169-173.
- Xiao, Z., Wang, Y., Huang, Y. C., Wei, Z., Dong, C. L., Ma, J., Shen, S., Li, Y. and Wang, S. (2017). Filling the oxygen vacancies in Co_3O_4 with phosphorus: an ultra-efficient electrocatalyst for overall water splitting. **Energy & Environmental Science**. 10(12): 2563-2569.
- Xu, L., Li, J., Sun, H., Guo, X., Xu, J., Zhang, H. and Zhang, X. (2019). *In situ* Growth of $\text{Cu}_2\text{O}/\text{CuO}$ Nanosheets on Cu Coating Carbon Cloths as a Binder-Free Electrode for Asymmetric Supercapacitors. **Frontiers in Chemistry**. 7(420).
- Xu, P., Liu, J., Liu, T., Ye, K., Cheng, K., Yin, J., Cao, D., Wang, G. and Li, Q. (2016). Preparation of binder-free $\text{CuO}/\text{Cu}_2\text{O}/\text{Cu}$ composites: a novel electrode material for supercapacitor applications. **RSC Advances**. 6(34): 28270-28278.
- Xu, P., Ye, K., Du, M., Liu, J., Cheng, K., Yin, J., Wang, G. and Cao, D. (2015). One-step synthesis of copper compounds on copper foil and their supercapacitive performance. **RSC Advances**. 5(46): 36656-36664.
- Yan, Y., Shi, W., Peng, W., Lin, Y., Zhang, C., Li, L., Sun, Y., Ju, H., Zhu, J., Ma, W. and Zhao, J. (2019). Proton-free electron-trapping feature of titanium dioxide nanoparticles without the characteristic blue color. **Communications Chemistry**. 2(1): 88.
- Yang, N., Yu, S., Macpherson, J. V., Einaga, Y., Zhao, H., Zhao, G., Swain, G. M. and Jiang, X. (2019). Conductive diamond: synthesis, properties, and electrochemical applications. **Chemical Society Reviews**. 48(1): 157-204.

- Yang, Y., Xu, D., Wu, Q. and Diao, P. (2016). Cu₂O/CuO Bilayered Composite as a High-Efficiency Photocathode for Photoelectrochemical Hydrogen Evolution Reaction. **Scientific Reports**. 6(1): 35158.
- Yoshida, M., Yomogida, T., Mineo, T., Nitta, K., Kato, K., Masuda, T., Nitani, H., Abe, H., Takakusagi, S., Uruga, T., Asakura, K., Uosaki, K. and Kondoh, H. (2014). Photoexcited Hole Transfer to a MnO_x Cocatalyst on a SrTiO₃ Photoelectrode during Oxygen Evolution Studied by *In Situ* X-ray Absorption Spectroscopy. **The Journal of Physical Chemistry C**. 118(42): 24302-24309.
- You, B. and Sun, Y. (2018). Innovative Strategies for Electrocatalytic Water Splitting. **Accounts of Chemical Research**. 51(7): 1571-1580.
- Zaafarany, I. and Boller, H. (2009). Electrochemical behavior of copper electrode in sodium hydroxide solutions. **Current World Environment**. 4: 277-284.
- Zhai, Y., Dou, Y., Zhao, D., Fulvio, P. F., Mayes, R. T. and Dai, S. (2011). Carbon Materials for Chemical Capacitive Energy Storage. **Advanced Materials**. 23(42): 4828-4850.
- Zhang, L. L. and Zhao, X. S. (2009). Carbon-based materials as supercapacitor electrodes. **Chemical Society Reviews**. 38(9): 2520-2531.
- Zhang, Y. C., Afzal, N., Pan, L., Zhang, X. and Zou, J. J. (2019). Structure-Activity Relationship of Defective Metal-Based Photocatalysts for Water Splitting: Experimental and Theoretical Perspectives. **Advanced Science**. 6(10): 1900053.
- Zhang, Y., Huang, M., Li, F. and Wen, Z. (2013). Controlled Synthesis of Hierarchical CuO Nanostructures for Electrochemical Capacitor Electrodes. **International Journal of Electrochemical Science**. 8: 8645-8661.

Zhang, Z. and Wang, P. (2012). Highly stable copper oxide composite as an effective photocathode for water splitting via a facile electrochemical synthesis strategy.

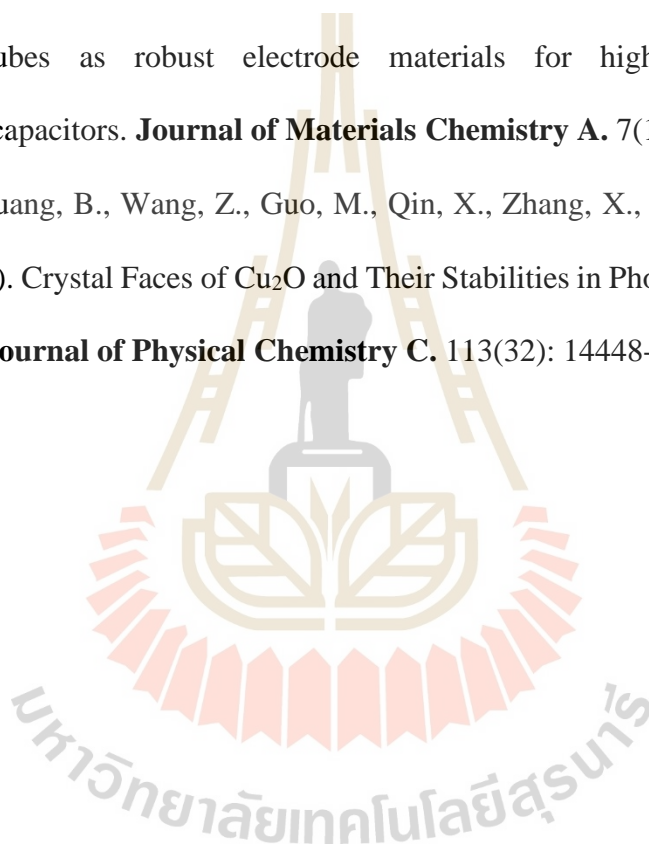
Journal of Materials Chemistry. 22(6): 2456-2464.

Zhao, J., Li, Z., Shen, T., Yuan, X., Qiu, G., Jiang, Q., Lin, Y., Song, G., Meng, A. and Li, Q. (2019). Oxygen-vacancy Bi₂O₃ nanosheet arrays with excellent rate capability and CoNi₂S₄ nanoparticles immobilized on N-doped graphene nanotubes as robust electrode materials for high-energy asymmetric supercapacitors. **Journal of Materials Chemistry A.** 7(13): 7918-7931.

Zheng, Z., Huang, B., Wang, Z., Guo, M., Qin, X., Zhang, X., Wang, P. and Dai, Y.

(2009). Crystal Faces of Cu₂O and Their Stabilities in Photocatalytic Reactions.

The Journal of Physical Chemistry C. 113(32): 14448-14453.





APPENDIX

APPENDIX

Photoenhanced Water Electrolysis in Separate O₂ and H₂ Cells Using Pseudocapacitive Electrodes

Supansa Musikajaroen, Siwat Polin, Suchinda Sattayaporn, Warakorn Jindata, Wittawat Saenrang, Pinit Kidkhunthod, Hideki Nakajima, Teera Butburee, Narong Chanlek, and Worawat Meevasana*

Cite This: ACS Omega 2021, 6, 19647–19655

Read Online

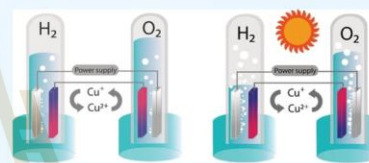
ACCESS |

Metrics & More

Article Recommendations

Supporting Information

ABSTRACT: Water electrolysis has received much attention in recent years as a means of sustainable H₂ production. However, many challenges remain in obtaining high-purity H₂ and making large-scale production cost-effective. This study provides a strategy for integrating a two-cell water electrolysis system with solar energy storage. In our proposed system, CuO-Cu(OH)₂/Cu₂O was used as a redox mediator between oxygen and hydrogen evolution components. The system not only overcame the gas-mixing issue but also showed high gas generation performance. The redox reaction (charge/discharge) of CuO-Cu(OH)₂/Cu₂O led to a significant increase (51%) in the initial rate of H₂ production from 111.7 μmol h⁻¹ cm⁻² in the dark to 168.9 μmol h⁻¹ cm⁻² under solar irradiation. The effects of light on the redox reaction of CuO-Cu(OH)₂/Cu₂O during water electrolysis were investigated by in situ X-ray absorption and photoemission spectroscopy. These results suggest that surface oxygen vacancies are created under irradiation and play an important role in increased capacitance and gas generation. These findings provide a new path to direct storage of abundant solar energy and low-cost sustainable hydrogen production.



INTRODUCTION

Water electrolysis provides a promising path for sustainable hydrogen production because it stands out as a mature, scalable technology for which the only required inputs are water and energy (in the form of electricity).¹ However, both improving the yield of high-purity H₂ and reducing the production cost remain challenges to the application of water electrolysis for large-scale hydrogen production.^{2–5} Therefore, water electrolysis in separate cells combined with renewable solar energy provides an alternative path for efficient device design and reduction of the cost of H₂ production.

In conventional water electrolysis, hydrogen and oxygen gases are simultaneously produced in the same cell. Mixing of these gases can occur during electrolysis, resulting in the degradation of electrolyzers as well as raising safety concerns.^{6,7} Therefore, several methods to prevent the mixing of gaseous H₂ and O₂ products are proposed.^{4–6,8–13} Cronin's group suggested a new method to separate gases produced in the conventional proton exchange membrane (PEM) water electrolysis process using a soluble molecular redox mediator (sulfotungstic acid) that mediates the electron-coupled proton exchange between the oxygen and hydrogen evolution reactions (OER and HER, respectively).^{9,10} Although PEM water electrolysis systems offer several advantages,^{9,10,13,15} their application remains hampered by the low efficiency and high cost of the Pt catalysts and membranes.¹¹ To overcome these problems, the separation of H₂ and O₂ production using Ni(OH)₂/NiOOH redox mediator electrodes in alkaline

aqueous solution was proposed.^{4,5,8,13} In this setup, the two separate cells use the redox reaction of Ni(OH)₂/NiOOH to mediate the ion exchange where there is a copper wire linking the two mediator electrodes instead of a membrane.^{8,5} Compared with PEM water electrolysis, alkaline water electrolysis exhibits inherent low-cost characteristics because it can use a nonprecious catalyst and a porous separator. The overall efficiency of water splitting in alkaline media would be better than that in acidic media.¹¹ Moreover, Rothschild's team provided the concept of using solar power to drive the separation of H₂ and O₂ production in this two-cell setup.⁴ In this work, we would firstly look into another oxide material (i.e., CuO-Cu(OH)₂/Cu₂O) that can be used as a redox mediator, and with Rothschild's concept of solar power, we would also like to investigate if the gas production can be further enhanced via the solar irradiation of the mediator electrodes.

The CuO, Cu(OH)₂, and Cu₂O electrodes have been widely used in rechargeable batteries and pseudocapacitors using alkaline electrolytes due to their high redox reaction and specific capacitance.^{16–19} Therefore, the redox-reversible CuO-

Received: May 2, 2021
Accepted: July 7, 2021
Published: July 21, 2021



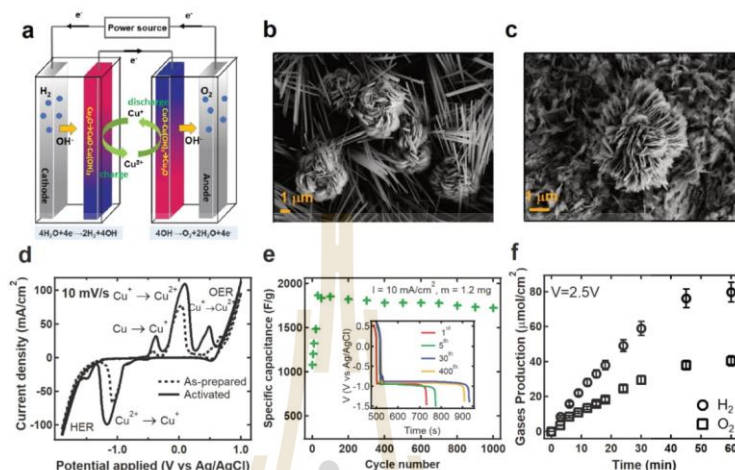


Figure 1. Redox mediator electrodes and experimental setup. (a) Schematic diagram of the electrolysis system. (b) SEM image of the CuO-Cu(OH)₂ as-prepared electrode directly grown onto a copper foil via surface oxidation in alkaline solution. At the reaction time of 30 min, the CuO micro-flowers are standing on Cu(OH)₂ nanowire arrays. (c) SEM image of the CuO-Cu(OH)₂ electrode after the activation process that included 300 activation cycles with charge and discharge steps at a constant current of 30 mA (3 mA/cm²). After activation, the Cu(OH)₂ nanowire transformed to CuO flower petals with a nanoscale thickness. (d) CV curves of CuO-Cu(OH)₂ electrode before and after the activation process at 10 mV/s with potential range from -2 to 1 V vs Ag/AgCl. (e) The cycling stability and galvanostatic discharge curves (inset) of the CuO-Cu(OH)₂/Cu-foil electrode by charge/discharge measurement at 10 mA/cm² and -1.4–0.6 V vs Ag/AgCl in 1 M NaOH. (f) H₂ and O₂ production that evolved during operation at a potential bias of 2.5 V in the two-cell water electrolysis that was set up according to the schematic diagram in (a).

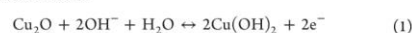
Cu(OH)₂/Cu₂O electrodes are suitable to be used as an ion exchange mediator in our two-cell water electrolysis system. The electrons transfer from one mediator electrode to another by the charge and discharge processes of mediator electrodes. Therefore, the capacitance of mediator electrodes has an important influence on the electrolysis rate in the two-cell water splitting system. Many studies report that charging and discharging of supercapacitive hydroxides and oxides under illumination can provide a higher areal current and capacitance due to photogenerated electron-hole pairs in the electrode materials.^{20–24} Compared with NiOOH/Ni(OH)₂, using CuO-Cu(OH)₂/Cu₂O as mediator electrodes could easily enhance the performance of a two-cell water electrolysis system by illumination due to its narrow band gap. It therefore strongly absorbs solar irradiation,^{25–28} which enables the generation of electron-hole pairs for enhanced redox and charge transfer in the water splitting system.

Herein, we present a concept providing a significant enhancement in the production of pure gases in a two-cell water electrolysis system by using charge-discharge Cu₂O/CuO-Cu(OH)₂ redox mediator electrodes under solar irradiation. In this work, the hydrogen and oxygen cells are separated by using CuO-Cu(OH)₂/Cu₂O mediator electrodes which substitute membrane separator for ion exchange between the anode and cathode. The CuO-Cu(OH)₂ (mixture of CuO and Cu(OH)₂) converts to Cu₂O during O₂ production at the anode (4OH⁻ → O₂ + 2H₂O + 4e⁻), while Cu₂O simultaneously converts to CuO-Cu(OH)₂ during H₂ production at the cathode (4H₂O + 4e⁻ → 2H₂ + 4OH⁻).

This system, the CuO-Cu(OH)₂ with Cu₂O, has both photosensitive and pseudocapacitive properties. The capacitance of mediator electrodes is improved greatly under light illumination by the creation of surface oxygen vacancies in the Cu₂O electrode. Therefore, the solar power can be captured and directly stored. This concept provides a new way of sustainable hydrogen production while reducing costs for large-scale utilization.

RESULTS

A CuO-Cu(OH)₂/Cu₂O redox couple was used as a mediator electrode in a two-cell water electrolysis system, as shown in the schematic in Figure 1a. The Cu₂O is used in the hydrogen production cell, and CuO-Cu(OH)₂ is used in the oxygen production cell. Electrons are transferred from Cu₂O to CuO-Cu(OH)₂, and ions (OH⁻) are exchanged between the primary electrodes (cathode and anode) by the charging and discharging of the Cu₂O/CuO-Cu(OH)₂ mediator electrodes. This process is accompanied by a visible color change from red to dark blue (see Figure S1a in the Supplementary Information). The charge and discharge cycle of the mediator pair depends on the reversible transformation of CuO-Cu(OH)₂/Cu₂O, which typically falls within the potential range of -1.5 to 0.7 V.^{17,19,29–31} The electrochemical reactions are as follows:



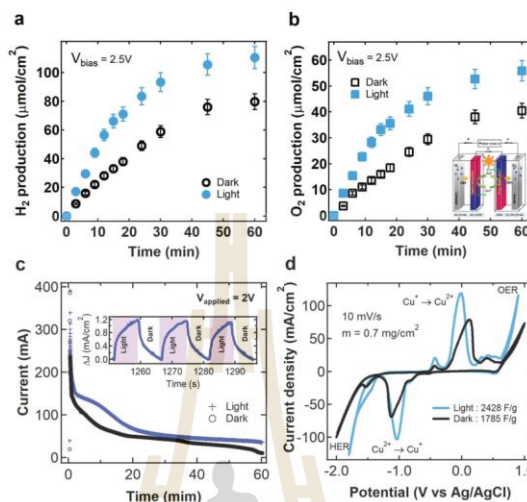


Figure 2. Effect of sunlight on CuO-Cu(OH)₂/Cu₂O redox mediator electrode. (a, b) H₂ and O₂ production in the two-cell water electrolysis system operated at a potential application of 2.5 V under dark and sunlight illumination. The sunlight was shone on the redox electrode (as shown in the inset (b)). (c) Current density of the two-cell water electrolysis system under sunlight conditions. The inset shows the additional current density depending on light on or off. (d) CV curve of the CuO-Cu(OH)₂ electrode at 10 mV/s in a three-electrode system under dark and sunlight illuminations.

To ensure the stability of the process during electrolysis, our CuO-Cu(OH)₂ electrodes were activated using the continuous charge/discharge process prior to fabricating the electrolytic cell. After activation, Cu(OH)₂ nanowires transform to CuO nanosheets with a thickness of approximately 50–100 nm as shown in Figure 1b,c, respectively (see details in Figures S2–S4). The changing of morphology provides a large electrode–electrolyte interface for an efficient redox reaction (see cyclic voltammetry (CV) curves in Figure 1d). The charge transfer and electrolyte diffusion resistance are smaller (Figure S5), leading to its specific capacitance in a potential range of −1.3–0.6 V vs Ag/AgCl that becomes larger than that of the as-prepared electrode (Figure 1e).

To start the electrolysis process, a constant voltage (2.5 and 3.0 V) was applied across the device for 1 h. Bubbles indicated the evolution of gaseous H₂ and O₂ at the cathode and anode, respectively, while there were no bubbles that formed at the mediator electrodes (Supplementary Note 6). The volume of gas evolved as a function of time at V = 2.5 V is shown in Figure 1f. The initial rates during the first 30 min are 111.7 and 57.2 μmol h^{−1} cm^{−2} (average rates of HER and OER are 74.9 and 38.7 μmol h^{−1} cm^{−2}); the H₂-to-O₂ ratio is approximately 2:1 in the consecutive cycles, similar to the previous studies.^{4,6} The production rate of H₂ and O₂ depends on the electrode's SOC (state of charge) (see Supplementary Note 7). Upon increasing the run time, the mediator electrode will be closer to the fully discharged state where the gas production will be stopped. Then, after approximately 1.2 h, the mediator electrode pair was nearly fully charged/discharged. Subsequent electrolysis could then be resumed by switching the applied voltage between the anode and cathode. Correlation of the

quantity of gas produced with the charge passed during electrolysis showed good average electrolysis efficiency ($\eta_V = V_{rev}/V_{app}$) of 47% (see Supplementary Note 1) and Faradaic efficiency of approximately 95 ± 2% (H₂ production) and 95% ± 4% (O₂ production) (Figure S8a), comparable to the Ni(OH)₂/NiOOH mediator pair studied in refs 2, 4. Deviation of the measured Faradaic efficiency from a theoretically achievable 100% yield is most likely due to a combination of gas leakage and dissolution of H₂ in the aqueous solution.

The cyclic stability of CuO-Cu(OH)₂/Cu₂O mediator electrodes (measurement area 1 cm²) was investigated by continuous charging and discharging for 1000 cycles at a current density of 10 mA/cm² (8.3 A/g) in 1 M NaOH solution within the potential range of −1.4–0.6 V vs Ag/AgCl. The specific capacitance curve shows a good retention rate as shown in Figure 1e where the specific capacitance remains to be at 1725 F/g after 1000 cycles or around 92% compared to that of the initially activated electrode (highest specific capacitance is 1867 F/g). During the charge–discharge process, the morphology of the mediator electrodes before and after looks similar to each other (Figure S2g,h), in agreement with the good retention, while some small degradation may come from the Cu(I)/Cu(0) reaction. Regarding the stability of the electrolysis system, the cycle duration as a function of cycle number is shown in Figure S9. The cycle duration decreases by only 7.5% after 55 electrolysis cycles, which is a good sign for the two-cell electrolysis system compared to the previous study.⁴

Interestingly, solar irradiation of the mediator electrodes during the charge and discharge processes led to an increase in the evolution rate of both H₂ and O₂ gases. As shown in Figure

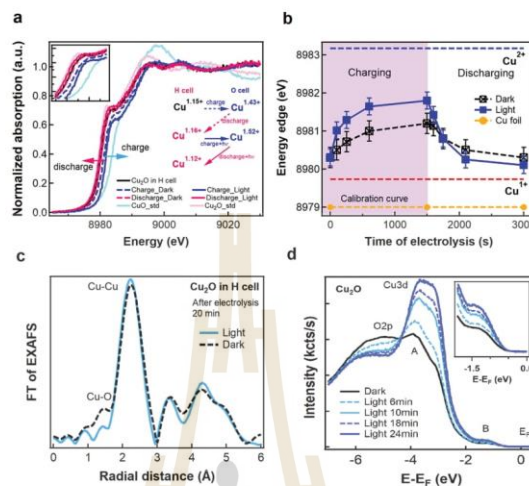


Figure 3. Electronic structure of $\text{CuO-Cu(OH)}_2/\text{Cu}_2\text{O}$ redox mediator electrode. (a) In situ Cu K-edge fluorescence XANES spectra of the mediator electrode during charging and discharging under dark and light illuminations in two-cell water electrolysis at 3 V. The changing of oxidation state for each condition is shown in the inset. (b, c) Changing absorption edge positions and FT EXAFS structures of redox mediator electrodes during charging and discharging under dark and light illumination. (d) Evolution of the valence band (VB) spectra of the Cu_2O redox mediator electrode from the pristine fractured surface to the light irradiated surface. Inset shows the evolution of the in-gap state with increasing exposure time.

$2a, b$, H_2 and O_2 were evolved at 110.4 and $55.8 \mu\text{mol h}^{-1} \text{cm}^{-2}$, representing an increase of approximately 38%, while initial evolution rates at 30 min increase up to 51%. This reflects a corresponding increase in the charge transfer ($Q = \int Idt$) between the anode and cathode (see Figure 2c), rising from 46 mAh in the absence of irradiation to 64 mAh under solar irradiation. The effect of solar irradiation was also studied by testing the two-cell water electrolysis under light on–off conditions. As shown in Figure 2c and inset, additional current density was observed when the CuO-Cu(OH)_2 and Cu_2O redox electrodes were operated under solar irradiation. This confirms that the presence of sunlight improves the yield of H_2 production.

To further elucidate the effect of solar irradiation on our system, the electrochemical properties of the $\text{CuO-Cu(OH)}_2/\text{Cu}_2\text{O}$ mediator pairs were investigated. The resulting cyclic voltammetry (CV) measurement is shown in Figure 2d. This further supports evidence that the $\text{CuO-Cu(OH)}_2/\text{Cu}_2\text{O}$ redox electrode provides a higher current density and specific capacitance under light irradiation. Photogenerated charge carriers drive the oxidation and reduction of $\text{Cu}_2\text{O}/\text{CuO-Cu(OH)}_2$ redox electrodes, leading to an enhancement of the specific capacitance by 36% compared with that in the absence of light.^{20–22,24}

The changing oxidation states in the $\text{CuO-Cu(OH)}_2/\text{Cu}_2\text{O}$ mediator electrode were tracked using in situ X-ray absorption spectroscopy (XAS) during charging and discharging in the presence and absence of solar irradiation. Figure 3a,b shows the resulting normalized Cu K-edge XANES spectra and the changes in the edge positions in the $\text{CuO-Cu(OH)}_2/\text{Cu}_2\text{O}$ mediator electrode, which was tracked during the electrolysis.

The position of the absorption edge contains information on the electronic structure of Cu within the electrode. During the charging process of Cu_2O in the hydrogen cell, XANES spectra showed a clear shift to higher-energy states (see blue dash lines in Figure 3a). This indicates a change in the Cu oxidation state from +1.15 to +1.43 during electrolysis at 3 V for 30 min. A shift of the XANES spectra in the opposite direction (see red lines in Figure 3a) was observed during the discharging process of CuO-Cu(OH)_2 in the oxygen cell. The oxidation state of Cu was reduced back to +1.16, which is near the initial oxidation state (+1.15). These observations indicate the reversibility of redox in $\text{CuO-Cu(OH)}_2/\text{Cu}_2\text{O}$ mediator electrodes. The changes in oxidation state during the charge and discharge processes are similar to those of other transition metal oxides in previous reports.^{32,33} Interestingly, under light irradiation at 3 V on the mediator electrode during the charging process in the electrolysis system, the XANES Cu K-edge energy significantly shifts according to oxidation of +1.16 to +1.52 (see blue spectra in Figure 3a,b). During the discharge process of the mediator electrode, a lower energy edge upon light irradiation (see red spectra in Figure 3a,b) indicated an increased amount of Cu^{1+} , with the average oxidation number changing from +1.52 to +1.12. This change of oxidation state is consistent with our CV measurements.

The Fourier transform of Cu K-edge EXAFS spectra of Cu_2O during electrolysis under dark and light conditions provides coordination information from the radial distribution function (RDF), which is shown in Figure 3c (see more details in Supplementary Note 10). The first peak at about 1.45 Å corresponds to the nearest neighbor to Cu and therefore originates from Cu–O bonds. The peak at 2.24 Å matches

well with Cu—O bonds in the Cu foil substrate, which is consistent with previous reports.^{34,35}

During the charging process (i.e., during electrolysis) under light irradiation, the radial distribution function obtained from EXAFS of the Cu₂O electrode showed a slight decrease in Cu—O bond length compared with the same measurement performed under dark conditions (see Supplementary Note 10). This effect can be seen in Figure 3c and corresponds to a significant change in the Cu—O coordination number resulting from fewer oxygen atoms as nearest neighbors. However, this effect was not observed in the case of CuO-Cu(OH)₂ electrode.

By using photoemission spectroscopy (PES), the electronic structure of the mediator electrode under illumination was also measured, which helps to elucidate the reaction mechanism at the electrodes during electrolysis. Figure 3d shows the valence band spectra of the Cu₂O mediator electrode with different carrier-dopants. It is clear that the valence band maximum is slightly shifted toward the Fermi level and the ratio of the Cu3d state (1.5–4 eV) to the O2p state (4–8 eV)³⁶ increases with increased carrier doping. This suggests a surface electron accumulation. It also indicates that electrons can be transferred from Cu₂O in the hydrogen cell to CuO-Cu(OH)₂ in the oxygen cell. This is consistent with the increase of current density in the CV curve and XAS results.

DISCUSSIONS

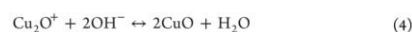
In a two-cell water electrolysis system, the CuO-Cu(OH)₂ and Cu₂O present both pseudocapacitive and photosensitive behaviors with high specific capacitance and excellent cycling stability. The integration of photosupercapacitive behavior with a mediator system in a single electrode offers important advantages. Specifically, the rate of evolution of H₂ and O₂ gases is significantly increased during sunlight irradiation onto the mediator electrodes. This is because the sunlight has an important influence on the pseudocapacitance behavior (Figure 2d). The solar power can be captured and directly stored chemically in redox mediator electrodes.

Under light irradiation, the charge in the electrolysis system was increased by 39% compared to that under dark conditions. In turn, the initial H₂ and O₂ evolution rates were significantly enhanced up to 51%. However, this effect depends strongly on which electrode is irradiated, as shown in the supplementary material (Figure S11). Irradiation of either the Cu₂O electrode alone or both electrodes at once produces a similar increase in gas evolution. On the other hand, when only the CuO-Cu(OH)₂ electrode in the oxygen cell is irradiated, there is a much weaker increase in the rate of gas evolution. This is because the conduction band minimum (CBM) of Cu₂O is higher in energy than the CBM of CuO.^{35,37} Therefore, during the charge/discharge process, photogenerated electrons can easily transfer from Cu₂O to CuO but not the other way around.

The redox mechanism of the Cu₂O and CuO-Cu(OH)₂ mediator electrode pair during the charging/discharging process under light illumination in two-cell electrolysis involves a photoassisted charging mechanism of electrodes. During the charging process in the hydrogen cell, the valence electrons of Cu₂O are excited to the conduction band under light illumination, resulting in the generation of electron–hole pairs (eq 3). The holes accumulate at the Cu₂O/water interface and oxidize Cu₂O into CuO (eq 4).^{20,38–43} Simultaneously, the photogenerated electrons pass through

the external circuit^{18,22} to reduce the CuO-Cu(OH)₂ electrode in the oxygen cell. During the discharge process in the oxygen cell, CuO-Cu(OH)₂ can be reduced back to Cu₂O by following a reversible redox reaction process (eq 5).

The redox mechanism under light irradiation is as follows:^{20,39,42}



More importantly, during light illumination, the photo-generated holes with oxidation react with mediator electrodes. This promotes the utilization of the electrode materials and further enhances the specific capacitance.

In situ Cu K-edge XANES was used to study the local electronic structure of redox mediator electrodes during electrolysis at a constant system voltage of 3 V. Upon light irradiation of the Cu₂O mediator electrode in the hydrogen cell, a larger shift of the Cu K-edge energy (Figure 3b) during charging indicated a greater positive shift in the oxidation state of Cu compared with the same experiment performed in the absence of light. This suggests that the photogenerated holes^{46,45} in the Cu₂O electrode assisted the oxidation of Cu₂O to CuO-Cu(OH)₂. On the other hand, the reduction of the Cu oxidation state in CuO-Cu(OH)₂ during the discharging process under irradiation suggests the migration of electrons from the Cu₂O electrode to the CuO-Cu(OH)₂ electrode. These electrons consequently reduced CuO-Cu(OH)₂ to Cu₂O. The reduction was more pronounced under light irradiation due to the difference in charge storage between dark and light conditions. These results confirm the photoassist charging of the mediator electrodes during water electrolysis, which is in good agreement with electrochemical results.

The Fourier transforms of Cu K-edge EXAFS spectra (shown in Figure 3c) of Cu₂O during electrolysis under dark and light conditions were also studied to support the observations made from XANES. Interestingly, the only significant change in these arose from shifts in the Cu—O bond peak. A lower coordination number of Cu—O bonds under irradiation is indicated, suggesting that oxygen vacancies^{46,47} are created in the Cu₂O electrode during electrolysis under light irradiation.

Electronic change local to the surface of the redox mediator electrodes was also tracked by taking both the valence band and XPS photoemission spectra of Cu₂O and CuO-Cu(OH)₂ during irradiation (Figure 3d and Figure S12 and S13, respectively). As exposure time increased, the O2p state decreases and its leading edge shifts slightly toward the Fermi level. It is accompanied by an increase in the intensity of the sub-gap state peak around 1.3 eV (inset in Figure 3d). Looking at previous studies, we consider that this sub-gap defect state is most likely associated with oxygen vacancies at the surface.^{48–52} The surface oxygen vacancies on Cu₂O electrodes play an important role in the separation of photogenerated electron–hole pairs and in the improvement of redox behavior involving photocapacitive performance.^{51–58} When Cu₂O is irradiated by light greater than its optical bandgap (valence band maximum (VBM) shift to EF), electron–hole pairs are generated (eq 3). Then, the photogenerated electrons are

trapped by surface oxygen vacancies (peak at 1.3 eV).^{54,55,59} These charges captured momentarily by surface oxygen vacancies are then readily transmitted to the Cu substrate^{55,60} (see schematic in Figure S14). Meanwhile, the photogenerated holes act to oxidize Cu₂O to CuO and H₂O as in eq 4. Our spectroscopic observations are consistent with the capacitive improvement of the mediator electrodes under solar irradiation as demonstrated in the CV curve. Importantly, oxygen vacancies enhance the electrical conductivity of transition metal oxides^{50,58} as a mediator electrode. The electron–hole pairs can be efficiently separated (inset in Figure 2c), resulting in higher gas evolution rates compared to those in the absence of light.

CONCLUSIONS

In conclusion, a two-cell electrolytic water splitting system has been developed with electrodes acting both as a redox mediator and as a photosupercapacitor for improved H₂ and O₂ gas production. The solar-driven pseudocapacitive behavior on the CuO–Cu(OH)₂/Cu₂O mediator electrode pair exhibits an increase in the specific capacitance compared with that in the absence of light (36%). This implies direct storage of solar energy that provided an increase in the initial H₂ and O₂ production rates of 51%. Our observations indicate that as a Cu₂O electrode is irradiated with solar light in a hydrogen cell, surface-localized oxygen vacancies are created. These play an important role in the separation of photogenerated electron–hole pairs, providing an improvement of redox behavior and capacitive activity in our two-cell water electrolysis system.

Regarding its application, this work provides a new strategy of combining a two-cell water electrolysis system with a photosupercapacitor in one device that is a route to low-cost and sustainable hydrogen production. Firstly, the two-cell system requires no expensive proton exchange membranes (PEM) commonly used in water electrolysis systems. Furthermore, in our system, the free solar irradiation could boost the performance of H₂ production by 51% and effectively increase the energy storage capacity of the mediator electrode. The effective increase in this solar-enhanced capacity is important for the cost optimization since the effective cost of energy storage is usually many folds of the solar cell panels proposed as the clean electricity generator for the H₂ production system.

EXPERIMENTAL DETAILS

Synthesis and Characterization of the CuO–Cu(OH)₂ Electrode. The Cu(OH)₂ nanowire/microflower-like CuO films on Cu foil were synthesized by chemical oxidation. A Cu foil (9 μm, 99%, MTI USA) was cut into 2.5 × 5 cm² sheets and cleaned by ultrasonication (water bath, 240 W) in acetone, ethanol, and distilled water at room temperature for 10 min sequentially. Impurities and oxide layers were removed from the surface by immersing in 1 M HCl solution for 30 min.¹⁹ The cleaned Cu foil was then immersed in an aqueous solution consisting of 24 mL of 10 M NaOH, 12 mL of 1 M (NH₄)₂S₂O₈, and 54 mL of distilled water¹⁹ at room temperature (25 °C). After 15–30 min, a dark-blue film covered the Cu foil surface, indicating the formation of Cu(OH)₂. The Cu(OH)₂-coated Cu foil was then taken from the solution, rinsed with water and then ethanol, and dried in air.

The morphology and chemical composition of the Cu(OH)₂ nanowire/microflower-like CuO were examined by scanning electron microscopy (SEM, ZEISS Auriga, operated at 5 keV) and energy-dispersive X-ray spectroscopy (EDS) (see Figures S2 and S3). The crystal structures of the samples were analyzed using an X-ray diffractometer (XRD, Bruker D2 Advance diffractometer) with Cu Kα radiation (λ = 0.1506 nm). The XRD patterns as shown in Figure S4 are measured with a scan rate of 10° min⁻¹ at a step width of 0.02°.

Electrochemical Characterization and Electrode Activation. The electrochemical measurement and electrode activation were carried out on a potentiostat/galvanostat. The Cu(OH)₂ nanowire/microflower-like CuO redox electrode was used as the working electrode (WE) in an electrochemical cell operated in a conventional three-electrode system with a Pt counter electrode (CE) and an Ag/AgCl reference electrode (RE) in an aqueous electrolyte solution of 1 M NaOH in deionized water. During the activation process, the working electrode was charged and discharged until its discharge capacity stabilized. At the end of the activation process, one of the redox electrodes (size 2.5 × 4 cm²) was charged and converted to CuO–Cu(OH)₂ by constant current charging (4 mA/cm², 1.5 h), whereas the other one (size 2.5 × 4 cm²) was discharged and converted to Cu₂O by constant current discharging (–4 mA/cm², 1.5 h). In addition, the electrochemical measurement of half-cell electrodes (1 × 1 cm²) was performed under dark and light illumination at 80 mW/cm² (approx. 0.8 Sun with 1.5 air mass) by using a PET solar simulator (model SS100AAA).

Two-Cell Water Electrolysis System. A two-cell water electrolysis system (shown in Figure 1a) was constructed with Ni foam primary electrodes (2.5 × 4 cm²) and CuO–Cu(OH)₂/Cu₂O (2.5 × 4 cm²) redox electrodes that had been activated beforehand as described above. The primary Ni electrodes (anode and cathode) were dipped in two glass bottles filled with alkaline aqueous solution (1 M NaOH in deionized water) and connected to a potentiostat/galvanostat. Two-electrode experiments were performed by attaching the counter and reference electrodes together, thereby giving a floating reference configuration. The redox electrodes were placed in the respective bottles in proximity to the primary electrodes (1.5 cm). The CuO–Cu(OH)₂ electrode was placed close to the Ni anode in the oxygen cell. And finally, the Cu₂O electrode was placed close to the Ni cathode in the hydrogen cell. The duration time of electrolysis cycles was 1 h with an applied constant voltage of 2–3 V. The threshold limit was set at 3 V to avoid gas generation at the redox mediator electrodes.

Performance of the Two-Cell Water Electrolysis System and Photoenhanced Pure Gas Production. To measure the gas volume and Faradaic efficiency of the total water electrolysis process at a constant applied voltage of 2 V in the two-electrode system, the volume of H₂ and O₂ production was measured using a custom-built device (shown in Supplementary Figure S8b). The mixing of gases during water electrolysis was monitored by an in situ gas chromatography technique. Before all gas analyses, the electrolyte and seal cells were purged with pure Ar (99%) or N₂ (99%) and pumped down to vacuum in several pump–purge cycles.

For the photoenhanced gas production measurement, the redox mediator electrode was exposed to simulate sunlight from the solar simulator. The light was reflected from a mirror and projected onto the sample (illumination area 10 cm²) with

an intensity of 80 mW/cm². The photoresponse of mediator electrodes during water electrolysis was performed under on-off light irradiation.

In Situ X-ray Absorption Spectroscopy (XAS). The Cu K-edge X-ray absorption experiments were conducted in fluorescent mode at BL5.2 of the Synchrotron Light Research Institute (SLRI), Thailand. The electron energy was 1.2 GeV, the beam current was 80–150 mA, and the maximum photon flux was about $1.1\text{--}1.7 \times 10^{11}$ photons s⁻¹. The X-ray beam size was 25 mm (width) \times 1 mm (height). To record XANES and EXAFS spectra in fluorescence mode, a four-channel Si detector after calibration with a Cu foil was used. The measurement parameters were adjusted to achieve a reliable dead time below 10% (1 s). The normalized XAS spectra were processed and analyzed by using the Athena and Artemis software. For in situ XANES and EXAFS measurements, all spectra were collected during water electrolysis in the two-cell setup. The electrolysis cell was made of acrylic material with dimensions of $5 \times 5 \times 7$ cm³ and a square hole (3×3 cm²) with Kapton tape as the entrance of the X-ray beam. The measurement was operated at a constant voltage of 3 V in both the presence and absence of laser light irradiation (450 nm, 80 mW/cm²) on mediator electrodes.

Photoemission Spectroscopy (PES). To understand the influence of light during electrolysis, the electronic structures of the mediator electrodes under laser light irradiation (450 nm, 80 mW/cm²) were investigated by using ultraviolet photoemission spectroscopy (UPS) at room temperature with a photon energy of 90 eV (electron mean free path \approx 5.5 Å) and a pass energy of 5 eV. The base pressure was better than 1×10^{-8} mbar. The valence band spectra were collected on a Scienta R4000 analyzer with an energy resolution of 30 meV at BL3.2a of the Synchrotron Light Research Institute (SLRI), Thailand. In addition, the elemental compositions of the electrodes in all conditions were analyzed by X-ray photoelectron spectroscopy (XPS) using a PHI5000 Versa Probe II (Ulvac-PHI, Japan) with Al K α radiation (photon energy 1486.6 eV) at BL5.3 of SLRI.

■ ASSOCIATED CONTENT

Supporting Information

The Supporting Information is available free of charge at <https://pubs.acs.org/doi/10.1021/acsomega.1c02305>.

The surface morphologies of the CuO-Cu(OH)₂ electrode, EDS and XRD analysis, electrochemical impedance spectroscopy study, the operation of the two-cell water electrolysis system, electrochemical properties, gas measurement and Faradaic efficiency, in situ gas chromatography, gas production of the two-cell water electrolysis under dark and light illumination, photoemission spectroscopy analysis, and proposed mechanism of charge transfer (PDF)

■ AUTHOR INFORMATION

Corresponding Author

Worawat Meevasana – Research Network NANOTEC-SUT on Advanced Nanomaterials and Characterization and School of Physics, Suranaree University of Technology, Nakhon Ratchasima 30000, Thailand; Thailand Center of Excellence in Physics, Ministry of Higher Education, Science, Research and Innovation, Bangkok 10400, Thailand;

orcid.org/0000-0003-2994-6249; Email: worawat@g.sut.ac.th

Authors

Supansa Musikajaroen – Research Network NANOTEC-SUT on Advanced Nanomaterials and Characterization and School of Physics, Suranaree University of Technology, Nakhon Ratchasima 30000, Thailand; Thailand Center of Excellence in Physics, Ministry of Higher Education, Science, Research and Innovation, Bangkok 10400, Thailand

Siwat Polin – Research Network NANOTEC-SUT on Advanced Nanomaterials and Characterization and School of Physics, Suranaree University of Technology, Nakhon Ratchasima 30000, Thailand

Suchinda Sattayaporn – Synchrotron Light Research Institute, Nakhon Ratchasima 30000, Thailand

Warakorn Jindata – Research Network NANOTEC-SUT on Advanced Nanomaterials and Characterization and School of Physics, Suranaree University of Technology, Nakhon Ratchasima 30000, Thailand

Wittawat Saenrang – Research Network NANOTEC-SUT on Advanced Nanomaterials and Characterization and School of Physics, Suranaree University of Technology, Nakhon Ratchasima 30000, Thailand; Thailand Center of Excellence in Physics, Ministry of Higher Education, Science, Research and Innovation, Bangkok 10400, Thailand

Pinit Kidkhunthod – Synchrotron Light Research Institute, Nakhon Ratchasima 30000, Thailand

Hideki Nakajima – Synchrotron Light Research Institute, Nakhon Ratchasima 30000, Thailand

Teera Butburee – National Nanotechnology Center, National Science and Technology Development Agency, Pathum Thani 12120, Thailand

Narong Chanlek – Synchrotron Light Research Institute, Nakhon Ratchasima 30000, Thailand

Complete contact information is available at:

<https://pubs.acs.org/doi/10.1021/acsomega.1c02305>

Author Contributions

W.M. conceived and guided the entire project. S.M. and S.P. designed and set up the experiment. S.M. performed the experiment and analyzed the data. H.N. and N.C. took the XPS/UPS measurement. S.S. and P.K. took and analyzed the XAS data. W.M. and S.M. wrote the manuscript. All authors participated in discussion of the results, commented on the manuscript, and have given approval to the final version of the manuscript. W.M. directed the research.

Notes

The authors declare no competing financial interest.

■ ACKNOWLEDGMENTS

We would like to thank S. Rattanasuporn, R. Supruangnet, W. Jenpiyapong, and A. Rattanachata for help in UPS/XPS measurement and C. Jaisuk, T. Eknapakul, A. Mooltang, and W. Saengsui for helpful discussion. This work was supported by the Program Management Unit for Human Resources and Institutional Development, Research and Innovation, Grant No. B05F630108 (Thailand), the Center of Excellence in Advanced Functional Materials (CoE-AFM), External Grants and Scholarships for Graduate Students (OROG) Suranaree University of Technology, the Research Network NANOTEC (RNN) program of the National Nanotechnology Center

(NANOTEC), NSTDA, and the Office of Naval Research Global under Grant N62909-18-1-2018.

REFERENCES

- Holladay, J. D.; Hu, J.; King, D. L.; Wang, Y. An overview of hydrogen production technologies. *Catal. Today* **2009**, *139*, 244–260.
- Shiva Kumar, S.; Himabindu, V. Hydrogen production by PEM water electrolysis – A review. *Mater. Sci. Energy Technol.* **2019**, *2*, 442–454.
- Wang, S.; Lu, A.; Zhong, C.-J. Hydrogen production from water electrolysis: role of catalysts. *Nano Conver.* **2021**, *8*, 4.
- Landman, A.; Dotan, H.; Shter, G. E.; Wullenkord, M.; Houajija, A.; Maljusch, A.; Grader, G. S.; Rothschild, A. Photoelectrochemical water splitting in separate oxygen and hydrogen cells. *Nat. Mater.* **2017**, *16*, 646.
- Landman, A.; Halabi, R.; Dias, P.; Dotan, H.; Mehlmann, A.; Shter, G. E.; Halabi, M.; Naseraldeen, O.; Mendes, A.; Grader, G. S.; Rothschild, A. Decoupled Photoelectrochemical Water Splitting System for Centralized Hydrogen Production. *Joule* **2020**, *4*, 448–471.
- Goodwin, S.; Walsh, D. A. Closed Bipolar Electrodes for Spatial Separation of H₂ and O₂ Evolution during Water Electrolysis and the Development of High-Voltage Fuel Cells. *ACS Appl. Mater. Interfaces* **2017**, *9*, 23654–23661.
- Scheepers, F.; Stähler, M.; Stähler, A.; Rauls, E.; Müller, M.; Carmo, M.; Lehnert, W. Improving the Efficiency of PEM Electrolyzers through Membrane-Specific Pressure Optimization. *Energies* **2020**, *13*, 612.
- Chen, L.; Dong, X.; Wang, Y.; Xia, Y. Separating hydrogen and oxygen evolution in alkaline water electrolysis using nickel hydroxide. *Nat. Commun.* **2016**, *7*, 11741.
- Rausch, B.; Symes, M. D.; Chisholm, G.; Cronin, L. Decoupled catalytic hydrogen evolution from a molecular metal oxide redox mediator in water splitting. *Science* **2014**, *345*, 1326.
- Symes, M. D.; Cronin, L. Decoupling hydrogen and oxygen evolution during electrolytic water splitting using an electron-coupled-proton buffer. *Nat. Chem.* **2013**, *5*, 403.
- You, B.; Sun, Y. Innovative Strategies for Electrocatalytic Water Splitting. *Acc. Chem. Res.* **2018**, *51*, 1571–1580.
- Hou, M.; Chen, L.; Guo, Z.; Dong, X.; Wang, Y.; Xia, Y. A clean and membrane-free chlor-alkali process with decoupled Cl₂ and H₂/NaOH production. *Nat. Commun.* **2018**, *9*, 438.
- Dotan, H.; Landman, A.; Sheehan, S. W.; Malviya, K. D.; Shter, G. E.; Grave, D. A.; Arzi, Z.; Yehudai, N.; Halabi, M.; Gal, N.; Hadari, N.; Cohen, C.; Rothschild, A.; Grader, G. S. Decoupled hydrogen and oxygen evolution by a two-step electrochemical–chemical cycle for efficient overall water splitting. *Nat. Energy* **2019**, *4*, 786–795.
- Ahmad Kamaruddin, M. F.; Sabli, N.; Tuan Abdullah, T. A. *Hydrogen Production by Membrane Water Splitting Technologies*; IntechOpen: 2018, 19.
- Lamy, C. From hydrogen production by water electrolysis to its utilization in a PEM fuel cell or in a SO fuel cell: Some considerations on the energy efficiencies. *Int. J. Hydrogen Energy* **2016**, *41*, 15415–15425.
- Senthilkumar, V.; Kim, Y. S.; Chandrasekaran, S.; Rajagopalan, B.; Kim, E. J.; Chung, J. S. Comparative supercapacitance performance of CuO nanostructures for energy storage device applications. *RSC Adv.* **2015**, *5*, 20545–20553.
- Xu, L.; Li, J.; Sun, H.; Guo, X.; Xu, J.; Zhang, H.; Zhang, X. In situ Growth of Cu₂O/CuO Nanosheets on Cu Coating Carbon Cloths as a Binder-Free Electrode for Asymmetric Supercapacitors. *Front. Chem.* **2019**, *7*, 420.
- Xu, P.; Liu, J.; Liu, T.; Ye, K.; Cheng, K.; Yin, J.; Cao, D.; Wang, G.; Li, Q. Preparation of binder-free CuO/Cu₂O/Cu composites: a novel electrode material for supercapacitor applications. *RSC Adv.* **2016**, *6*, 28270–28278.
- Xu, P.; Ye, K.; Du, M.; Liu, J.; Cheng, K.; Yin, J.; Wang, G.; Cao, D. One-step synthesis of copper compounds on copper foil and their supercapacitive performance. *RSC Adv.* **2015**, *5*, 36656–36664.
- An, C.; Wang, Z.; Xi, W.; Wang, K.; Liu, X.; Ding, Y. Nanoporous Cu@Cu₂O hybrid arrays enable photo-assisted supercapacitor with enhanced capacities. *J. Mater. Chem. A* **2019**, *7*, 15691–15697.
- Kalasina, S.; Pattanasattayavong, P.; Suksomboon, M.; Phattharasupakun, N.; Wuthiprom, J.; Sawangphruk, M. A new concept of charging supercapacitors based on the photovoltaic effect. *Chem. Commun.* **2017**, *53*, 709–712.
- Kalasina, S.; Phattharasupakun, N.; Maihom, T.; Promarak, V.; Sudyoadsak, T.; Limtrakul, J.; Sawangphruk, M. Novel Hybrid Energy Conversion and Storage Cell with Photovoltaic and Supercapacitor Effects in Ionic Liquid Electrolyte. *Sci. Rep.* **2018**, *8*, 12192.
- Safshekan, S.; Herraiz-Cardona, I.; Cardenas-Morcoso, D.; Ojani, R.; Haro, M.; Gimenez, S. Solar Energy Storage by a Heterostructured BiVO₄–PbO₂ Photocapacitive Device. *ACS Energy Lett.* **2017**, *2*, 469–475.
- Xia, X.; Luo, J.; Zeng, Z.; Guan, C.; Zhang, Y.; Tu, J.; Zhang, H.; Fan, H. J. Integrated photoelectrochemical energy storage: solar hydrogen generation and supercapacitor. *Sci. Rep.* **2012**, *2*, 981.
- Dias, P.; Schreier, M.; Tilley, S. D.; Luo, J.; Azevedo, J.; Andrade, L.; Bi, D.; Hagfeldt, A.; Mendes, A.; Grätzel, M.; Mayer, M. T. Transparent Cuprous Oxide Photocathode Enabling a Stacked Tandem Cell for Unbiased Water Splitting. *Adv. Energy Mater.* **2015**, *5*, 1501537.
- Luo, J.; Steier, L.; Son, M.-K.; Schreier, M.; Mayer, M. T.; Grätzel, M. Cu₂O Nanowire Photocathodes for Efficient and Durable Solar Water Splitting. *Nano Lett.* **2016**, *16*, 1848–1857.
- Shu, X.; Zheng, H.; Xu, G.; Zhao, J.; Cui, L.; Cui, J.; Qin, Y.; Wang, Y.; Zhang, Y.; Wu, Y. The anodization synthesis of copper oxide nanosheet arrays and their photoelectrochemical properties. *Appl. Surf. Sci.* **2017**, *412*, 505–516.
- Zhang, Z.; Wang, P. Highly stable copper oxide composite as an effective photocathode for water splitting via a facile electrochemical synthesis strategy. *J. Mater. Chem.* **2012**, *22*, 2456–2464.
- Guan, B.-J.; van Hoef, V.; Jobava, R.; Elroy-Stein, O.; Valasek, L. S.; Cargnello, M.; Gao, X.-H.; Krokowski, D.; Merrick, W. C.; Kimball, S. R.; Komar, A. A.; Koromilas, A. E.; Wynshaw-Boris, A.; Topisirovic, I.; Larsson, O.; Hatzoglou, M. A Unique ISR Program Determines Cellular Responses to Chronic Stress. *Mol. Cell* **2017**, *68*, 885–900.e6.
- Zaafarany, I.; Boller, H. Electrochemical behavior of copper electrode in sodium hydroxide solutions. *Curr. World Environ.* **2009**, *4*, 277–284.
- Wang, Y.-H.; He, J.-B. Corrosion inhibition of copper by sodium phytate in NaOH solution: Cyclic voltabsorptometry for in situ monitoring of soluble corrosion products. *Electrochim. Acta* **2012**, *66*, 45–51.
- Pongha, S.; Seekoan, B.; Limphirat, W.; Kidkhunthod, P.; Srilomsak, S.; Chiang, Y.-M.; Meethong, N. XANES Investigation of Dynamic Phase Transition in Olivine Cathode for Li-Ion Batteries. *Adv. Energy Mater.* **2015**, *5*, 1500663.
- Xuning, L.; Wang, H.-Y.; Yang, H.; Cai, W.; Liu, S.; Liu, B. In Situ/Operando Characterization Techniques to Probe the Electrochemical Reactions for Energy Conversion. *Small Methods* **2018**, *1700395*.
- Aregahegn, A.; Gedamu, A.; Chen, H.-M.; Berhe, T.; Su, W.-N.; Hwang, B.-J. Highly stable CuS and CuS-Pt catalyzed Cu₂O/CuO heterostructure as efficient photocathode for hydrogen evolution reaction. *J. Mater. Chem. A* **2015**, *4*, 2205.
- Dubale, A. A.; Pan, C.-J.; Tamirat, A. G.; Chen, H.-M.; Su, W.-N.; Chen, C.-H.; Rick, J.; Ayele, D. W.; Aragaw, B. A.; Lee, J.-F.; Yang, Y.-W.; Hwang, B.-J. Heterostructured Cu₂O/CuO decorated with nickel as a highly efficient photocathode for photoelectrochemical water reduction. *J. Mater. Chem. A* **2015**, *3*, 12482–12499.
- Wang, Y.; Lany, S.; Ghanbaja, J.; Fagot-Revurat, Y.; Chen, Y. P.; Soldera, F.; Horwat, D.; Mücklich, F.; Pierson, J. F. Electronic structures of Cu₂O, Cu₃O₄ and CuO: A joint experimental and theoretical study. *Phys. Rev. B* **2016**, *94*, 245418.

- (37) Yang, Y.; Xu, D.; Wu, Q.; Diao, P. Cu₂O/CuO Bilayered Composite as a High-Efficiency Photocathode for Photoelectrochemical Hydrogen Evolution Reaction. *Sci. Rep.* **2016**, *6*, 35158.
- (38) Aguirre, M. E.; Zhou, R.; Eugene, A. J.; Guzman, M. I.; Grela, M. A. Cu₂O/TiO₂ heterostructures for CO₂ reduction through a direct Z-scheme: Protecting Cu₂O from photocorrosion. *Appl. Catal., B* **2017**, *217*, 485–493.
- (39) Huang, L.; Peng, F.; Yu, H.; Wang, H. Preparation of cuprous oxides with different sizes and their behaviors of adsorption, visible-light driven photocatalysis and photocorrosion. *Solid State Sci.* **2009**, *11*, 129–138.
- (40) Kakuta, S.; Abe, T. Structural characterization of Cu₂O after the evolution of H₂ under visible light irradiation. *Electrochem. Solid-State Lett.* **2009**, *12*, P1–P3.
- (41) Saratale, R. G.; Ghodake, G. S.; Shinde, S. K.; Cho, S.-K.; Saratale, G. D.; Pugazhendhi, A.; Bharagava, R. N. Photocatalytic activity of CuO/Cu(OH)₂ nanostructures in the degradation of Reactive Green 19A and textile effluent, phytotoxicity studies and their biogenic properties (antibacterial and anticancer). *J. Environ. Manage.* **2018**, *223*, 1086–1097.
- (42) Toe, C. Y.; Scott, J.; Amal, R.; Ng, Y. H. Recent advances in suppressing the photocorrosion of cuprous oxide for photocatalytic and photoelectrochemical energy conversion. *J. Photochem. Photobiol., C* **2018**, *191*.
- (43) Zheng, Z.; Huang, B.; Wang, Z.; Guo, M.; Qin, X.; Zhang, X.; Wang, P.; Dai, Y. Crystal Faces of Cu₂O and Their Stabilities in Photocatalytic Reactions. *J. Phys. Chem. C* **2009**, *113*, 14448–14453.
- (44) Yoshida, M.; Yomogida, T.; Mineo, T.; Nitta, K.; Kato, K.; Masuda, T.; Nitani, H.; Abe, H.; Takakusagi, S.; Uruga, T.; Asakura, K.; Uosaki, K.; Kondoh, H. Photoexcited Hole Transfer to a MnO₂ Cocatalyst on a SrTiO₃ Photoelectrode during Oxygen Evolution Studied by In Situ X-ray Absorption Spectroscopy. *J. Phys. Chem. C* **2014**, *118*, 24302–24309.
- (45) van Oversteeg, C. H. M.; Doan, H. Q.; de Groot, F. M. F.; Cuk, T. In situ X-ray absorption spectroscopy of transition metal based water oxidation catalysts. *Chem. Soc. Rev.* **2017**, *46*, 102–125.
- (46) Xiao, Z.; Wang, Y.; Huang, Y.-C.; Wei, Z.; Dong, C.-L.; Ma, J.; Shen, S.; Li, Y.; Wang, S. Filling the oxygen vacancies in Co₃O₄ with phosphorus: an ultra-efficient electrocatalyst for overall water splitting. *Energy Environ. Sci.* **2017**, *10*, 2563–2569.
- (47) Zhang, Y.-C.; Afzal, N.; Pan, L.; Zhang, X.; Zou, J.-J. Structure-Activity Relationship of Defective Metal-Based Photocatalysts for Water Splitting: Experimental and Theoretical Perspectives. *Adv. Sci.* **2019**, *6*, 1900053.
- (48) Masingboon, C.; Eknapakul, T.; Suwanwong, S.; Buaphet, P.; Nakajima, H.; Mo, S.-K.; Thongbai, P.; King, P. D. C.; Maensiri, S.; Meevasana, W. Anomalous change in dielectric constant of CaCu₂Ti₂O₇ under violet-to-ultraviolet irradiation. *Appl. Phys. Lett.* **2013**, *102*, 202903.
- (49) Meevasana, W.; King, P. D. C.; He, R. H.; Mo, S. K.; Hashimoto, M.; Tamai, A.; Songsririthigul, P.; Baumberger, F.; Shen, Z. X. Creation and control of a two-dimensional electron liquid at the bare SrTiO₃ surface. *Nat. Mater.* **2011**, *10*, 114.
- (50) Suwanwong, S.; Eknapakul, T.; Rattanachai, Y.; Masingboon, C.; Rattanasuporn, S.; Phatthanakun, R.; Nakajima, H.; King, P. D. C.; Hodak, S. K.; Meevasana, W. The dynamics of ultraviolet-induced oxygen vacancy at the surface of insulating SrTiO₃(001). *Appl. Surf. Sci.* **2015**, *355*, 210–212.
- (51) Singh, M.; Jampaiah, D.; Kandjani, A. E.; Sabri, Y. M.; Della Gaspera, E.; Reineck, P.; Judd, M.; Langley, J.; Cox, N.; van Embden, J.; Mayes, E. L. H.; Gibson, B. C.; Bhargava, S. K.; Ramanathan, R.; Bansal, V. Oxygen-deficient photostable Cu₂O for enhanced visible light photocatalytic activity. *Nanoscale* **2018**, *10*, 6039–6050.
- (52) Nathabumroong, S.; Eknapakul, T.; Jaiban, P.; Yotburut, B.; Siriroj, S.; Saisopa, T.; Mo, S. K.; Supruangnet, R.; Nakajima, H.; Yimnirun, R.; Maensiri, S.; Meevasana, W. Interplay of negative electronic compressibility and capacitance enhancement in lightly-doped metal oxide Bi_{0.93}La_{0.05}FeO₃ by quantum capacitance model. *Sci. Rep.* **2020**, *10*, 5153.
- (53) Liu, J.; Ke, J.; Li, D.; Sun, H.; Liang, P.; Duan, X.; Tian, W.; Tade, M. O.; Liu, S.; Wang, S. Oxygen Vacancies in Shape Controlled Cu₂O/Reduced Graphene Oxide/In₂O₃ Hybrid for Promoted Photocatalytic Water Oxidation and Degradation of Environmental Pollutants. *ACS Appl. Mater. Interfaces* **2017**, *9*, 11678–11688.
- (54) Khan, M. E.; Khan, M. M.; Cho, M. H. Ce³⁺-ion, Surface oxygen vacancy, and visible light-induced photocatalytic dye degradation and photocapacitive performance of CeO₂-graphene nanostructures. *Sci. Rep.* **2017**, *7*, 5928.
- (55) Liu, Q.; Wang, F.; Lin, H.; Xie, Y.; Tong, N.; Lin, J.; Zhang, X.; Zhang, Z.; Wang, X. Surface oxygen vacancy and defect engineering of WO₃ for improved visible light photocatalytic performance. *Catal. Sci. Technol.* **2018**, *8*, 4399–4406.
- (56) Lv, Y.; Yao, W.; Zong, R.; Zhu, Y. Fabrication of Wide-Range-Visible Photocatalyst Bi₂WO_{6-x} nanoplates via Surface Oxygen Vacancies. *Sci. Rep.* **2016**, *6*, 19347.
- (57) Zhao, J.; Li, Z.; Shen, T.; Yuan, X.; Qiu, G.; Jiang, Q.; Lin, Y.; Song, G.; Meng, A.; Li, Q. Oxygen-vacancy Bi₂O₃ nanosheet arrays with excellent rate capability and CoNi₂S₄ nanoparticles immobilized on N-doped graphene nanotubes as robust electrode materials for high-energy asymmetric supercapacitors. *J. Mater. Chem. A* **2019**, *7*, 7918–7931.
- (58) Lu, L.; Xu, X.; Yan, J.; Shi, F.-N.; Huo, Y. Oxygen vacancy rich Cu₂O based composite material with nitrogen doped carbon as matrix for photocatalytic H₂ production and organic pollutant removal. *Dalton Trans.* **2018**, *47*, 2031–2038.
- (59) Yan, Y.; Shi, W.; Peng, W.; Lin, Y.; Zhang, C.; Li, L.; Sun, Y.; Ju, H.; Zhu, J.; Ma, W.; Zhao, J. Proton-free electron-trapping feature of titanium dioxide nanoparticles without the characteristic blue color. *Commun. Chem.* **2019**, *2*, 88.
- (60) Cheng, Y.; Lin, Y.; Xu, J.; He, J.; Wang, T.; Yu, G.; Shao, D.; Wang, W.-H.; Lu, F.; Li, L.; Du, X.; Wang, W.; Liu, H.; Zheng, R. Surface plasmon resonance enhanced visible-light-driven photocatalytic activity in Cu nanoparticles covered Cu₂O microspheres for degrading organic pollutants. *Appl. Surf. Sci.* **2016**, *366*, 120–128.

The First Materials Research Society of Thailand International Conference
(1st MRS Thailand International Conference)
October 31 – November 3, 2017
The Empress Convention Center, Chiang Mai, Thailand

Mediator Electrode for Water Splitting in Separate Hydrogen and Oxygen Cells

S. Musikajaroen^{a,*}, S. Pol-in^a, W. Meevasana^a

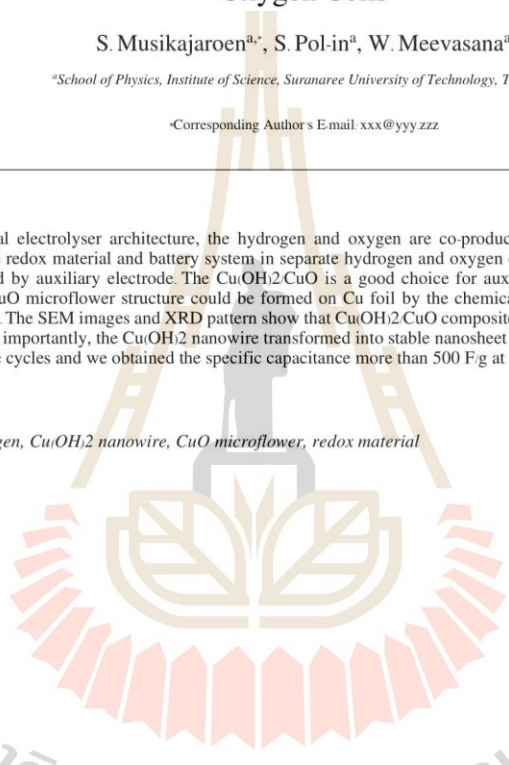
^a*School of Physics, Institute of Science, Suranaree University of Technology, Thailand*

*Corresponding Author's E-mail: xxx@yyy.zzz

Abstract

The conventional electrolyser architecture, the hydrogen and oxygen are co-produced in the same cell. For this problem, we use redox material and battery system in separate hydrogen and oxygen cells. The ion exchange in our cells is mediated by auxiliary electrode. The $\text{Cu(OH)}_2\text{CuO}$ is a good choice for auxiliary electrode. The Cu(OH)_2 nanowire and CuO microflower structure could be formed on Cu foil by the chemical oxidation reaction of Cu in alkaline solution. The SEM images and XRD pattern show that $\text{Cu(OH)}_2\text{CuO}$ composite were successfully synthesize on Cu foil. More importantly, the Cu(OH)_2 nanowire transformed into stable nanosheet CuO.Cu(OH)_2 after about 100 charge-discharge cycles and we obtained the specific capacitance more than 500 F/g at current density 5 A/g.

Keyword: hydrogen, Cu(OH)_2 nanowire, CuO microflower, redox material



มหาวิทยาลัยเทคโนโลยีสุรนารี

The Second Materials Research Society of Thailand International Conference
(2nd MRS Thailand International Conference)
10-12 July 2019
The Zign Hotel, Pattaya, Thailand

Electronic Structure of CuO-Cu(OH)₂/Cu₂O Mediator electrodes During Water Electrolysis under Sunlight Irradiation

S. Musikajaroen^a, S. Polin^a, C. Jaisuk^a, W. Jindata^a, N. Chanlek^b, S. Satayaporn^b, P.
Kidkhunthod^b, H. Nakajima^b and W. Meevasana^{a,*}

^aSchool of Physics, Institute of Science, Suranaree University of Technology, Nakhon Ratchasima, 30000, Thailand

^bSynchrotron Light Research Institute, Nakhon Ratchasima, 30000, Thailand

*Corresponding Author's E-mail: worawat@g.sut.ac.th

Abstract

Water electrolysis has received much attention for sustainable hydrogen production. Many challenges still remain in enhancing high-purity H₂ and reducing the hydrogen production cost for large-scale. This study provides a research strategy for integrated two-cell water electrolysis system with solar energy storage utilization, which is leading to increase pure hydrogen production. In our cells, the OH⁻ ion exchange between hydrogen and oxygen cells by charging/discharging of Cu₂O/CuO-Cu(OH)₂ redox mediator electrodes under sunlight illumination. Intrinsic sunlight affecting the redox reaction of Cu₂O/CuO-Cu(OH)₂ during water electrolysis are first analyzed, whereby understanding and characterizing the changing oxidation state of mediator electrodes. The photoemission and in situ X-ray absorption spectroscopy-based methodology are discussed to determine electronic and structural properties of Cu₂O/CuO-Cu(OH)₂ which allows the prediction of water electrolysis mechanism.

Keywords: CuO, Cu(OH)₂, Cu₂O, water electrolysis, photo-charging, in situ XAS, photoemission spectroscopy

มหาวิทยาลัยเทคโนโลยีสุรนารี

The 21st International Union of Materials Research Societies – International Conference in Asia
(IUMRS-ICA2020), 23-26 February 2021
The Empress Convention Center, Chiang Mai, Thailand

Recent Improvement of Photo-enhanced Water Electrolysis in Separate O₂ and H₂ Cells using Pseudocapacitive Electrodes

S. Musikajaroen^{a,b}, S. Polin^a, S. Sattayaporn^c, W. Jindata^a, W. Saenrang^{a,b},
P. Kidkhunthod^c, H. Nakajima^c, T. Butburee^d, N. Chanlek^c and W. Meevasana^{a,b,*}

^a Research Network NANOTEC-SUT on Advanced Nanomaterials and Characterization and School of Physics, Suranaree University of Technology, Nakhon Ratchasima 30000, Thailand

^b Thailand Center of Excellence in Physics, Ministry of Higher Education, Science, Research and Innovation, 328 Si Ayutthaya Road, Bangkok 10400, Thailand

^c Synchrotron Light Research Institute, Nakhon Ratchasima, 30000, Thailand

^d National Nanotechnology Center, National Science and Technology Development Agency, 111 Thailand Science Park, Pathum Thani, 12120, Thailand

*Corresponding Author's E-mail: worawat@g.sut.ac.th

Abstract

Water electrolysis has received much attention in recent years as a means of sustainable H₂ production. However, many challenges remain in obtaining high-purity H₂ and making large-scale production cost-effective. This study provides a strategy for integrating a two-cell water electrolysis system with solar energy storage. Our proposed system has been developed with electrodes acting as both a redox mediator and as a photo-supercapacitor for improved H₂ and O₂ gas production. The solar-driven pseudocapacitive behavior on CuO-Cu(OH)₂/Cu₂O mediator electrode pair exhibits an increase in the specific capacitance compared with that in the absence of light (36%). In our recent progress, after improving the electrodes and adjusting the electrolysis parameters, we show an increase of the initial H₂ and O₂ production rates by 45% with better duration of more than 1.5 hrs. The effects of light on the CuO-Cu(OH)₂/Cu₂O were investigated by photoemission spectroscopy. These findings provide a new path to direct storage of abundant solar energy and low-cost sustainable hydrogen production.

Keywords: CuO-Cu(OH)₂/Cu₂O; Two-cells water electrolysis; Hydrogen production; Photocapacitance; Oxygen vacancy

มหาวิทยาลัยเทคโนโลยีสุรนารี

CURRICULUM VITAE

Name Miss Supansa Musikajaroen

Date of Birth July 29, 1983

Place of Birth 43 Moo 1, Khaochaison sub-district, Khaochaison district, Phatthalung, 93130, Thailand.

Education

2014-2021 Suranaree University of Technology, Nakhon Ratchasima, Thailand.
Ph.D. in Physics

2006-2008 Chiang Mai University
M.Sc. in Applied Physics

2002-2005 Prince of Songkla University, Songkla, Thailand.
B.Sc. in Physics

Position and Place of Work

Company Employee
EQ TECH ENERGY CO., LTD.
281/1 Ladya Road, Somdet-chaopraya, Klongsan,
Bangkok 10600 Thailand